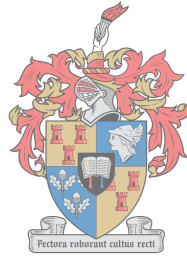


# Physical Optics Based Methods for Scattering Analysis

by

Michael Peter Richardson



UNIVERSITEIT  
iYUNIVESITHI  
STELLENBOSCH  
UNIVERSITY

*Thesis presented in partial fulfilment of the requirements for  
the degree of Master of Engineering (Electronic) in the  
Faculty of Engineering at Stellenbosch University*

Supervisor: Prof. MM. Botha

March 2018

# Declaration

By submitting this thesis electronically, I declare that the entirety of the work contained therein is my own, original work, that I am the sole author thereof (save to the extent explicitly otherwise stated), that reproduction and publication thereof by Stellenbosch University will not infringe any third party rights and that I have not previously in its entirety or in part submitted it for obtaining any qualification.

Date: ..... March 2018 .....

Copyright ©2018 Stellenbosch University  
All rights reserved.

# Abstract

## Physical Optics Based Methods for Scattering Analysis

MP. Richardson

*Department of Electrical and Electronic Engineering,  
University of Stellenbosch,  
Private Bag X1, Matieland 7602, South Africa.*

Thesis: MEng (Electronic)

November 2017

The physical optics (PO) approximation is often used in asymptotic, electromagnetic scattering analysis to calculate the induced current on a perfectly conducting surface, represented by a mesh. The multiple reflection physical optics (MRPO) method is the recursive application of the PO approximation. MRPO uses full, inter-segment visibility shadowing. Iterative physical optics is similar, except the shadowing is relaxed. Only half-space visibility is used for shadowing. The performance of these methods is investigated for a variety of test cases.

The domain decomposition physical optics (DDPO) method is presented. It decomposes the geometry into two parts, a cavity and external geometry. The two geometries interact through an aperture, using equivalent sources. Thus, the shadowing can be calculated for the individual geometries and not as a whole. The equivalent sources and aperture interactions are validated. The performance of DDPO is investigated for various, simple test cases.

All methods and results are presented in a two-dimensional, transverse magnetic context.

# Opsomming

## Fisiese Optika-gebaseerde Metodes vir Verstrooiingsanalise

*(“Physical Optics Based Methods for Scattering Analysis”)*

MP. Richardson

*Departement Elektriese en Elektroniese Ingenieurswese,  
Universiteit van Stellenbosch,  
Privaatsak X1, Matieland 7602, Suid Afrika.*

Tesis: MIng (Elektronies)

November 2017

Die fisiese optika (PO) benadering word dikwels gebruik in asimptotiese, elektromagnetiese verstrooiingsanalise om die geïnduseerde stroom op 'n perfek geleidende oppervlak te bereken, wat deur 'n maas voorgestel word. Die veelvoudige weerkaatsing fisiese optika metode (MRPO) is die rekursiewe toepassing van die PO-benadering. MRPO gebruik volledige, inter-segment sigbaarheidsbepaling. Iteratiewe fisiese optika is soortgelyk, behalwe die sigbaarheidsbepaling is minder streng. Slegs halfspasie-sigbaarheid word gebruik. Die uitvoering van hierdie metodes word ondersoek vir 'n verskeidenheid toetsgevallen.

Die domein dekomposisie fisiese optika (DDPO) metode word aangebied. Dit breek die struktuur op in twee dele, 'n holte en eksterne gebied. Die twee dele koppel deur middel van ekwivalente bronne op 'n gepaste stralingsvlak. Die skaduweebepaling hoef slegs vir die afsonderlike dele gedoen te word. Verifikasie van die ekwivalente bronne en stralingsvlak interaksies word gedoen. Die prestasie van DDPO word ondersoek vir verskeie, eenvoudige toetsgevallen.

Alle metodes en resultate word in 'n tweedimensionele, transversale magnetiese konteks aangebied.

# Contents

<b>Declaration</b>	<b>i</b>
<b>Abstract</b>	<b>ii</b>
<b>Opsomming</b>	<b>iii</b>
<b>Contents</b>	<b>iv</b>
<b>List of Figures</b>	<b>vi</b>
<b>Nomenclature</b>	<b>xi</b>
<b>1 Introduction</b>	<b>1</b>
1.1 Introduction . . . . .	1
1.2 CEM for Scattering Analysis . . . . .	1
1.3 Asymptotic Methods . . . . .	1
1.4 Report Overview . . . . .	2
<b>2 Method of Moments</b>	<b>3</b>
2.1 Introduction . . . . .	3
2.2 Integral Equation Theory . . . . .	3
2.3 Formulation . . . . .	7
2.4 Verification . . . . .	10
2.5 Conclusion . . . . .	12
<b>3 MRPO and IPO</b>	<b>13</b>
3.1 Introduction . . . . .	13
3.2 Physical Optics . . . . .	13
3.3 Multiple Reflection Physical Optics . . . . .	14
3.4 Iterative Physical Optics . . . . .	15
3.4.1 Fixed Point Iterations . . . . .	16
3.4.1.1 Jacobi Iteration . . . . .	17
3.4.1.2 Gauss-Seidel Iteration . . . . .	18
3.4.1.3 SOR Iteration . . . . .	18
3.4.1.4 SSOR Iteration . . . . .	18

## CONTENTS

v

3.4.2	Combined System Methods . . . . .	19
3.4.2.1	Direct Solution . . . . .	20
3.4.2.2	GMRES Iteration . . . . .	20
3.4.2.3	JMRES Iteration . . . . .	21
3.4.2.4	Other methods . . . . .	22
3.4.3	Relaxed Method . . . . .	22
3.5	MRPO and IPO Evaluation . . . . .	23
3.5.1	MRPO Performance Assessment . . . . .	23
3.5.2	IPO Performance Assessment . . . . .	30
3.5.3	MRPO and IPO Comparison . . . . .	38
3.5.4	General, Closed Body Results . . . . .	44
3.5.5	Relaxed Jacobi $\alpha$ Parameter Assessment . . . . .	47
3.6	Conclusion . . . . .	52
<b>4</b>	<b>Domain Decomposition PO</b>	<b>53</b>
4.1	Introduction . . . . .	53
4.2	Formulation . . . . .	53
4.3	Computational Cost . . . . .	61
4.4	Validation . . . . .	61
4.4.1	Aperture Source Accuracy . . . . .	61
4.4.2	Aperture Source Interaction . . . . .	64
4.5	Evaluation . . . . .	67
4.5.1	Square Cavity . . . . .	68
4.5.2	Square Cavity with External Geometry . . . . .	69
4.6	Conclusion . . . . .	72
<b>5</b>	<b>Conclusion</b>	<b>73</b>
	<b>List of References</b>	<b>75</b>

# List of Figures

2.1	Two-dimensional structure in free space. . . . .	4
2.2	Two-dimensional segmented structure in free space. . . . .	7
2.3	A segment, $S_n$ , from a structure in free space. . . . .	9
2.4	Validation structures. . . . .	11
	(a) Circular cylinder in free space. . . . .	11
	(b) Square cylinder in free space. . . . .	11
2.5	Circular cylinder bi-static SW. . . . .	11
2.6	Square cylinder bi-static SW. . . . .	11
3.1	PEC structure in free space. . . . .	13
3.2	Corner reflector. . . . .	23
3.3	MRPO – Corner reflector bi-static SW. . . . .	24
	(a) Solution history. . . . .	24
	(b) Final solution (K=5). . . . .	24
3.4	Test structures in free space. . . . .	25
	(a) Line with angled edge. . . . .	25
	(b) Circle with a 40° opening. . . . .	25
	(c) Circle with a 180° opening . . . . .	25
	(d) Irregular Octagon. . . . .	25
3.5	MRPO – Line with angled edge bi-static SW. . . . .	26
	(a) Small structure. . . . .	26
	(b) Medium structure. . . . .	26
	(c) Large structure. . . . .	26
3.6	MRPO – Circle with a 40° opening bi-static SW. . . . .	27
	(a) Small structure. . . . .	27
	(b) Medium structure. . . . .	27
	(c) Large structure. . . . .	27
3.7	MRPO – Circle with a 180° opening bi-static SW. . . . .	28
	(a) Small structure. . . . .	28
	(b) Medium structure. . . . .	28
	(c) Large structure. . . . .	28
3.8	MRPO – Irregular octagon bi-static SW. . . . .	29
	(a) Small structure. . . . .	29
	(b) Medium structure. . . . .	29

(c)	Large structure. . . . .	29
3.9	IPO – Line with angled edge bi-static SW for additional methods. . . . .	30
(a)	Fixed point iterations. . . . .	30
(b)	Combined system methods. . . . .	30
3.10	IPO – Line with angled edge bi-static SW. . . . .	31
(a)	Small structure. . . . .	31
(b)	Medium structure. . . . .	31
(c)	Large structure. . . . .	31
3.11	IPO – Line with angled edge convergence error history. . . . .	32
(a)	Small structure. . . . .	32
(b)	Medium structure. . . . .	32
(c)	Large structure. . . . .	32
3.12	IPO – Circle with a 40° opening bi-static SW. . . . .	33
(a)	Small structure. . . . .	33
(b)	Medium structure. . . . .	33
(c)	Large structure. . . . .	33
3.13	IPO – Circle with a 40° opening convergence error history. . . . .	34
(a)	Small structure. . . . .	34
(b)	Medium structure. . . . .	34
(c)	Large structure. . . . .	34
3.14	IPO – Circle with a 180° opening bi-static SW. . . . .	35
(a)	Small structure. . . . .	35
(b)	Medium structure. . . . .	35
(c)	Large structure. . . . .	35
3.15	IPO – Circle with a 180° opening convergence error history. . . . .	36
(a)	Small structure. . . . .	36
(b)	Medium structure. . . . .	36
(c)	Large structure. . . . .	36
3.16	IPO – Irregular octagon bi-static SW. . . . .	37
(a)	Small structure. . . . .	37
(b)	Medium structure. . . . .	37
(c)	Large structure. . . . .	37
3.17	IPO – Irregular octagon convergence error history. . . . .	38
(a)	Small structure. . . . .	38
(b)	Medium structure. . . . .	38
(c)	Large structure. . . . .	38
3.18	MRPO & IPO – Medium sized line with angled edge. . . . .	39
(a)	Bi-static SW (0° - 180°). . . . .	39
(b)	Bi-static SW (180° - 360°). . . . .	39
(c)	Bi-static SW error. . . . .	39
(d)	Convergence error history. . . . .	39
3.19	MRPO & IPO – Medium sized circle with a 40° opening. . . . .	40
(a)	Bi-static SW (0° - 180°). . . . .	40
(b)	Bi-static SW (180° - 360°). . . . .	40



(c)	Bi-static SW Error. . . . .	40
(d)	Convergence error history. . . . .	40
3.20	MRPO & IPO – Medium sized circle with a 180° opening. . . . .	41
(a)	Bi-static SW (0° - 180°). . . . .	41
(b)	Bi-static SW (180° - 360°). . . . .	41
(c)	Bi-static SW Error. . . . .	41
(d)	Convergence error history. . . . .	41
3.21	MRPO & IPO – Medium sized irregular octagon. . . . .	42
(a)	Bi-static SW (0° - 180°). . . . .	42
(b)	Bi-static SW (180° - 360°). . . . .	42
(c)	Bi-static SW Error. . . . .	42
(d)	Convergence error history. . . . .	42
3.22	(a) Shows both sides of the structure having normals, thus modelling the external and internal current. (b) Shows only the external normals, thus only modelling the external currents. . . . .	44
(a)	Irregular octagon cavity. . . . .	44
(b)	Irregular octagon solid. . . . .	44
3.23	Irregular octagon cavity bi-static SW (Includes internal currents). . . . .	45
(a)	Bi-static SW (0° - 180°). . . . .	45
(b)	Bi-static SW (180° - 360°). . . . .	45
(c)	Bi-static SW error. . . . .	45
(d)	Convergence error history. . . . .	45
3.24	Irregular octagon solid bi-static SW (Excludes internal currents). . . . .	46
(a)	Bi-static SW (0° - 180°). . . . .	46
(b)	Bi-static SW (180° - 360°). . . . .	46
(c)	Bi-static SW error. . . . .	46
(d)	Convergence error history. . . . .	46
3.25	Line with angled edge. . . . .	48
(a)	Bi-static SW (0° - 180°). . . . .	48
(b)	Bi-static SW (180° - 360°). . . . .	48
(c)	Bi-static SW error. . . . .	48
(d)	Convergence error history. . . . .	48
3.26	Circle with a 40° opening. . . . .	49
(a)	Bi-static SW (0° - 180°). . . . .	49
(b)	Bi-static SW (180° - 360°). . . . .	49
(c)	Bi-static SW error. . . . .	49
(d)	Convergence error history. . . . .	49
3.27	Circle with a 180° opening . . . . .	50
(a)	Bi-static SW (0° - 180°). . . . .	50
(b)	Bi-static SW (180° - 360°). . . . .	50
(c)	Bi-static SW error. . . . .	50
(d)	Convergence error history. . . . .	50
3.28	Irregular octagon. . . . .	51
(a)	Bi-static SW (0° - 180°). . . . .	51

(b)	Bi-static SW ( $180^\circ$ - $360^\circ$ ) . . . . .	51
(c)	Bi-static SW error. . . . .	51
(d)	Convergence error history. . . . .	51
4.1	Boeing 747-400 CAD model [23]. . . . .	54
4.2	Jet engine inlet CAD model [24]. . . . .	54
4.3	DDPO current calculation flow chart. . . . .	56
4.4	DDPO Initial currents. . . . .	57
4.5	DDPO Incident currents. . . . .	58
4.6	DDPO First reflection currents. . . . .	59
4.7	DDPO Second reflection currents. . . . .	60
4.8	Horizontal line with aperture for equivalent source tests. . . . .	62
(a)	$5\lambda$ . . . . .	62
(b)	$10\lambda$ . . . . .	62
(c)	$20\lambda$ . . . . .	62
(d)	$50\lambda$ . . . . .	62
(e)	$100\lambda$ . . . . .	62
(f)	$500\lambda$ . . . . .	62
4.9	Equivalent source tests. The black line represents the current induced, on the line segment surface with half the geometry in shadow, due to the incident source. The blue line represents the current induced from the aperture. . . . .	63
(a)	$5\lambda$ . . . . .	63
(b)	$10\lambda$ . . . . .	63
(c)	$20\lambda$ . . . . .	63
(d)	$50\lambda$ . . . . .	63
(e)	$100\lambda$ . . . . .	63
(f)	$500\lambda$ . . . . .	63
4.10	$10\lambda$ Reflector with varying aperture sizes. . . . .	64
(a)	$10\lambda$ . . . . .	64
(b)	$20\lambda$ . . . . .	64
(c)	$40\lambda$ . . . . .	64
(d)	$80\lambda$ . . . . .	64
4.11	$10\lambda$ Reflector aperture test. . . . .	65
(a)	Bi-static SW. . . . .	65
(b)	Bi-static SW. . . . .	65
4.12	$20\lambda$ Reflector with varying aperture sizes. . . . .	66
(a)	$10\lambda$ . . . . .	66
(b)	$20\lambda$ . . . . .	66
(c)	$40\lambda$ . . . . .	66
(d)	$80\lambda$ . . . . .	66
4.13	$20\lambda$ Reflector aperture test. . . . .	67
(a)	Bi-static SW. . . . .	67
(b)	Bi-static SW. . . . .	67

## LIST OF FIGURES

x

4.14	Open square cavity with aperture. . . . .	68
4.15	Open square cavity with aperture bi-static SW. . . . .	69
	(a) Single reflection ( $K=1$ ) bi-static SW. . . . .	69
	(b) Multiple reflections ( $K=5$ ) bi-static SW. . . . .	69
4.16	Square cavity with external geometry. . . . .	70
	(a) $5\lambda$ Aperture. . . . .	70
	(b) $10\lambda$ Aperture. . . . .	70
	(c) $20\lambda$ Aperture. . . . .	70
	(d) $50\lambda$ Aperture. . . . .	70
4.17	Square cavity with external geometry bi-static SW. . . . .	71
	(a) $5\lambda$ Aperture. . . . .	71
	(b) $10\lambda$ Aperture. . . . .	71
	(c) $20\lambda$ Aperture. . . . .	71
	(d) $50\lambda$ Aperture. . . . .	71

# Nomenclature

## Constants

$\mu_0$	$4\pi \times 10^{-7}$	$H \cdot m^{-1}$
$\epsilon_0$	$8.854e^{-12}$	$F \cdot m^{-1}$
$c$	$1/\sqrt{\epsilon_0\mu_0}$	$m \cdot s^{-1}$
$Z_0$		$\mu_0 c \quad \Omega$

## Abbreviations

CEM	Computational Electromagnetics
TM	Transverse Magnetic
PEC	Perfect Electric Conductor
EFIE	Electric Field Integral Equation
MFIE	Magnetic Field Integral Equation
MoM	Method of Moments
RCS	Radar Cross Section
PO	Physical Optics
SRPO	Single Reflection Physical Optics
MRPO	Multiple Reflection Physical Optics
IPO	Iterative Physical Optics
DDPO	Domain Decomposition Physical Optics

## Definitions

$f$	Frequency in Hertz (Hz)
$k_0$	$2\pi/f$
$\lambda_0$	$c/f$
$\phi$	Observation angle
$\mathcal{I}$	Identity matrix
$\delta$	MRPO Shadowing coefficient
$\gamma$	IPO Shadowing coefficient

# Chapter 1

## Introduction

### 1.1 Introduction

A background is given on computational electromagnetic (CEM) methods for electromagnetic scattering analysis. An overview of asymptotic methods is also provided, with emphasis on physical optics (PO). Multiple reflection physical optics (MRPO) and iterative physical optics (IPO) are investigated throughout the thesis.

The main contributions of the thesis are: (i) a detailed, numerical performance assessment of MRPO and IPO; and (ii) the presentation of a domain decomposition method for the MRPO, to reduce its computational cost for certain applications.

### 1.2 CEM for Scattering Analysis

Electromagnetic scattering analysis is an important topic which has been focused on extensively in recent literature. Scattering analysis is important for various applications such as radar cross section (RCS) calculations and antenna reflections. For electrically small structures, the method of moments (MoM) can be used [1, 2]. For electrically large structures the method of moments is too expensive to use. Even using accelerated MoM formulations, such as multi-level fast multi-pole method (MLFMM) [3], for structures upwards in size of 100 wavelengths become impractical to run, depending on available resources. A more suitable approach is to use asymptotic methods such as the physical optics method [4].

### 1.3 Asymptotic Methods

Asymptotic methods are widely used for scattering analysis. They can be placed into one of two groups – ray-based methods and current based meth-

ods. The ray-based methods include two sub categories, ray-tracing and ray-launching methods. Ray-tracing includes methods such as geometric optics (GO) and uniform theory of diffraction (UTD) [4, 5]. Ray-launching includes methods such as shooting-and-bouncing rays (SBR) [6]. The second group, current methods, includes physical optics [4].

Ray-tracing methods model the reflections and diffraction that occurs on the propagation path from the source point to the observation point, and apply canonical solutions.

The ray-launching methods use an accurate representation of the geometry to track the specular reflections of launched ray tubes. At the points where the rays interact with the geometry or leave an enclosed surface, equivalent sources are placed.

The PO approximation continues to find applications in scattering analysis [7]. Physical optics relates the incident magnetic field to the induced surface current at points that are in direct line of sight of each other [8, 9]. MRPO is the PO approximation, with rigorous shadowing applied to the field due to the currents on the surface, which calculates multiple internal reflections [10], this is where the runtime bottleneck occurs. In [10] the formulation is actually that of the MRPO and not IPO. In MRPO, the shadowing between each pair of source and observation points is calculated. IPO is very similar to the MRPO method. The shadowing for IPO is simplified as geometry between each pair of source and observation points is ignored [11, 12], which means the IPO iteration cannot be interpreted as a physical reflection. The IPO solves the magnetic field integral equation (MFIE) iteratively with the shadowing coefficient included. The IPO is a Picard-type iterative solution to the MFIE [13]. The benefits of IPO above MRPO is that dramatically less computational effort is needed to determine the shadowing coefficients. The convergence of neither MRPO nor IPO, has been shown to be theoretically guaranteed.

## 1.4 Report Overview

Chapter 2 will give an in-depth formulation of the electric field integral equation (EFIE) and MFIE. The method of moments will be formulated and verified. All of this will be done in the two-dimensional (2D), transverse magnetic (TM) field context, which is the case considered throughout.

Chapter 3 will discuss the MRPO and IPO methods. Several IPO variants are investigated. The numerical performance of the MRPO and IPO methods is investigated in detail.

In Chapter 4, the domain decomposition physical optics (DDPO) will be introduced. The DDPO formulation is presented in detail. The method will then be evaluated against MRPO from chapter 3.

The last chapter presents a final discussion on the work done in the thesis and gives a detailed conclusion to the report.

# Chapter 2

## Method of Moments

### 2.1 Introduction

This chapter will present an in-depth review of the electric field integral equation (EFIE) and the magnetic field integral equation (MFIE). The 2D, TM EFIE formulation is derived in [2] and is documented here as a basis for the work to be presented later on. The derivations are all within the 2D, TM context. This means that the structure and source have no variation in the  $z$ -axis as it is a 2D problem, with  $\mathbf{E}(\boldsymbol{\rho}) = E_z(\boldsymbol{\rho})\hat{z}$ . Thus only the plane perpendicular to the  $z$ -axis,  $xy$  plane, is considered. The EFIE will be the foundation for the method of moments (MoM) described in section 2.3 for PEC structures. The MFIE will be used in chapter 4 but follows on from the EFIE so it is derived in this chapter. The chapter ends off with the MoM implementation being validated using FEKO.

### 2.2 Integral Equation Theory

This section will formulate the electric field integral equation and magnetic field integral equation. Two-dimensional electromagnetic problems can use a scalar Helmholtz equation as the governing equation, in case where only one field component is present.

Consider the problem of an arbitrarily shaped structure in free space, as shown in Figure 2.1. The region enclosed by the boundary,  $\Gamma_0$ , will be referred to as the interior region,  $\Omega_0$ . Everywhere else will be known as the exterior region,  $\Omega_\infty$ . This structure is in the presence of a source producing an incident wave. The electric field satisfies the Helmholtz equation:

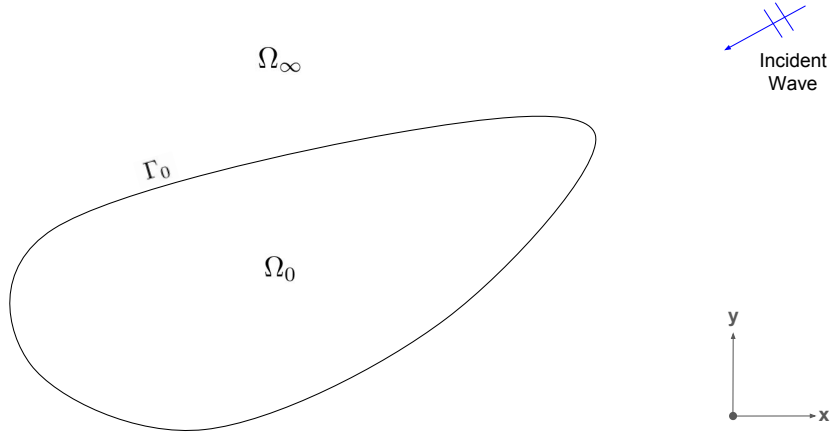


Figure 2.1: Two-dimensional structure in free space.

$$\nabla^2 E_z(\boldsymbol{\rho}) + k_0^2 E_z(\boldsymbol{\rho}) = E_z^{\text{inc}}(\boldsymbol{\rho}) \quad (2.1)$$

In order to get the integral equation, the free-space Green's function  $G_0(\boldsymbol{\rho}, \boldsymbol{\rho}')$  is introduced in (2.2) which satisfies the inhomogeneous Helmholtz equation, where  $\delta(\boldsymbol{\rho} - \boldsymbol{\rho}')$  is the Dirac delta function.

$$G_0(\boldsymbol{\rho}, \boldsymbol{\rho}') = \frac{1}{4j} H_0^{(2)}(k_0 |\boldsymbol{\rho} - \boldsymbol{\rho}'|) \quad (2.2)$$

$$\nabla^2 G_0(\boldsymbol{\rho}, \boldsymbol{\rho}') + k_0^2 G_0(\boldsymbol{\rho}, \boldsymbol{\rho}') = -\delta(\boldsymbol{\rho} - \boldsymbol{\rho}') \quad (2.3)$$

Where  $\boldsymbol{\rho}$  and  $\boldsymbol{\rho}'$  are the source and observation points,  $H_0^{(2)}$  is the zero-th order Hankel function of the second kind. After some careful manipulation of equations (2.1) and (2.3), shown in [2], the general EFIE is established.

$$E_z^{\text{inc}}(\boldsymbol{\rho}) + \oint_{\Gamma_0} \left[ E_z(\boldsymbol{\rho}') \frac{\partial G_0(\boldsymbol{\rho}, \boldsymbol{\rho}')}{\partial n'} - G_0(\boldsymbol{\rho}, \boldsymbol{\rho}') \frac{\partial E_z(\boldsymbol{\rho}')}{\partial n'} \right] d\Gamma' = \begin{cases} E_z(\boldsymbol{\rho}), & \boldsymbol{\rho} \in \Omega_\infty \\ 0, & \boldsymbol{\rho} \in \Omega_0 \end{cases} \quad (2.4)$$

For observation points in the  $xy$ -plane, Faraday's Law can be expressed as follows:

$$\mathbf{H}(\boldsymbol{\rho}) = -\frac{1}{j\omega\mu_0} \nabla \times \mathbf{E}(\boldsymbol{\rho}) \quad (2.5)$$

Substituting (2.4) into (2.5), yields

$$\mathbf{H}^{\text{inc}}(\boldsymbol{\rho}) - \frac{1}{j\omega\mu_0} \oint_{\Gamma_0} \left[ \nabla \times \mathbf{T}_1(\boldsymbol{\rho}') - \nabla \times \mathbf{T}_2(\boldsymbol{\rho}') \right] d\Gamma' = \begin{cases} \mathbf{H}(\boldsymbol{\rho}), & \boldsymbol{\rho} \in \Omega_\infty \\ 0, & \boldsymbol{\rho} \in \Omega_0 \end{cases} \quad (2.6)$$



where,

$$\mathbf{H}^{\text{inc}}(\boldsymbol{\rho}) = -\frac{1}{j\omega\mu_0}\nabla \times E_z^{\text{inc}}(\boldsymbol{\rho})\hat{z} \quad (2.7)$$

$$\nabla \times \mathbf{T}_1(\boldsymbol{\rho}') = \nabla \times E_z(\boldsymbol{\rho}')\frac{\partial G_0(\boldsymbol{\rho}, \boldsymbol{\rho}')}{\partial n'}\hat{z} \quad (2.8)$$

$$\nabla \times \mathbf{T}_2(\boldsymbol{\rho}') = \nabla \times G_0(\boldsymbol{\rho}, \boldsymbol{\rho}')\frac{\partial E_z(\boldsymbol{\rho}')}{\partial n'}\hat{z} \quad (2.9)$$

It can be seen that (2.7) is trivial and results in  $\mathbf{H}^{\text{inc}}(\boldsymbol{\rho})$ . The objective is to rework (2.8) and (2.9) into expressions which can be directly implemented to evaluate the magnetic field given a source distribution. Consider (2.9) next. It is slightly more complicated and gives the result below

$$\begin{aligned} \nabla \times \mathbf{T}_2(\boldsymbol{\rho}') &= \nabla G_0(\boldsymbol{\rho}, \boldsymbol{\rho}') \times \frac{\partial E_z(\boldsymbol{\rho}')}{\partial n'}\hat{z} \\ &= \frac{j H_1^{(2)}(k_0|\boldsymbol{\rho} - \boldsymbol{\rho}'|)}{4} \frac{\partial E_z(\boldsymbol{\rho}')}{\partial n'} [(\boldsymbol{\rho} - \boldsymbol{\rho}') \times \hat{z}] \end{aligned} \quad (2.10)$$

The second term, (2.8), is more complicated to derive. In the interest of simplifying the notation,  $G_0(\boldsymbol{\rho}, \boldsymbol{\rho}')$  will be referred to as  $G_0$ . The derivative of  $G_0$  with respect to the unit normal in (2.8) can be expanded to give (2.11). Substituting (2.11) into (2.8) results in (2.12).

$$E_z(\boldsymbol{\rho}')\frac{\partial G_0}{\partial n'} = E_z(\boldsymbol{\rho}')(\nabla' G_0 \cdot \hat{n}')\hat{z} \quad (2.11)$$

$$\begin{aligned} \nabla \times \mathbf{T}_1(\boldsymbol{\rho}') &= E_z(\boldsymbol{\rho}') \left[ \nabla \times \frac{\partial G_0}{\partial n'}\hat{z} \right] \\ &= E_z(\boldsymbol{\rho}') [\nabla \times (\nabla' G_0 \cdot \hat{n}')\hat{z}] \end{aligned} \quad (2.12)$$

Using the vector identity below, (2.12) can be written as (2.14) [14].

$$\nabla \times (\psi \mathbf{A}) = \nabla \psi \times \mathbf{A} + \psi \nabla \times \mathbf{A} \quad (2.13)$$

$$\begin{aligned} \nabla \times \mathbf{T}_1(\boldsymbol{\rho}') &= E_z(\boldsymbol{\rho}') [\nabla \times (\nabla' G_0 \cdot \hat{n}')\hat{z}] \\ &= E_z(\boldsymbol{\rho}') [\nabla (\nabla' G_0 \cdot \hat{n}') \times \hat{z} + (\nabla' G_0 \cdot \hat{n}') \nabla \times \hat{z}] \end{aligned} \quad (2.14)$$

In (2.14), the last term falls away as  $\nabla \times \hat{z} = 0$ . Applying the vector identity below to (2.14) will result in (2.16) [14].

$$\begin{aligned} \nabla(\mathbf{A} \cdot \mathbf{B}) &= (\mathbf{A} \cdot \nabla)\mathbf{B} + (\mathbf{B} \cdot \nabla)\mathbf{A} + \mathbf{A} \\ &\quad \times (\nabla \times \mathbf{B}) + \mathbf{B} \times (\nabla \times \mathbf{A}) \end{aligned} \quad (2.15)$$

$$\begin{aligned}
\nabla \times \mathbf{T}_1(\boldsymbol{\rho}') &= E_z(\boldsymbol{\rho}') [\nabla(\nabla' G_0 \cdot \hat{n}')] \times \hat{z} \\
&= E_z(\boldsymbol{\rho}') \left[ (\hat{n}' \cdot \nabla) \nabla' G_0 + (\nabla' G_0 \cdot \nabla) \hat{n}' + \hat{n}' \right. \\
&\quad \left. \times (\nabla \times \nabla' G_0) + \nabla' G_0 \times (\nabla \times \hat{n}') \right] \times \hat{z}
\end{aligned} \tag{2.16}$$

The last three terms of (2.16) are equal zero. The term  $(\nabla' G_0 \cdot \nabla) \hat{n}'$  equals zero as the non-accented derivative of an accented co-ordinate function is zero. The  $\hat{n}' \times (\nabla \times \nabla' G_0)$  term equals zero as the curl of a gradient is zero. The last term,  $\nabla' G_0 \times (\nabla \times \hat{n}')$ , is zero because  $(\nabla \times \hat{n}') = 0$ . Thus the equation can be simplified as shown below.

$$\begin{aligned}
\nabla \times \mathbf{T}_1(\boldsymbol{\rho}') &= E_z(\boldsymbol{\rho}') [(\hat{n}' \cdot \nabla) \nabla' G_0] \times \hat{z} \\
&= E_z(\boldsymbol{\rho}') [-(\hat{n}' \cdot \nabla') \nabla' G_0] \times \hat{z} \\
&= -E_z(\boldsymbol{\rho}') [\hat{n}' \cdot \nabla' \nabla' G_0] \times \hat{z}
\end{aligned} \tag{2.17}$$

Once (2.8) and (2.9) have been substituted back into (2.6), the general MFIE can be represented as follows:

$$\begin{aligned}
\mathbf{H}^{\text{inc}}(\boldsymbol{\rho}) + \frac{1}{j\omega\mu_0} \oint_{\Gamma_0} \left[ E_z(\boldsymbol{\rho}') [\hat{n}' \cdot \nabla' \nabla' G_0 \times \hat{z}] \right. \\
\left. + \nabla G_0 \times [\hat{n}' \times \mathbf{H}(\boldsymbol{\rho}')] \right] d\Gamma' = \mathbf{H}(\boldsymbol{\rho})
\end{aligned} \tag{2.18}$$

The rest of the derivation will consist of deriving the values for (2.17). It is now rewritten in a format which is more suitable for practical implementation. The double gradient of the Green's function will first be derived.

$$\begin{aligned}
\nabla \times \mathbf{T}_1(\boldsymbol{\rho}') &= E(\boldsymbol{\rho}') [\hat{z} \times (\hat{n}' \cdot \nabla') \nabla' G_0] \\
&= E(\boldsymbol{\rho}') \left[ \hat{z} \times \left( \hat{n}'_x \frac{\partial}{\partial x'} + \hat{n}'_y \frac{\partial}{\partial y'} \right) \left( \frac{\partial G_0}{\partial x'} \hat{x} + \frac{\partial G_0}{\partial y'} \hat{y} \right) \right] \\
&= E(\boldsymbol{\rho}') \left[ \hat{z} \times \left( \left( \hat{n}'_x \frac{\partial^2 G_0}{\partial^2 x'} + \hat{n}'_y \frac{\partial^2 G_0}{\partial x' \partial y'} \right) \hat{x} + \left( \hat{n}'_x \frac{\partial^2 G_0}{\partial x' \partial y'} + \hat{n}'_y \frac{\partial^2 G_0}{\partial^2 y'} \right) \hat{y} \right) \right]
\end{aligned} \tag{2.19}$$

Note that,

$$|\boldsymbol{\rho} - \boldsymbol{\rho}'| = \sqrt{(\mathbf{x} - \mathbf{x}')^2 + (\mathbf{y} - \mathbf{y}')^2} \tag{2.20}$$

Using the following template for the first partial derivative,

$$\frac{\partial G_0}{\partial \alpha'} = -\frac{jk_0(\alpha' - \alpha)}{4|\boldsymbol{\rho} - \boldsymbol{\rho}'|} H_1^{(2)}(k_0|\boldsymbol{\rho} - \boldsymbol{\rho}'|), \quad \alpha \in x, y \quad (2.21)$$

Using the following template for the second partial derivative,

$$\begin{aligned} \frac{\partial^2 G_0}{\partial^2 \alpha'} &= -\frac{jk_0^2(\alpha - \alpha')^2}{4|\boldsymbol{\rho} - \boldsymbol{\rho}'|} H_1^{(2)}(k_0|\boldsymbol{\rho} - \boldsymbol{\rho}'|) \\ &\quad - \frac{jk_0(\alpha - \alpha')^2}{4|\boldsymbol{\rho} - \boldsymbol{\rho}'|^3} H_0^{(2)}(k_0|\boldsymbol{\rho} - \boldsymbol{\rho}'|) \\ &\quad + \frac{jk_0}{4|\boldsymbol{\rho} - \boldsymbol{\rho}'|} H_0^{(2)}(k_0|\boldsymbol{\rho} - \boldsymbol{\rho}'|), \quad \alpha \in x, y \end{aligned} \quad (2.22)$$

The partial  $xy$  derivative can be derived as follows,

$$\begin{aligned} \frac{\partial^2 G_0}{\partial x' \partial y'} &= -\frac{jk_0^2(x - x')(y - y')}{4|\boldsymbol{\rho} - \boldsymbol{\rho}'|} H_1^{(2)}(k_0|\boldsymbol{\rho} - \boldsymbol{\rho}'|) \\ &\quad - \frac{jk_0(x - x')(y - y')}{4|\boldsymbol{\rho} - \boldsymbol{\rho}'|^3} H_0^{(2)}(k_0|\boldsymbol{\rho} - \boldsymbol{\rho}'|) \end{aligned} \quad (2.23)$$

## 2.3 Formulation

This section will explain how the 2D EFIE, (2.4), derived in Section 2.2 is used with MoM to calculate the scattering from a PEC structure. To solve (2.4) the boundary,  $\Gamma_0$ , can be divided up into small segments shown in Figure 2.2.

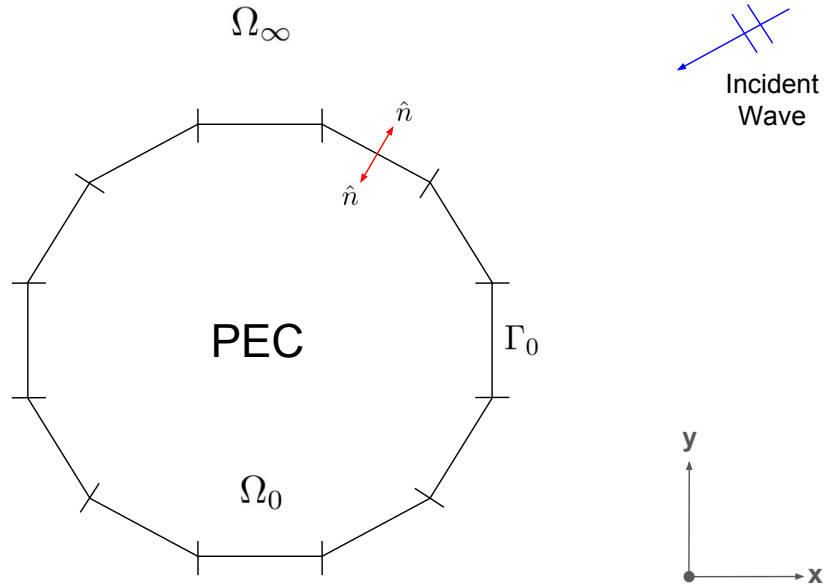


Figure 2.2: Two-dimensional segmented structure in free space.

Enforcing the boundary condition that the tangential electric field is zero on the surface of the structure gives (2.24). Equation (2.25) is derived from Faraday's law, (2.5), and  $\hat{n} \times \mathbf{H} = \mathbf{J}$ . After some careful manipulation of the two equations, the result is (2.25). Substituting (2.24) and (2.25) into (2.4) results in (2.26), which is the 2D EFIE for a PEC structure.

$$E_z(\boldsymbol{\rho}') = 0, \quad \boldsymbol{\rho}' \in \Gamma_0 \quad (2.24)$$

$$\frac{\partial E_z(\boldsymbol{\rho}')}{\partial n'} = jk_0 Z_0 J_z(\boldsymbol{\rho}'), \quad \boldsymbol{\rho}' \in \Gamma_0 \quad (2.25)$$

$$E_z^{\text{inc}}(\boldsymbol{\rho}) - jk_0 Z_0 \int_{\Gamma_0} J_z(\boldsymbol{\rho}') G_0(\boldsymbol{\rho}, \boldsymbol{\rho}') d\Gamma' = 0, \quad \boldsymbol{\rho} \in \Gamma_0 \quad (2.26)$$

The 2D EFIE for a PEC structure in (2.26) can be represented by

$$\mathcal{L}(J_z(\boldsymbol{\rho}')) = E_z^{\text{inc}}(\boldsymbol{\rho}) \quad (2.27)$$

with

$$\mathcal{L}(X) = jk_0 Z_0 \int_{\Gamma_0} X G_0(\boldsymbol{\rho}, \boldsymbol{\rho}') d\Gamma' \quad (2.28)$$

In (2.27),  $\mathcal{L}$  is the integral operator,  $J_z$  is the unknown current source and  $E_z^{\text{inc}}$  is the excitation source.

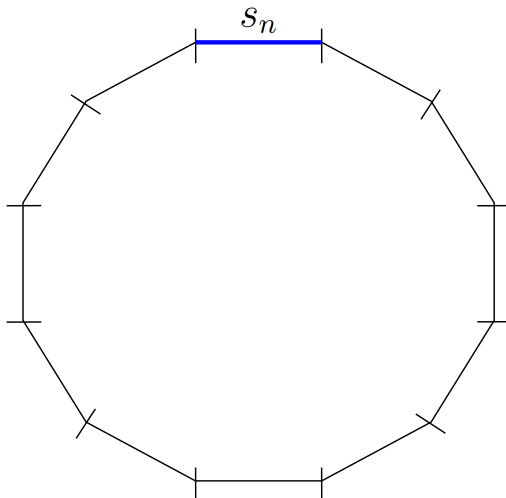
Basis functions are chosen to approximate the unknown function, which is the unknown current for the case at hand. There are two types of basis functions - entire domain and sub-sectional. Entire domain basis functions are easy to formulate if the surface of the structure is regular, otherwise it can be very difficult. Sub-sectional basis functions are easier to formulate as the structure surface can be divided into smaller segments.

Pulse basis functions will be used. The pulse basis function is a simple approximation to the solution on each segment. The pulse basis function is defined in equation (2.29), where  $s_n$  is the  $n$ -th segment, shown in Figure 2.3 [15].

$$f_n(\boldsymbol{\rho}) = \begin{cases} 1, & \boldsymbol{\rho} \in s_n \\ 0, & \text{elsewhere} \end{cases} \quad (2.29)$$

Other basis functions include the piecewise linear basis functions which use piecewise equations to model the current over two adjacent segments and piecewise sinusoidal basis functions, which use a sinusoidal to model the current over two adjacent segments [15].

The unknown current is expanded into  $N$  weighted basis functions,  $N$  being the number of segments  $\Gamma_0$  has been divided into.

Figure 2.3: A segment,  $S_n$ , from a structure in free space.

$$J_z(\boldsymbol{\rho}') = \sum_{n=1}^N I_n f_n(\boldsymbol{\rho}') \quad (2.30)$$

Where  $I_n$  is the unknown weighting coefficients yet to be determined. Substitution of (2.30) into (2.27) and multiplying with a weighting function and integrating over the whole domain again, results in the equation below.

$$\sum_{n=1}^N I_n \mathcal{L}(J_z(\boldsymbol{\rho}')) = E_z^{\text{inc}}(\boldsymbol{\rho}) \quad (2.31)$$

The method chosen for the weighting functions is point collocation. Other methods include Galerkin's method. Point collocation is equivalent to enforcing the boundary condition at the center of each segment [2]. The weighting function is defined in (2.32), where  $\boldsymbol{\rho}_m$  is the center of the  $m$ -th segment.

$$w_m(\boldsymbol{\rho}) = \delta(\boldsymbol{\rho} - \boldsymbol{\rho}_m), \quad m = 1, 2, \dots, N \quad (2.32)$$

Next, (2.31) is converted into a matrix equation by testing it with  $w_m$  and integrating over the entire solution domain,  $\Gamma_0$ . This yields

$$\sum_{n=1}^N I_n \int_{\Gamma_0} w_m \mathcal{L}(J_z(\boldsymbol{\rho}')) d\Gamma' = \int_{\Gamma_0} w_m E_z^{\text{inc}}(\boldsymbol{\rho}) d\Gamma', \quad m = 1, 2, \dots, N \quad (2.33)$$

This results in a set of linear equations which can be written in matrix form.

$$[A]\{I\} = \{b\} \quad (2.34)$$

With A being the system matrix, of dimension  $N \times N$ , defined as

$$A_{mn} = \int_{\Gamma_0} w_m \mathcal{L}(J_z(\boldsymbol{\rho}')) d\Gamma', \quad m, n = 1, 2, \dots, N \quad (2.35)$$

and  $b$  being the source vector defined as

$$b_m = \int_{\Gamma_0} w_m E_z^{\text{inc}}(\boldsymbol{\rho}) d\Gamma', \quad m = 1, 2, \dots, N \quad (2.36)$$

Solving (2.26) will give the following system of equations using MoM, i.e. a discretized, weighted residual approach.

$$\sum_{n=1}^N A_{mn} I = b_m, \quad m = 1, 2, \dots, N \quad (2.37)$$

The integral in (2.35) is evaluated using Gaussian quadrature of sufficiently high order. When  $m = n$ , the small argument for the Hankel function is used as shown below.

$$A_{mm} = \frac{k_0 Z_0 w_n}{4} \left[ 1 - \frac{2j}{\pi} \ln \left( \frac{k_0 \gamma w_n}{4e} \right) \right] \quad (2.38)$$

Once the surface current density is known, by solving the system of equations, the field at any observation point can be computed using (2.39).

$$E_z(\boldsymbol{\rho}) = E_z^{\text{inc}}(\boldsymbol{\rho}) - j k_0 Z_0 \int_{\Gamma_0} J_z(\boldsymbol{\rho}') G_0(\boldsymbol{\rho}, \boldsymbol{\rho}') d\Gamma', \quad \boldsymbol{\rho} \in \Omega_\infty \quad (2.39)$$

An important parameter in scattering is the measure of the reflective strength of a target [16]. This is usually represented by its echo area or radar cross section (RCS) ( $\sigma$ ). Bi-static RCS is the energy reflected in any direction other than the incident or opposite of the incident direction. For a 2D target, the parameter is referred to as the scattering width (SW). Equation (2.40) is used to calculate the bi-static SW [14].

$$\sigma_{2D} = \lim_{\rho \rightarrow \infty} \left[ 2\pi\rho \frac{|E^{\text{scat}}(\boldsymbol{\rho})|^2}{|E^{\text{inc}}(\boldsymbol{\rho})|^2} \right] \quad (2.40)$$

## 2.4 Verification

The derived MoM solution, (2.37), will be evaluated using two test cases shown in Figure 2.4. A plane wave with an incident angle of  $0^\circ$  and an excitation frequency of 300MHz will be used to illuminate the structures. The mesh size for the MoM code is decreased from  $\frac{\lambda_0}{2}$  to  $\frac{\lambda_0}{64}$  in the test cases. This will show the convergence of the MoM solution. The SW will be plotted against the FEKO results for the same 2D structures [17].

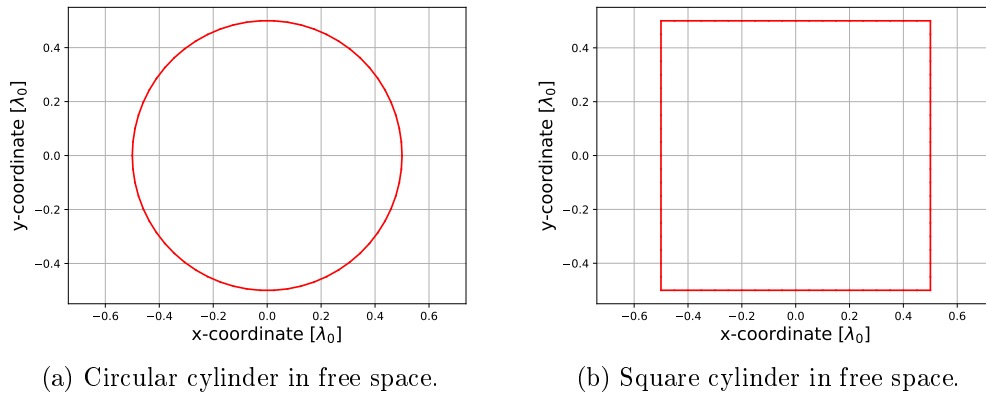


Figure 2.4: Validation structures.

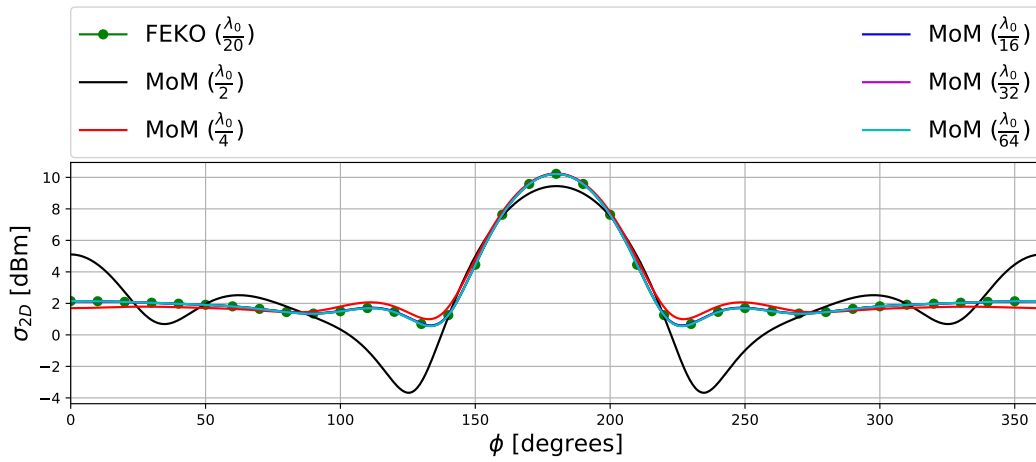


Figure 2.5: Circular cylinder bi-static SW.

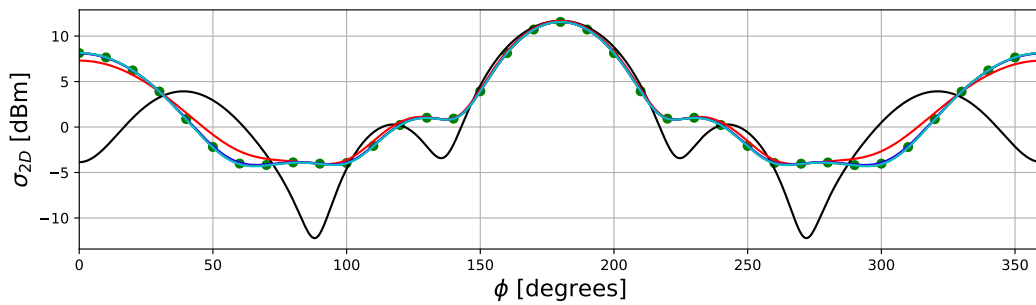


Figure 2.6: Square cylinder bi-static SW.

Figures 2.5 and 2.6 show the SW results for each of the structures. The legend shows the method used together with the size of the mesh in brackets.

For both the circular and square cylinders, when a coarse mesh is used,  $\frac{\lambda_0}{2}$ , the results are not very accurate compared with the FEKO results. As the mesh size decreases, the accuracy of the SW results increases. For both the circular and square cylinder, the SW converges when a mesh size greater than  $\frac{\lambda_0}{4}$  is used. Thus for the rest of the thesis a mesh size of  $\frac{\lambda_0}{10}$  will be used.

## 2.5 Conclusion

The results shown in Figures 2.5 and 2.6 demonstrate that MoM has been implemented correctly. This implementation will be used as the benchmark for evaluations in the rest of the thesis.



# Chapter 3

## MRPO and IPO

### 3.1 Introduction

This chapter will give a brief overview of the physical optics (PO) approximation. Next, an in-depth description of the multiple reflection physical optics (MRPO) and the iterative physical optics (IPO) formulations will be presented. Once the formulations have been discussed, the results for MRPO and IPO will be evaluated against the MoM formulation from Chapter 2.

### 3.2 Physical Optics

Consider the 2D PEC structure with a closed surface  $\Gamma_0$  in Figure 3.1. When the surface,  $\Gamma_0$ , is divided into  $N$  segments, each of the segments will have a positive and negative unit normal,  $\hat{n}_p$  and  $\hat{n}_n$  respectively. Note that  $\hat{n}$  represents the outward pointing normal vector. The positive and negative normal vectors will be used later, when discussing open structures.

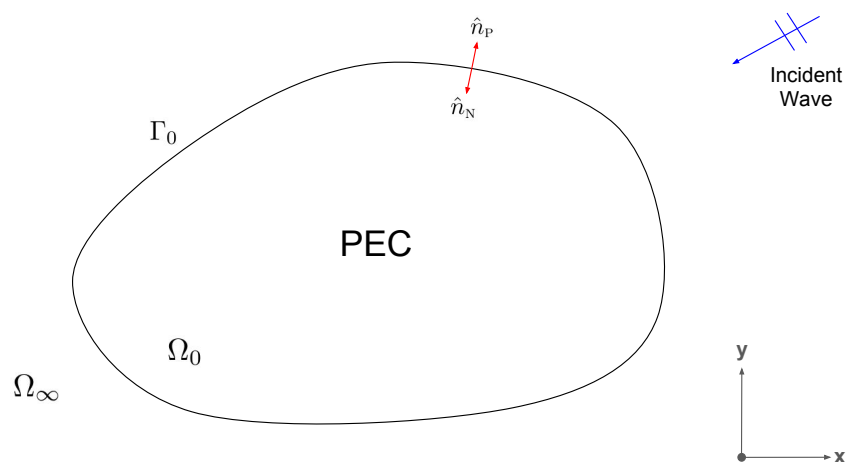


Figure 3.1: PEC structure in free space.

The PO approximation is as follows:

$$\mathbf{J}^{\text{PO}}(\boldsymbol{\rho}) = \begin{cases} 2\hat{\mathbf{n}} \times \mathbf{H}^{\text{inc}}(\boldsymbol{\rho}), & \text{visible} \\ 0, & \text{not visible} \end{cases} \quad (3.1)$$

The induced surface current density due to the incident magnetic field can be calculated using the first-order PO approximation (3.1) [4]. A segment is visible if there are no obstructions, from  $\Gamma_0$ , in the direct line-of-sight between the segment and source.

According to image theory, in the case of the PEC half-space, the PO approximation, (3.1), becomes exact. Therefore, the PO approximation will become increasingly more accurate as the electrical size of the object increases. This approximation does not support multiple reflections, it is a single reflection [14].

### 3.3 Multiple Reflection Physical Optics

The incident current solution for MRPO can be obtained as [18]:

$$\mathbf{J}^{\text{PO}}(\boldsymbol{\rho}) = 2\delta^{\text{inc}} \hat{\mathbf{n}} \times \mathbf{H}^{\text{inc}}(\boldsymbol{\rho}) \quad (3.2)$$

where the incident shadowing coefficient is

$$\delta_n^{\text{inc}} = \begin{cases} 1, & \text{if } s_n \text{ visible to source} \\ 0, & \text{if } s_n \text{ not visible to source} \end{cases} \quad (3.3)$$

Equation (3.2) is known as the single reflection physical optics (SRPO) solution. The discretized current solution can be obtained from (3.2)

$$\mathbf{J}_{(1)}^{\text{PO}}(\boldsymbol{\rho}) = 2 \sum_{n=1}^N \delta_n^{\text{inc}} \hat{\mathbf{n}} \times \mathbf{H}^{\text{inc}}(\boldsymbol{\rho}) \quad (3.4)$$

It is apparent that (3.2) can be applied successively. The current induced on the first reflection will become the source for the second reflection and so forth. This will need to take internal shadowing into account. The internal shadowing will be represented by  $\delta$ , which will be equal to unity for observation and source points visible to each other and zero otherwise.

Using the MFIE, the radiated magnetic field due to the current at  $\boldsymbol{\rho}$  can be formally expressed as

$$\mathbf{H}(\mathbf{J})(\boldsymbol{\rho}) = \int_{\Gamma_0} \nabla G_0(\boldsymbol{\rho}, \boldsymbol{\rho}') \times \mathbf{J}(\boldsymbol{\rho}') d\Gamma' \quad (3.5)$$

The current after the  $K$ -th reflection can be calculated using [18, 10]

$$\mathbf{J}_{(K+1)}^{\text{PO}}(\boldsymbol{\rho}) = \mathbf{J}_{(1)}^{\text{PO}}(\boldsymbol{\rho}) + 2\hat{\mathbf{n}} \times \mathbf{H}(\delta \mathbf{J}_{(K)}^{\text{PO}}(\boldsymbol{\rho}'))(\boldsymbol{\rho}) \quad (3.6)$$

A segment is visible to another segment if there are no obstructions, from  $\Gamma_0$ , in the direct line-of-sight between the two segments. The discretized current on each segment,  $N$ , is the total sum of the currents, induced by the magnetic field, on the other,  $M$ , segments. This will give the discretized current solution after  $K$  reflections shown below.

$$\mathbf{J}_{(K+1)}^{\text{PO}} = \mathbf{J}_{(1)}^{\text{PO}} + 2 \sum_{n=1}^N \sum_{m=1}^M \hat{n} \times \mathbf{H} \left( \delta_n^m (\mathbf{J}_{(K)})_m \right) \quad (3.7)$$

where

$$\delta_n^m = \begin{cases} 1, & \text{if } s_n \text{ visible to } s_m \\ 0, & \text{if } s_n \text{ not visible to } s_m \end{cases} \quad (3.8)$$

The MRPO implementation uses (3.7) in matrix form, which is shown below. Where the p and n denote the positive and negative sides of each segment.

$$\begin{Bmatrix} I_{(K+1)}^{\text{p}} \\ I_{(K+1)}^{\text{n}} \end{Bmatrix} = \begin{Bmatrix} I_{(1)}^{\text{p}} \\ I_{(1)}^{\text{n}} \end{Bmatrix} + [C_\delta] \begin{Bmatrix} I_{(K)}^{\text{p}} \\ I_{(K)}^{\text{n}} \end{Bmatrix} \quad (3.9)$$

Where an entry in the  $C_\delta$  matrix will look as follows,

$$(C_\delta)_{n,m} = 2\hat{n} \times \mathbf{H}(\delta_n^m \mathbf{J}_m^{\text{PO}}) \quad (3.10)$$

The discretized MRPO formulation can be succinctly expressed as

$$I_{(K+1)}^{\text{PO}} = I_{(1)}^{\text{PO}} + C_\delta I_{(K)}^{\text{PO}} \quad (3.11)$$

### 3.4 Iterative Physical Optics

Iterative physical optics solves (3.11) using a different shadowing coefficient,  $\gamma$ . This new shadowing coefficient is more relaxed than the MRPO shadowing coefficient. The incident current solution for IPO can be obtained as [18]:

$$\mathbf{J}_{(1)}^{\text{PO}}(\boldsymbol{\rho}) = 2\gamma^{\text{inc}} \hat{n} \times \mathbf{H}^{\text{inc}}(\boldsymbol{\rho}) \quad (3.12)$$

where the incident shadowing coefficient is

$$\gamma_n^{\text{inc}} = \begin{cases} 1, & \text{if source in } s_n \text{ half space} \\ 0, & \text{if source not in } s_n \text{ half space} \end{cases} \quad (3.13)$$

To determine if the source is in  $s_n$ 's half space, the elemental plane and normal vector,  $\hat{n}_n$ , must be pointing in opposite directions.

Applying (3.12) successively will give (3.14) which is the IPO current solution after the  $K$ -th iteration.

$$\mathbf{J}_{(K+1)}^{\text{PO}}(\boldsymbol{\rho}) = \mathbf{J}_{(1)}^{\text{PO}}(\boldsymbol{\rho}) + 2\hat{n} \times \mathbf{H}(\gamma \mathbf{J}_{(K)}^{\text{PO}}(\boldsymbol{\rho}'))(\boldsymbol{\rho}) \quad (3.14)$$

where

$$\gamma_n^m = \begin{cases} 1, & \text{if } s_n \text{ in } s_m \text{ half space} \\ 0, & \text{if } s_n \text{ not in } s_m \text{ half space} \end{cases} \quad (3.15)$$

To determine if  $s_n$  is in  $s_m$ 's half space, let  $\mathbf{R}' = \boldsymbol{\rho}_m - \boldsymbol{\rho}_n$ , where  $\boldsymbol{\rho}_m$  and  $\boldsymbol{\rho}_n$  are the centers of  $s_m$  and  $s_n$ . Thus  $s_n$  is in  $s_m$  half space if  $\hat{n}_m \cdot \mathbf{R}' < 0$ . This is known as the IPO shadowing rule. By definition the equivalent currents radiate in free space regardless of which way they are facing [12].

The IPO formulation is the same as the MRPO formulation. The only difference being the shadowing coefficient. Thus the IPO can be written in the same matrix form as (3.9)

$$\begin{Bmatrix} I_{(K+1)}^{\text{P}} \\ I_{(K+1)}^{\text{n}} \end{Bmatrix} = \begin{Bmatrix} I_{(1)}^{\text{P}} \\ I_{(1)}^{\text{n}} \end{Bmatrix} + [C_\gamma] \begin{Bmatrix} I_{(K)}^{\text{P}} \\ I_{(K)}^{\text{n}} \end{Bmatrix} \quad (3.16)$$

Where an entry in the  $C_\gamma$  matrix will look as follows

$$(C_\gamma)_{n,m} = 2\hat{n} \times \mathbf{H}(\gamma_n^m \mathbf{J}_m^{\text{PO}}) \quad (3.17)$$

The discretized IPO formulation can be succinctly expressed as

$$I_{(K+1)}^{\text{PO}} = I_{(1)}^{\text{PO}} + C_\gamma I_{(K)}^{\text{PO}} \quad (3.18)$$

The iterations will run until convergence. If the convergence error,  $\mathcal{E}$ , is less than a predetermined value, the solution has converged. The error convergence is defined below:

$$\mathcal{E} = \frac{|I_{(K+1)}^{\text{PO}} - I_{(K)}^{\text{PO}}|}{I_{(1)}^{\text{PO}}}, \quad I_{(1)}^{\text{PO}} > 0 \quad (3.19)$$

Practical solution of the IPO recursive matrix expression, has been divided into 3 sub-categories: fixed-point, combined systems and relaxed. Each of these categories will be discussed in more detail in the next sections.

### 3.4.1 Fixed Point Iterations

There are various ways to solve a linear system,  $Ax = b$ , iteratively. Methods such as Jacobi, Gauss-Seidel, successive over relaxation (SOR) and symmetric successive over relaxation (SSOR) are based on the splitting of the  $A$  matrix to obtain a recursive iterative scheme [19]. The splitting of  $A$  is

$$A = M - N \quad (3.20)$$

The methods have the following form [20],

$$Mx_{K+1} = Nx_K + b \quad (3.21)$$

The IPO formulation, (3.18), can be converted to a fixed point problem as follows,

$$MI_{(K+1)}^{\text{PO}} = NI_{(K)}^{\text{PO}} + I_{(1)}^{\text{PO}} \quad (3.22)$$

The  $A$  matrix can be decomposed using the LDU decomposition such that  $D$  is the identity matrix,  $L$  is the strict lower matrix and  $U$  is the strict upper matrix [20].

$$A = D - L - U \quad (3.23)$$

The splittings of the  $A$  matrix,  $M$  and  $N$ , are set to a combination of the decomposed parts of the  $A$  matrix. For the IPO formulation, the  $A$  matrix is given as follows,

$$A = (\mathcal{I} + C_\gamma) \quad (3.24)$$

The Jacobi, Gauss-Seidel, SOR and SSOR methods will be discussed in detail next. The values of  $M$  and  $N$  will be given in terms of the LDU decomposition.

### 3.4.1.1 Jacobi Iteration

The first method to be discussed is the Jacobi iteration. The Jacobi iteration is only defined for systems that have a non-zero diagonal  $A$  matrix. The Jacobi iteration splits the  $A$  matrix as follows,

$$\begin{aligned} M &= D \\ N &= L + U \end{aligned} \quad (3.25)$$

Thus the  $K$ -th iteration for the Jacobi iteration will be

$$x_{(K+1)} = D^{-1}(L + U)x_{(K)} + D^{-1}b \quad (3.26)$$

The Jacobi iteration does not make use of the most recent information when calculating  $x_{(K+1)}$ . For example,  $(x_{(K)})_1$  is used in the calculation of  $(x_{(K+1)})_2$  even though  $(x_{(K+1)})_1$  is known. Only once it has completed the  $(K + 1)$ -th iteration does it update the values in the matrix [21, 20, 19].

The implementation of the Jacobi iteration for (3.18) is shown below.

$$I_{(K+1)}^{\text{PO}} = D^{-1}(L + U)I_{(K)}^{\text{PO}} + D^{-1}I_{(1)}^{\text{PO}} \quad (3.27)$$

### 3.4.1.2 Gauss-Seidel Iteration

The Gauss-Seidel iteration is very similar to the Jacobi iteration. The difference between the two iterations is that the Gauss-Seidel method updates the  $n$ -th component immediately instead of at the end of the  $K$ -th iteration [19].

The Gauss-Seidel splits the  $A$  matrix up as follows,

$$\begin{aligned} M &= D + L \\ N &= U \end{aligned} \quad (3.28)$$

Thus the  $K$ -th iteration for the Gauss-Seidel iteration will be

$$x_{(K+1)} = (D + L)^{-1}Ux_{(K)} + (D + L)^{-1}b \quad (3.29)$$

The implementation of the Gauss-Seidel iteration for (3.18) is shown below.

$$I_{(K+1)}^{\text{PO}} = (D + L)^{-1}UI_{(K)}^{\text{PO}} + (D + L)^{-1}I_{(1)}^{\text{PO}} \quad (3.30)$$

### 3.4.1.3 SOR Iteration

The successive over relaxation (SOR) iteration adds a relaxation parameter,  $\omega$ , to the Gauss-Seidel iteration. The SOR splits the  $A$  matrix up as follows,

$$\begin{aligned} M &= D + \omega L \\ N &= (1 - \omega)D - \omega U, \quad \text{with } 0 \leq \omega \leq 1 \end{aligned} \quad (3.31)$$

Thus the  $K$ -th iteration for the SOR iteration will be [19]

$$x_{(K+1)} = ((D + \omega L)^{-1}((1 - \omega)D - \omega U)x_{(K)} + ((D + \omega L)^{-1}b \quad (3.32)$$

The implementation of the SOR iteration for (3.18) is shown below.

$$I_{(K+1)}^{\text{PO}} = ((D + \omega L)^{-1}((1 - \omega)D - \omega U)I_{(K)}^{\text{PO}} + ((D + \omega L)^{-1}I_{(1)}^{\text{PO}} \quad (3.33)$$

### 3.4.1.4 SSOR Iteration

SOR can be thought of as the forward step in symmetric successive over relaxation (SSOR). The forward step is shown in (3.35) and the backward step is shown in (3.36) [21, 20], with  $0 \leq \omega \leq 1$ . The SSOR splits the  $A$  matrix up into two steps as follows,

$$\begin{aligned}
M_{\frac{1}{2}} &= D + \omega L \\
N_{\frac{1}{2}} &= (1 - \omega)D - \omega U \\
M_1 &= D + \omega U \\
N_1 &= (1 - \omega)D - \omega L
\end{aligned} \tag{3.34}$$

Thus the  $K$ -th iteration for the SSOR iteration will be [20]

$$x_{(K+\frac{1}{2})} = ((D + \omega L)^{-1}((1 - \omega)D - \omega U)x_{(K)} + ((D + \omega L)^{-1}b \tag{3.35}$$

$$x_{(K+1)} = ((D + \omega U)^{-1}((1 - \omega)D - \omega L)x_{(K+\frac{1}{2})} + ((D + \omega U)^{-1}b \tag{3.36}$$

This gives the recurrence,

$$x_{(K+1)} = G_\omega x_{(K)} + F_\omega b \tag{3.37}$$

Substituting (3.35) into (3.36),  $G_\omega$  can be calculated to be

$$G_\omega = (D - \omega L)^{-1}(\omega U + (1 - \omega)D) \times (D - \omega U)^{-1}(\omega L + (1 - \omega)D) \tag{3.38}$$

and  $F_\omega$  can be calculated to be

$$F_\omega = \omega(2 - \omega)(D - \omega U)^{-1}D(D - \omega L)^{-1} \tag{3.39}$$

The implementation of the SSOR iteration for (3.18) is shown below.

$$I_{(K+1)}^{\text{PO}} = F_\omega I_{(1)}^{\text{PO}} + G_\omega I_{(K)}^{\text{PO}} \tag{3.40}$$

### 3.4.2 Combined System Methods

Under the assumption that for sufficiently large  $K$ ,  $I_{(K+1)}^{\text{PO}} = I_{(K)}^{\text{PO}} = I^{\text{PO}}$ , one obtains

$$\mathcal{I}I^{\text{PO}} = I_{(1)}^{\text{PO}} + C_\gamma I^{\text{PO}} \tag{3.41}$$

with  $\mathcal{I}$  being an identity matrix. This can be transformed into a linear equation shown in (3.42).

$$(\mathcal{I} - C_\gamma)I^{\text{PO}} = I_{(1)}^{\text{PO}} \tag{3.42}$$

Transforming (3.41) into (3.42) opens up many doors to different types of solvers to use. Many ways exist to solve the system of linear equations  $Ax = b$ .

The three methods, direct solution, generalized minimal residual method (GMRES) and Jacobi minimal residual method (JMRES) will be discussed in more detail next. The first method solves (3.42) by calculating the inverse of  $(\mathcal{I} - C_\gamma)$ . The latter two methods solve (3.42) iteratively.

### 3.4.2.1 Direct Solution

The most basic method is to take the inverse of  $A$  and multiply it by  $b$  to solve for  $x$  shown below. This is known as the direct solution.

$$Ax = b \quad (3.43)$$

$$x = A^{-1}b \quad (3.44)$$

The implementation of (3.44) can be represented in the formal notation below

$$I^{\text{PO}} = (\mathcal{I} - C_\gamma)^{-1} I_{(1)}^{\text{PO}} \quad (3.45)$$

### 3.4.2.2 GMRES Iteration

The Generalized minimal residual method (GMRES) is a projection method that is used to solve a linear system,  $Ax = b$ . GMRES is based on taking  $\mathcal{K} = \mathcal{K}_n$  and  $\mathcal{L} = A\mathcal{K}_n$  where  $\mathcal{K}_n$  is the  $n$ -th Krylov subspace. The Krylov subspaces are used to find an approximate solution, with minimal residual,  $r$  [20, 19].

The  $n$ -th Krylov sequence can be defined below

$$\mathcal{K} = \mathcal{K}(A, b) = \text{span}\{A^0b, A^1b, A^2b, \dots, A^{n-1}b\} \quad (3.46)$$

GMRES uses Arnoldi vectors to express the iterates of the solution by the vector,  $x_K \in \mathcal{K}_n$ . This vector minimizes the residual,  $r$ .

The vectors  $A^0b, A^1b, A^2b, \dots, A^{n-1}b$  will be linearly independent for non-singular  $A$  matrix. The Arnoldi iteration is used to find orthonormal vectors  $q_1, q_2, \dots, q_n$ , which will be the basis for  $\mathcal{K}$ . The  $x_n$  vector can then be written as  $x_n = \mathcal{Q}_n y_n$ , where  $\mathcal{Q}_n$  is an  $m \times n$  matrix formed by the  $q_1, q_2, \dots, q_n$ .

The Arnoldi iteration process produces Hessenberg matrix,  $\mathcal{H}_n$ , of the form  $(n+1) \times n$ , such that

$$A\mathcal{Q}_n = \mathcal{Q}_{n+1}\mathcal{H}_n \quad (3.47)$$

With the columns of the  $\mathcal{Q}_n$  being orthonormal, the initial equation can be made to equal

$$\|Ax - b\| = \|\mathcal{H}_n y_n - \beta e_1\| \quad (3.48)$$

With  $e = \{1, 0, 0, \dots, 0\}^T$  and  $\beta = \|Ax_0 - b\|$ ,  $x_0$  is the first trial vector.  $x_n$  can be found by minimizing the norm of the residual, which is a linear least squares problem of size  $n$ .

$$r_n = \mathcal{H}_n y_n - \beta e_1 \quad (3.49)$$

The algorithm described below is known as an unlimited GMRES. When the restart value is equal to infinity, all of the previous iterations are taken



into account. For practicality, a restart value is usually used in GMRES to avoid excessive amounts of computations and memory use.

---

**Algorithm 1** Unlimited GMRES algorithm
 

---

```

 $r_0 = b - Ax_0$ 
 $h_{1,0} = \|r_0\|_2$ 
 $k = 0$ 
while ( $h_{k+1,k} > 0$ ) do
   $q_{k+1} = r_k / h_{k+1,k}$ 
   $k = k + 1$ 
   $r_k = Aq_k$ 
  for ( $i = 1 : k$ ) do
     $h_{i,k} = q_i^T r_k$ 
     $r_k = r_k - h_{i,k}q_i$ 
  end for
   $h_{k+1,k} = \|r_k\|_2$ 
   $x_k = x_0 + Q_k y_k$ 
end while
 $x = x_k$ 

```

---

### 3.4.2.3 JMRES Iteration

The Jacobi Minimal Residual method (JMRES) is based on the GMRES method described in the previous section. It can be proven to be mathematically equivalent to GMRES but using a restart value of 2 instead of saving all of the previous iteration history [11]. The JMRES algorithm is described below in pseudocode,

---

**Algorithm 2** JMRES algorithm

---

```

1:  $r_0 = b - \mathbf{A}x_0$ 
2:  $k = 0$ 
3: while ( $h_{k+1,k} > 0$ ) do
4:    $k = k + 1$ 
5:    $q_1 = b - r_k$ 
6:    $q_2 = Ar_k$ 
7:    $H_{11} = \langle q_1, q_1 \rangle$ 
8:    $H_{12} = \langle q_1, q_2 \rangle$ 
9:    $H_{21} = H_{12}^*$ 
10:   $H_{22} = \langle q_2, q_2 \rangle$ 
11:   $v_1 = \langle q_1, b \rangle$ 
12:   $v_2 = \langle q_2, b \rangle$ 
13:   $[\alpha] = [H]^{-1}[v]$ 
14:   $x_k = \alpha_1 x_{k-1} + \alpha_2 r_{k-1}$ 
15:   $r_k = b - \alpha_1 q_1 + \alpha_2 q_2$ 
16: end while
17:  $x = x_k$ 

```

---

**3.4.2.4 Other methods**

Other iterative solvers for the combined system investigated included the conjugate gradient method, bi-conjugate gradient method and the bi-conjugate gradient stabilized method. The GMRES algorithm was found to be much more rapidly converging than the conjugate and bi-conjugate gradient methods [22]. Thus they have been ignored in this investigation.

**3.4.3 Relaxed Method**

The Relaxed Jacobi method mentioned in [12], uses the information from the previous iteration to help the accuracy of the final solution. The Relaxed Jacobi method has a general form shown below in equation (3.50).

$$I_{(K+1)}^{\text{PO}} = \alpha I_{(1)}^{\text{PO}} + (1 - \alpha) I_{(K-1)}^{\text{PO}} + C_\gamma I_{(K)}^{\text{PO}}, \quad \text{with } 0 \leq \alpha \leq 1 \quad (3.50)$$

## 3.5 MRPO and IPO Evaluation

In this section the methods discussed in Sections 3.3 and 3.4 will be evaluated with the MoM from Chapter 2, used to generate full-wave, reference results. The MRPO method will be evaluated in the first subsection followed by the evaluation of the several IPO methods. The best performing IPO schemes will then be compared against the MRPO in the next subsection. Modelling both the internal and external currents in case of closed structures, versus modelling only the external currents will be compared using the methods from the section before. Lastly, the influence upon performance of the  $\alpha$  parameter for the Relaxed Jacobi method, (3.50), will be investigated.

### 3.5.1 MRPO Performance Assessment

The MRPO method will first be tested on a simple corner reflector shown below. The incident angle will be set to  $0^\circ$  with an excitation frequency of 1GHz. The results for increasing numbers of reflections will be shown.

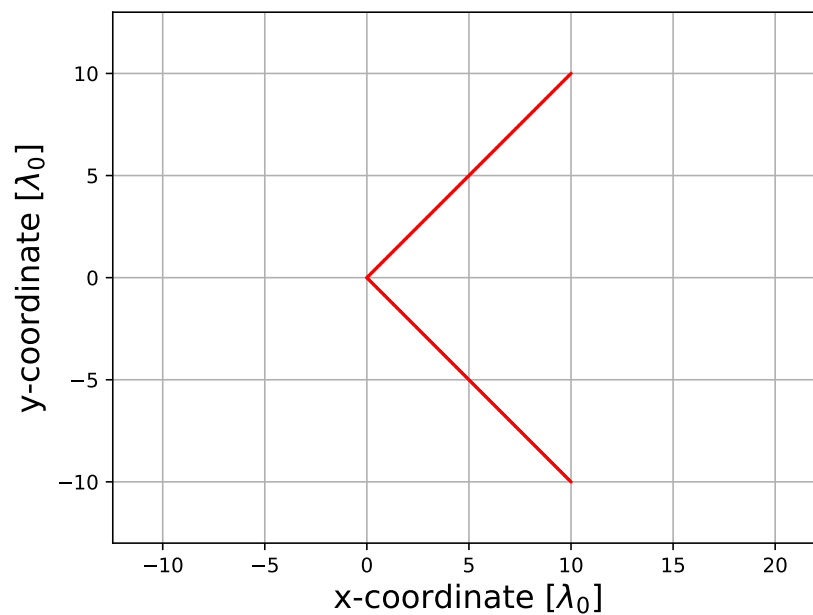
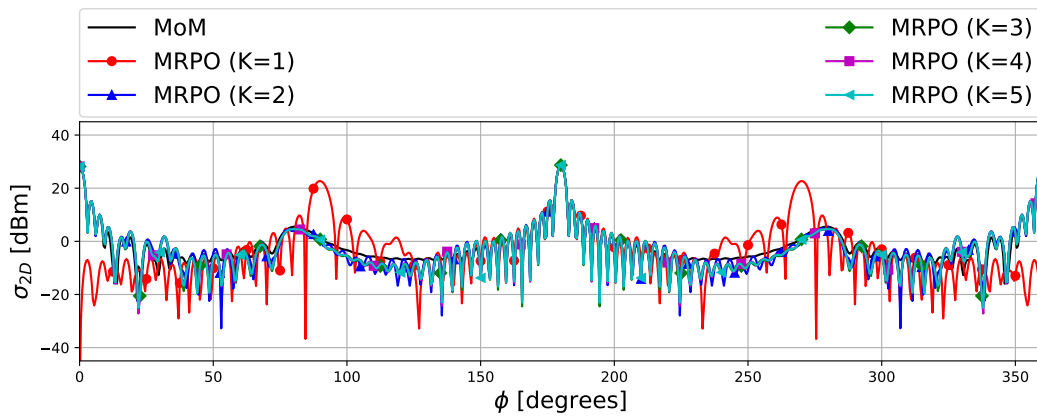
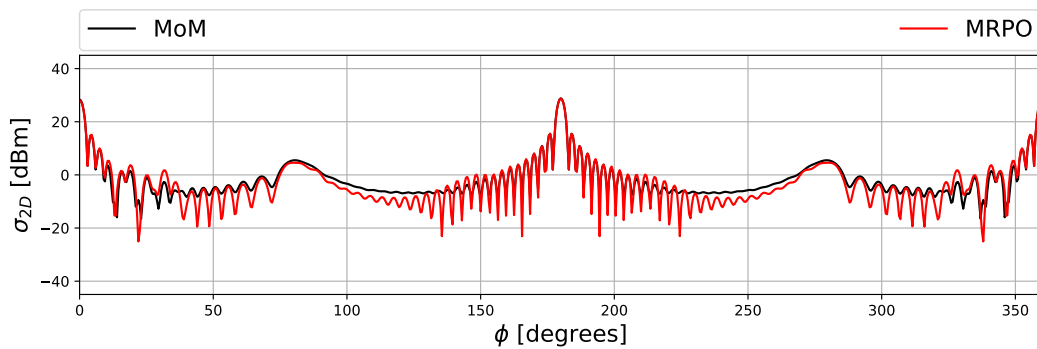


Figure 3.2: Corner reflector.



(a) Solution history.



(b) Final solution (K=5).

Figure 3.3: MRPO – Corner reflector bi-static SW.

Figure 3.3a shows that the results converges to the final results even if many reflections have been selected. After 2 reflections the solution converges to the final solution.

The MRPO implementation (3.11) will be evaluated on the test cases in Figure 3.4. The dimensions are indicated in wavelengths. There will be 3 sizes for each test case, "small", "medium" and "large". These will be  $1\times$ ,  $2\times$  and  $3\times$  the original size. The asymptotic behaviour is investigated as the electrical size is increased.

The test cases are chosen to include connected and disjointed structures, as well as open, almost closed and closed structures. Figure 3.4 shows that the structures contain normals on both side. This indicates that the current is being modelled on both sides on the geometry.

The incident plane wave angles for the line with angled edge, circle with a  $40^\circ$  opening and circle with a  $180^\circ$  opening is  $0^\circ$ . The irregular octagon has an incident plane wave angle of  $45^\circ$ . The plane wave angles will remain the same unless stated otherwise. The excitation frequency of the plane wave will

be set to 1GHz. The number of reflections,  $K$ , will be set to 10 except for the circle with a  $180^\circ$  opening which will be set to 50.

The test cases in Figure 3.4 will also be used in the IPO evaluation, MRPO and IPO evaluation and the  $\alpha$  parameter investigation later in the chapter.

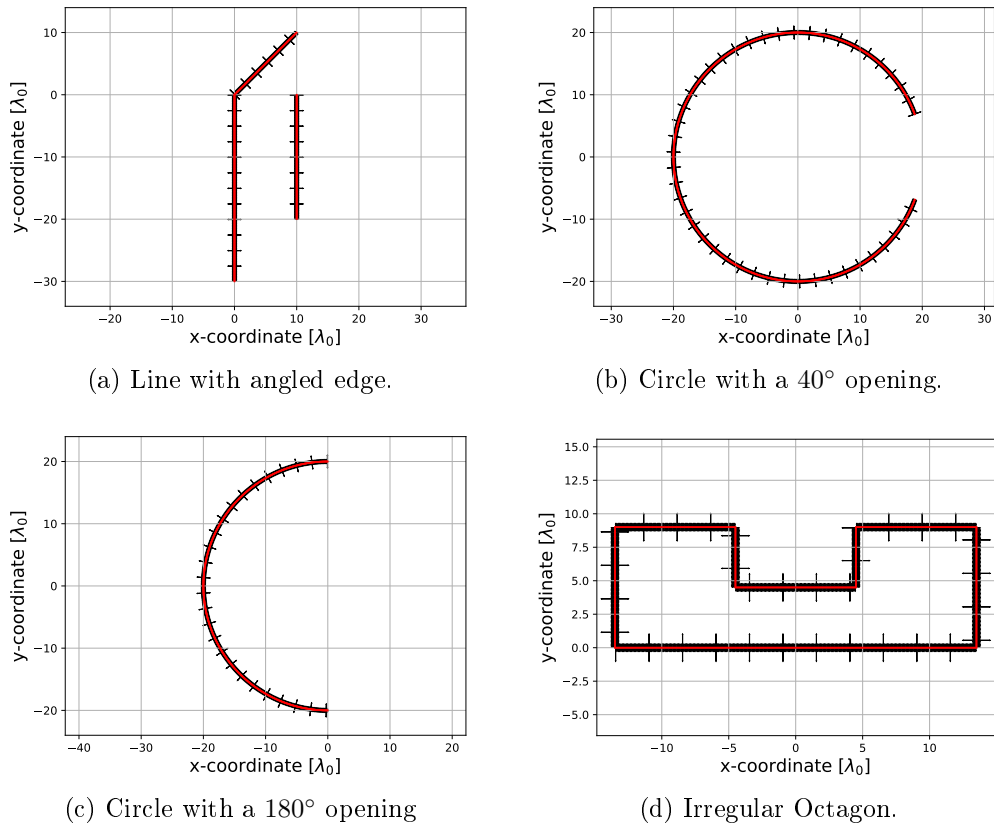
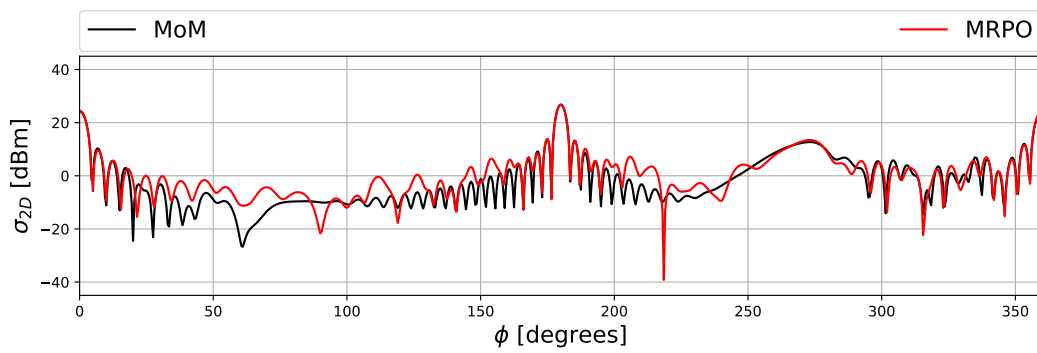
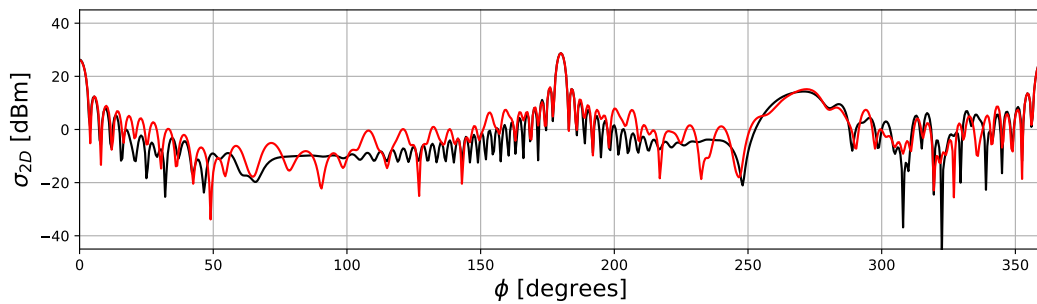


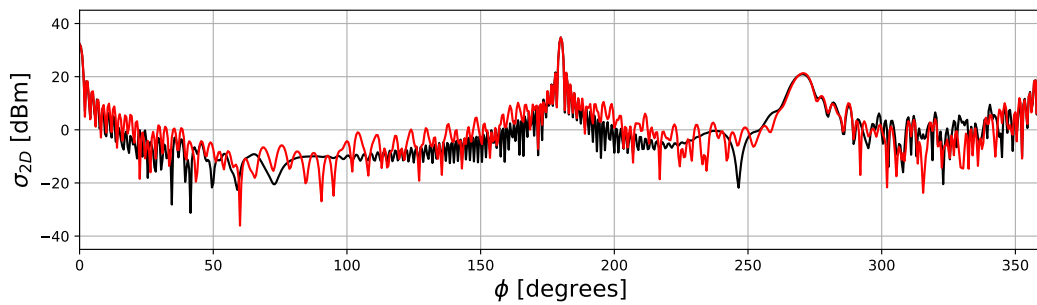
Figure 3.4: Test structures in free space.



(a) Small structure.



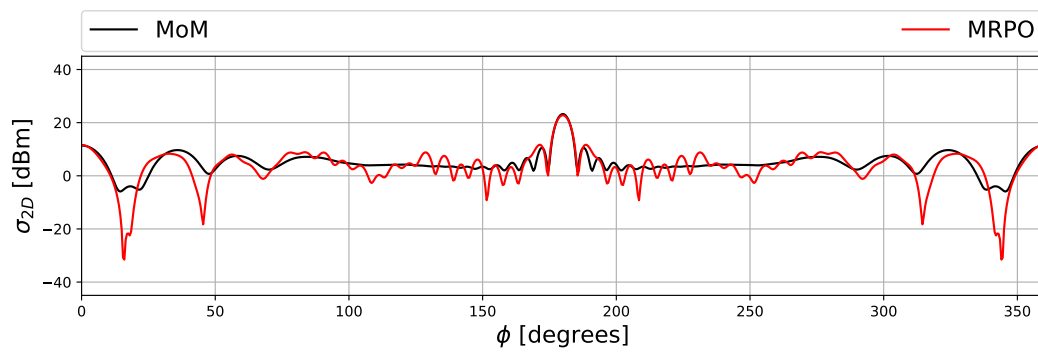
(b) Medium structure.



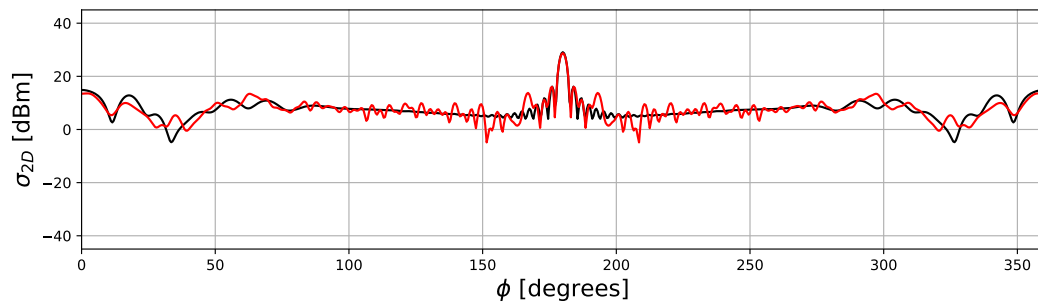
(c) Large structure.

Figure 3.5: MRPO – Line with angled edge bi-static SW.

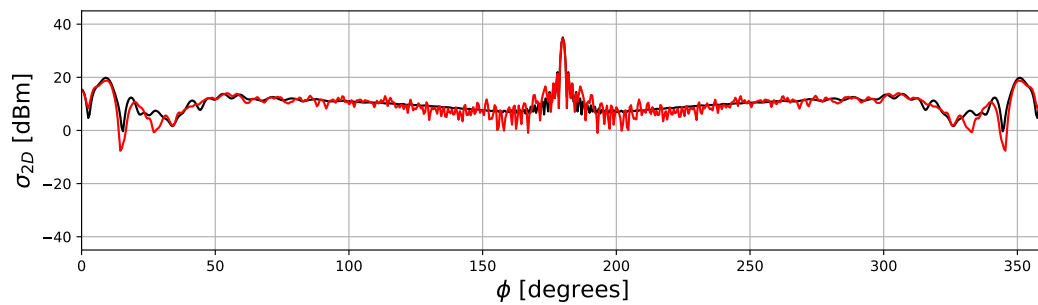
The two main lobes at  $0^\circ$  and  $180^\circ$ , in Figure 3.5, have been approximated very well for all three of the structure sizes. MRPO approximates the solution increasingly well, as the electrical size is increased. MRPO has approximated the reflection of the  $45^\circ$  angled plate well at  $270^\circ$ .



(a) Small structure.



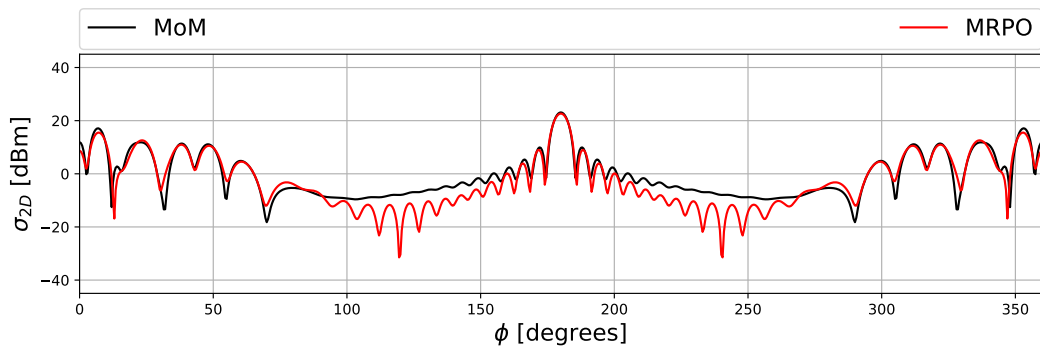
(b) Medium structure.



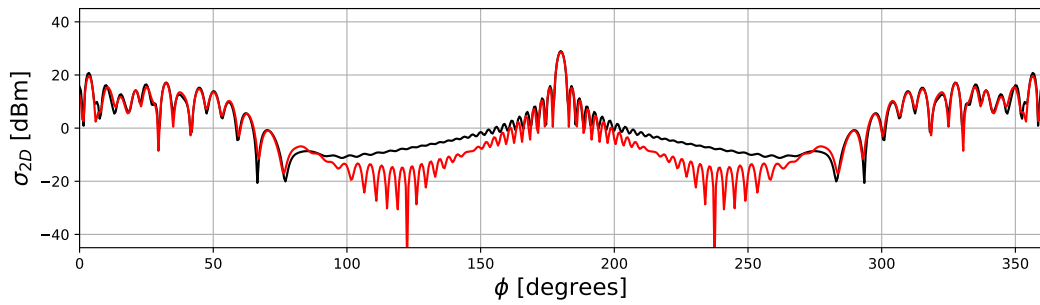
(c) Large structure.

Figure 3.6: MRPO – Circle with a  $40^\circ$  opening bi-static SW.

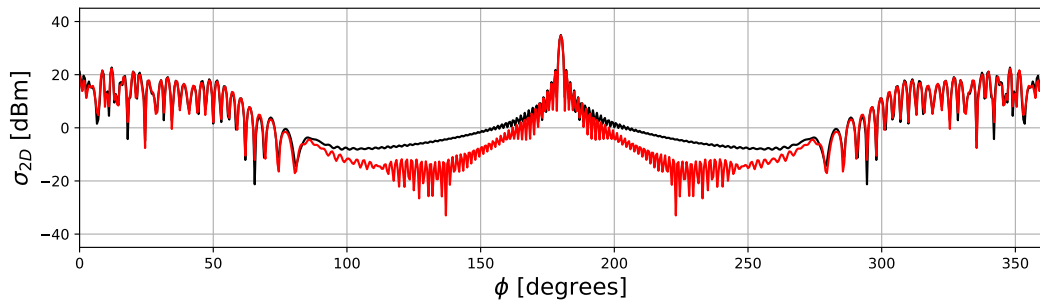
MRPO approximates the forward scattering of the circle with a  $40^\circ$  opening very well. Elsewhere, the scattering has not been approximated well. The small opening of the structure will cause many internal reflections to take place. This simulation was run with 50 reflection. Although these results are not uniformly accurate, it can be observed that they improve around  $0^\circ$ , as the electrical size grows.



(a) Small structure.



(b) Medium structure.

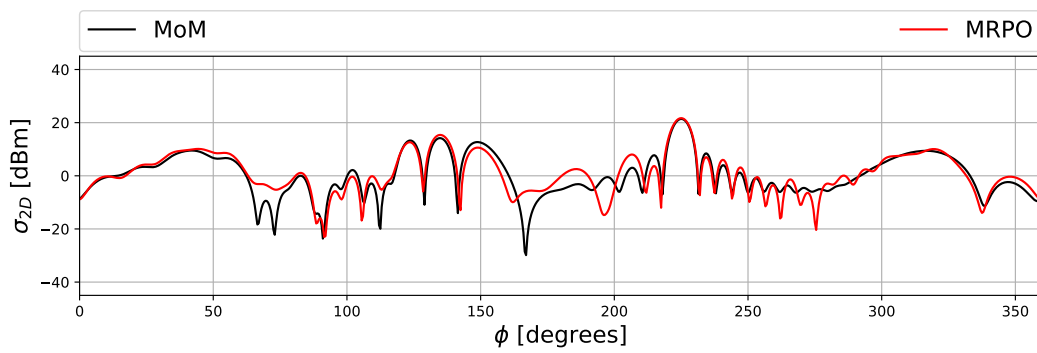


(c) Large structure.

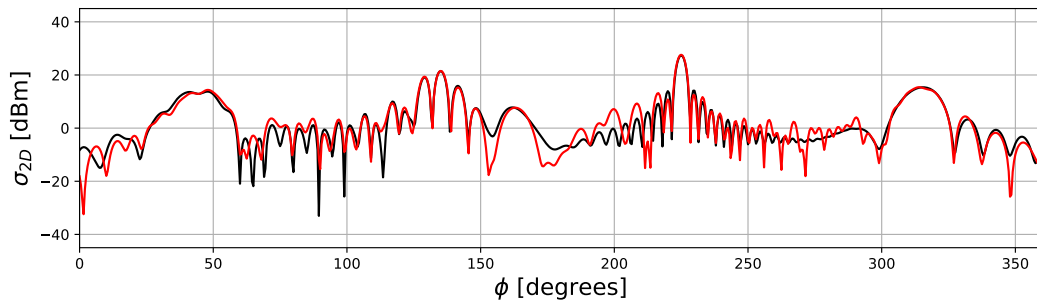
Figure 3.7: MRPO – Circle with a  $180^\circ$  opening bi-static SW.

Again, the forward scattering has been approximated very well by MRPO for all three structure sizes. The back scattering has also been approximated well compared to the circle with  $40^\circ$  opening. Much less reflections are needed to model the internal currents.

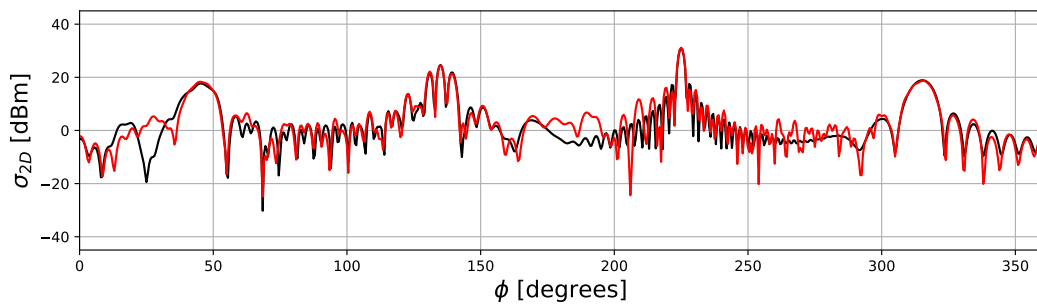




(a) Small structure.



(b) Medium structure.



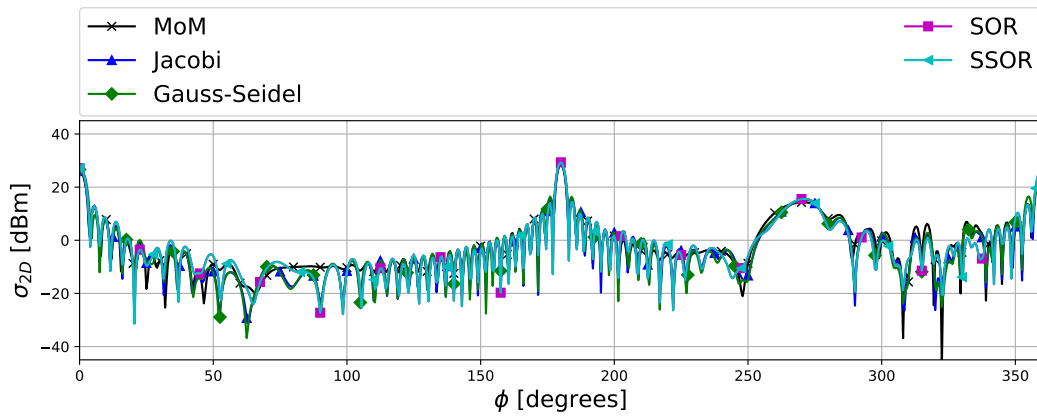
(c) Large structure.

Figure 3.8: MRPO – Irregular octagon bi-static SW.

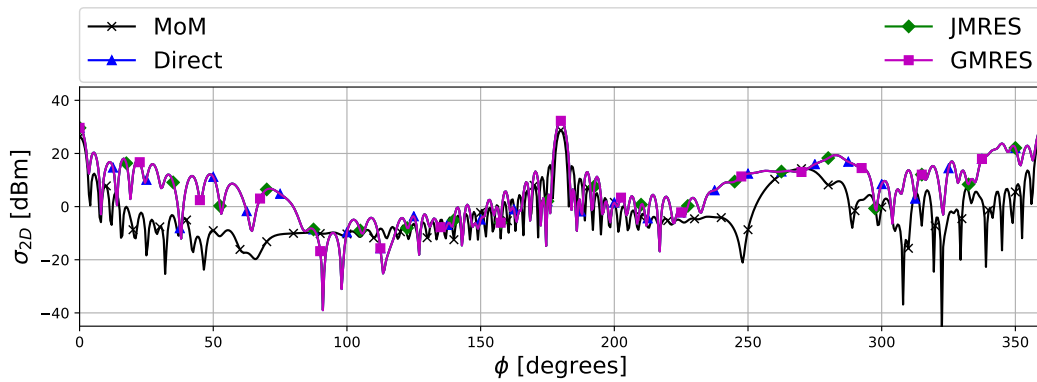
The main lobe at  $225^\circ$  has been approximated very well. MRPO has approximated the bi-static SW from the irregular octagon very well for all three of the structure sizes. It can be seen from Figure 3.8 that as the structure size increases so does the accuracy as stated in the PO approximation [14].

### 3.5.2 IPO Performance Assessment

The IPO methods from Section 3.4 will be evaluated in this section. The Gauss-Seidel, SOR and SSOR have not been added to the investigation as they either performed the same or worse than the Jacobi method and added unnecessary clutter to the graphs. The GMRES and JMRES converge to the same solution with the GMRES method taking longer to converge. Thus the GMRES has been left out of the assessment as well. The results for the methods left out have been shown for the line with angled edge in Figure 3.9.



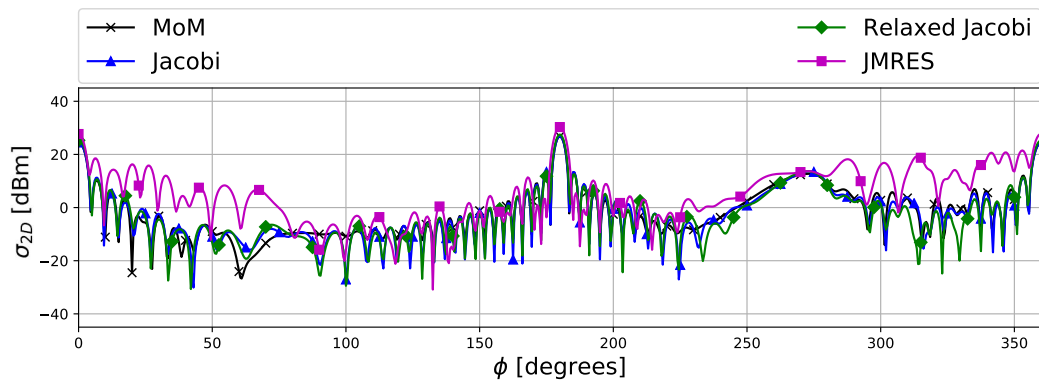
(a) Fixed point iterations.



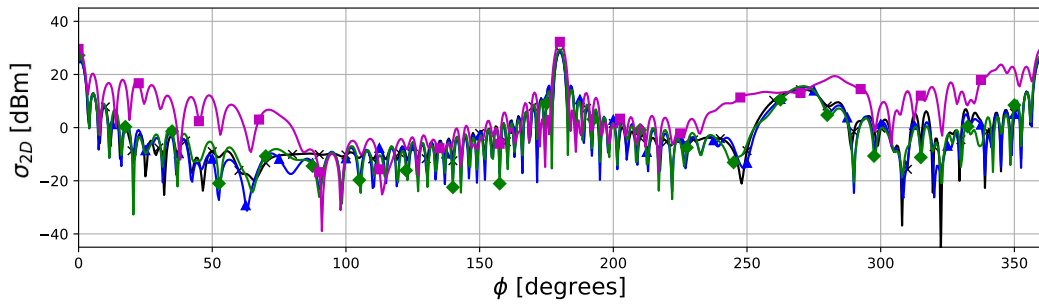
(b) Combined system methods.

Figure 3.9: IPO – Line with angled edge bi-static SW for additional methods.

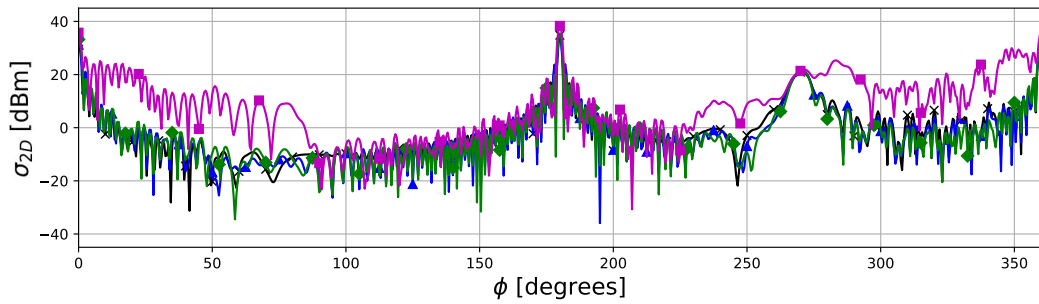
The same test cases, Figure 3.4, that were used for the MRPO evaluation will be used for the IPO evaluation. The convergence error, (3.19), will be plotted for all test cases. The  $\alpha$  value in the Relaxed Jacobi method is set to 0.7. The investigation in Section 3.5.5 shows that this is a judicious choice for the value of  $\alpha$ .



(a) Small structure.



(b) Medium structure.



(c) Large structure.

Figure 3.10: IPO – Line with angled edge bi-static SW.

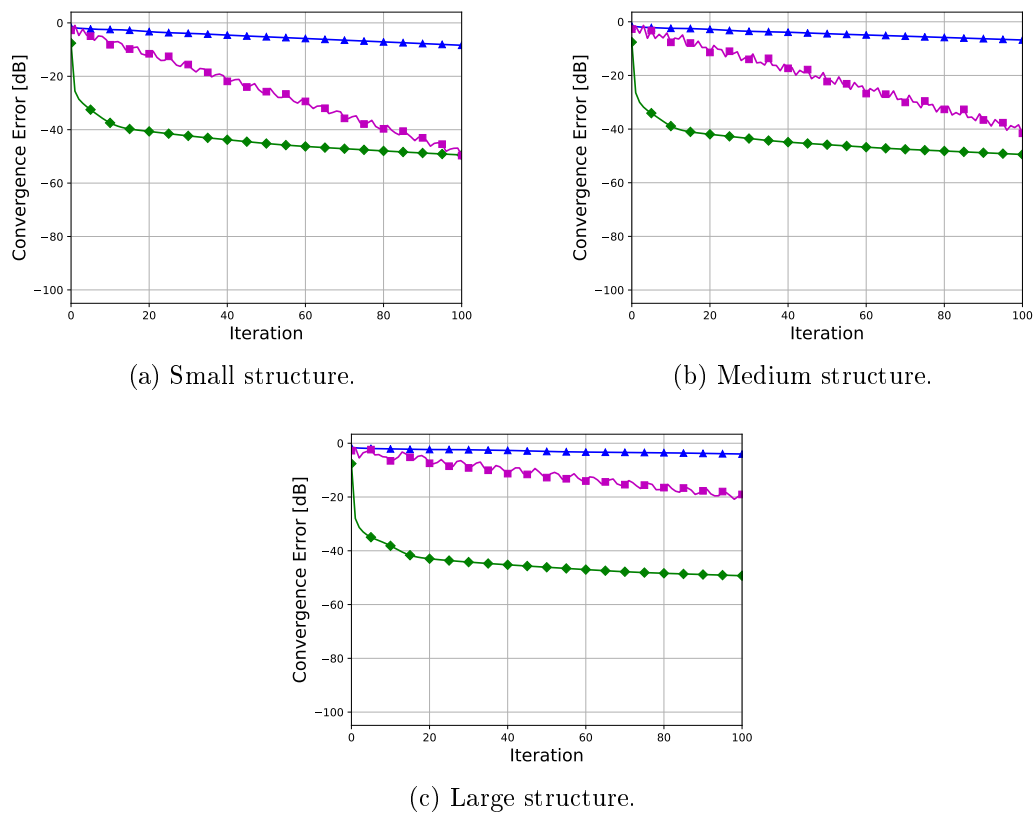
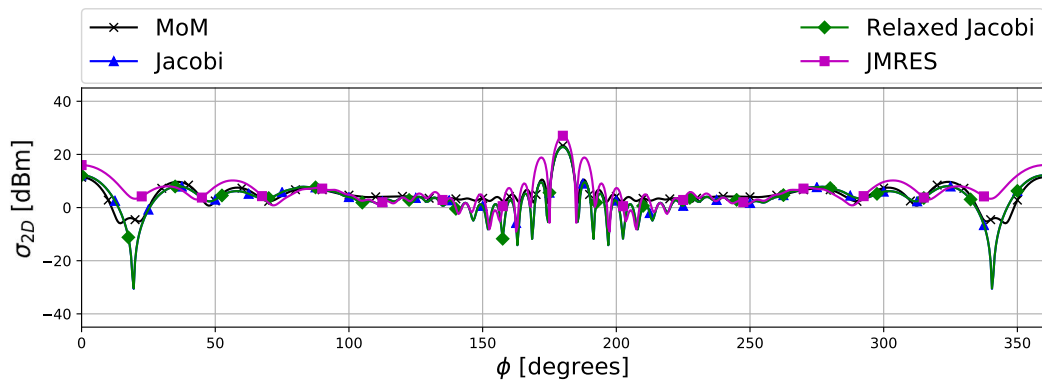
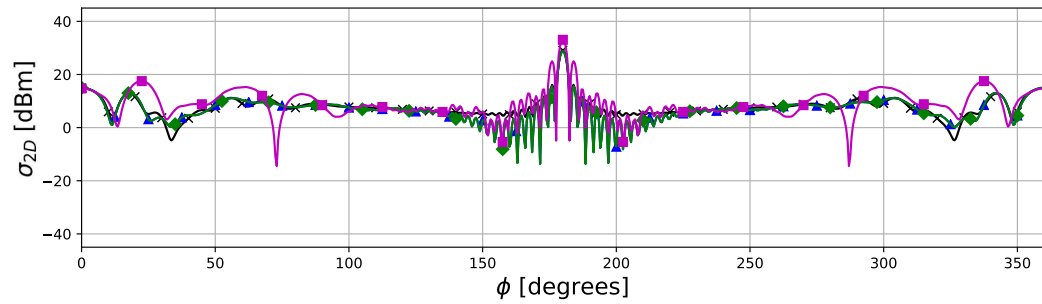


Figure 3.11: IPO – Line with angled edge convergence error history.

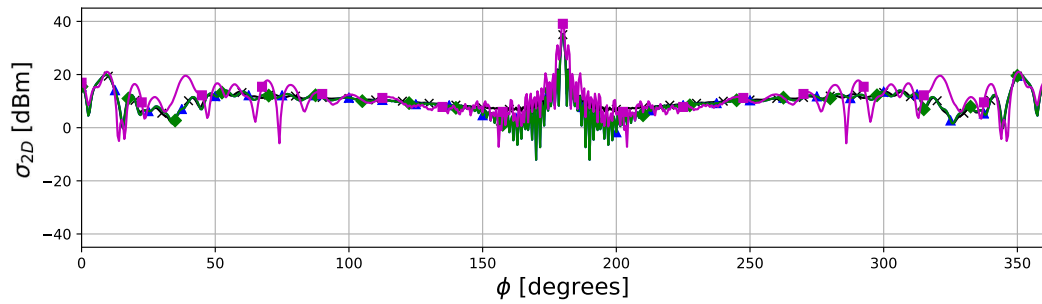
The converged Jacobi and Relaxed Jacobi solutions approximated the line with angled edge solution very well for all three structure sizes. The forward and back scattering have been approximated well by Jacobi and Relaxed Jacobi. The Relaxed Jacobi converged much faster than Jacobi. The main lobe at  $0^\circ$  and  $180^\circ$  is not as well approximated by the JMRES method. The JMRES solution started to diverge for the small and large structure and was stopped.



(a) Small structure.

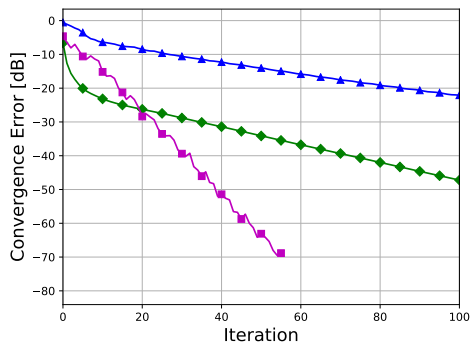


(b) Medium structure.

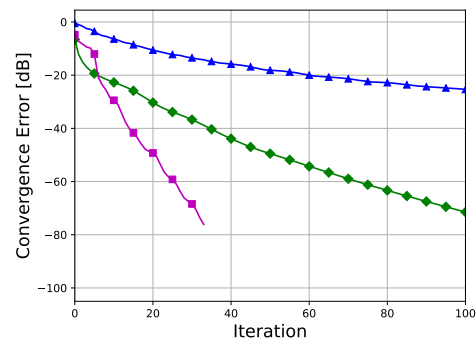


(c) Large structure.

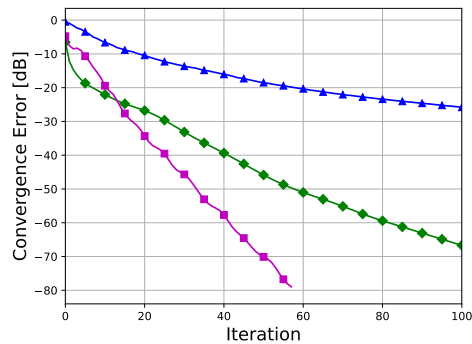
Figure 3.12: IPO – Circle with a  $40^\circ$  opening bi-static SW.



(a) Small structure.



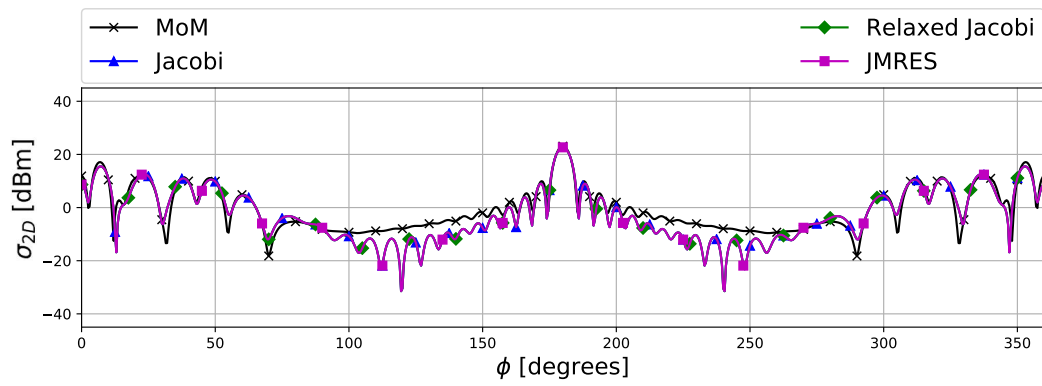
(b) Medium structure.



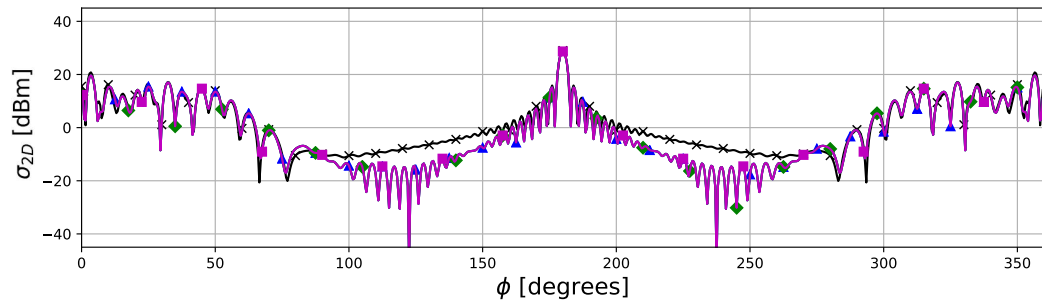
(c) Large structure.

Figure 3.13: IPO – Circle with a  $40^\circ$  opening convergence error history.

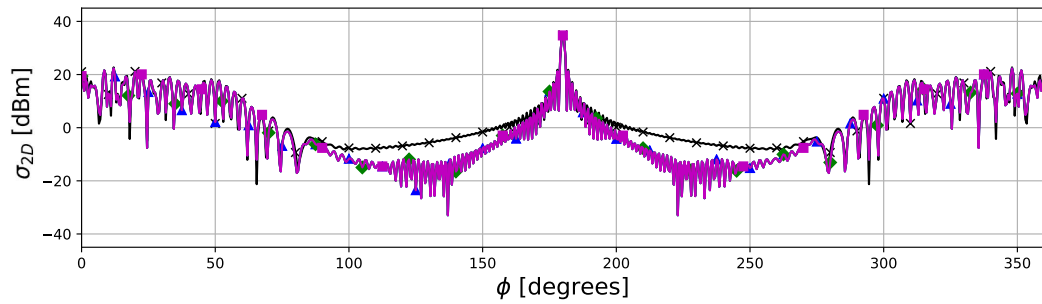
Again, the Jacobi and Relaxed Jacobi approximated the solutions very well with the JMRES not approximating the solution very well. Although JMRES has converged much quicker than Jacobi and Relaxed Jacobi, the accuracy of the final solution is not as well approximated as the other two results.



(a) Small structure.



(b) Medium structure.



(c) Large structure.

Figure 3.14: IPO – Circle with a 180° opening bi-static SW.

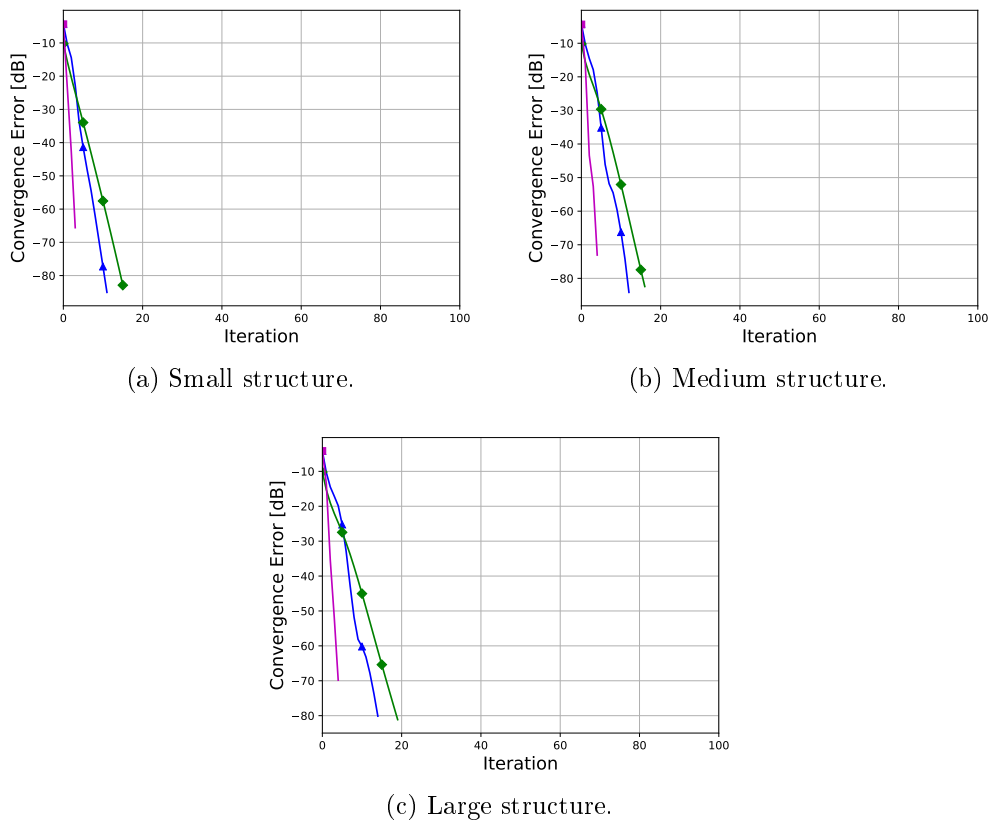
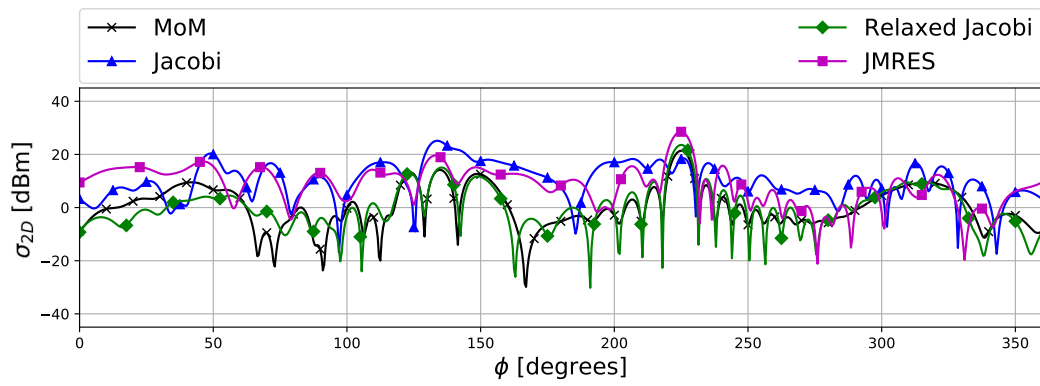


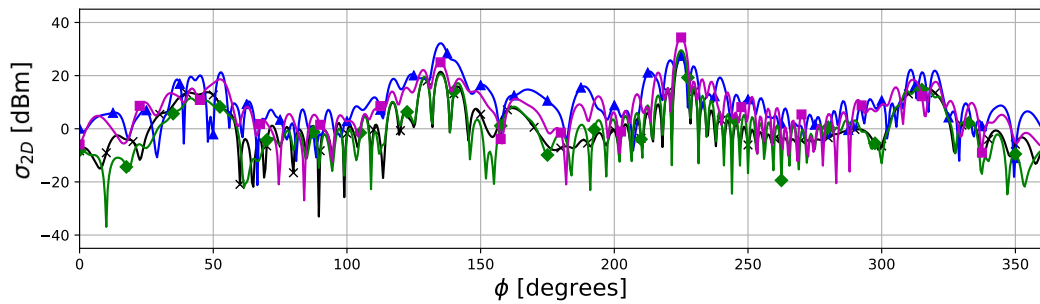
Figure 3.15: IPO – Circle with a 180° opening convergence error history.

All three of the methods give the same result for the circle with a 180° opening. The main lobes have been well approximated by the methods for this structure. The JMRES method converged faster than both the Jacobi and Relaxed Jacobi.

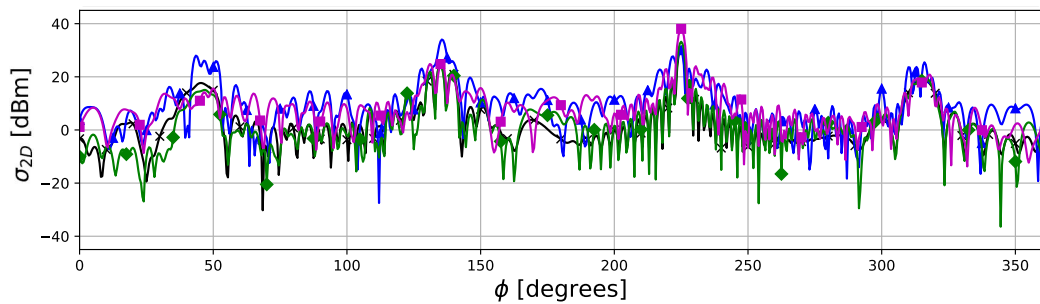




(a) Small structure.



(b) Medium structure.



(c) Large structure.

Figure 3.16: IPO – Irregular octagon bi-static SW.

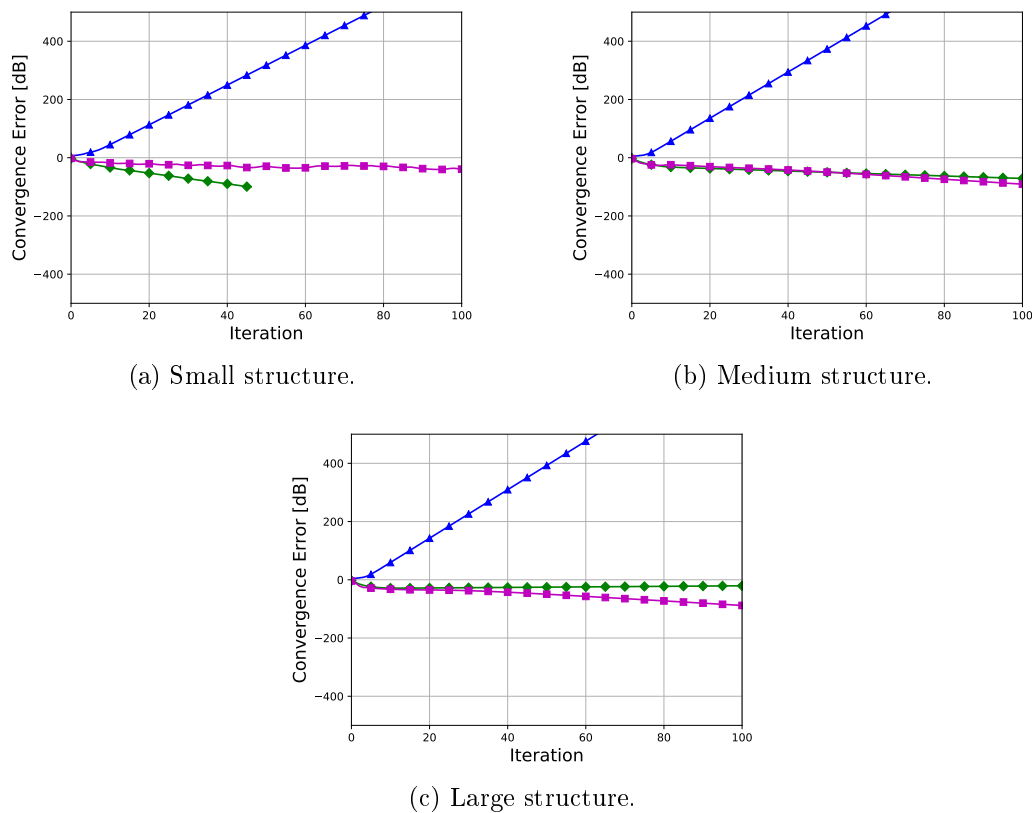


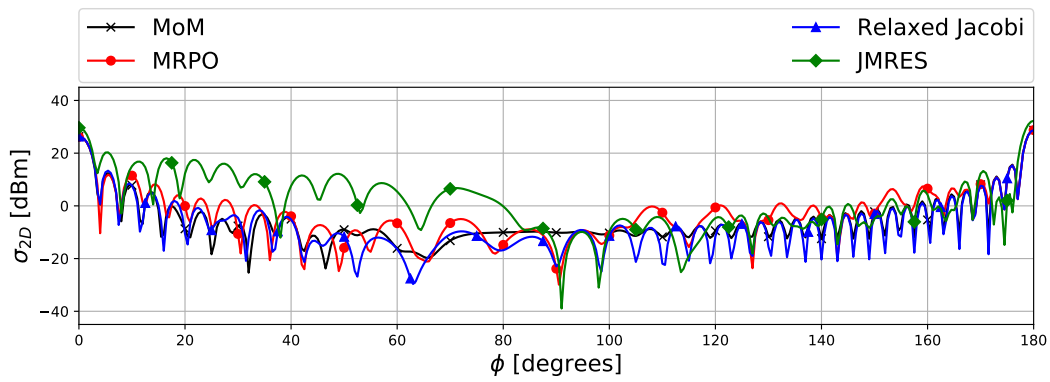
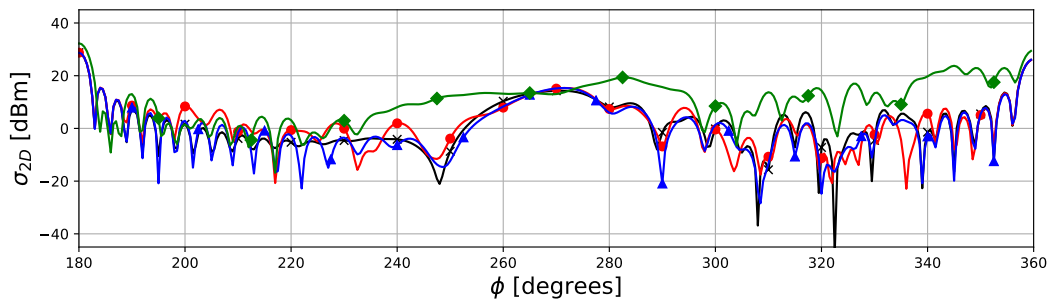
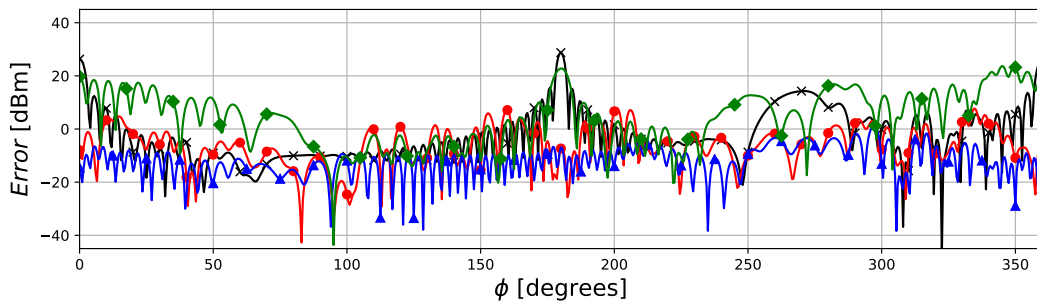
Figure 3.17: IPO – Irregular octagon convergence error history.

Figure 3.16 shows that the JMRES method has not performed well for the irregular octagon structure. The final solution for JMRES is not accurate. The Jacobi method has also not performed well for this structure. The main lobes of the scattered field have not been approximated well by JMRES and Jacobi. The Relaxed Jacobi method has performed well here. The final approximation for the main lobe is very accurate and converged in a reasonable time.

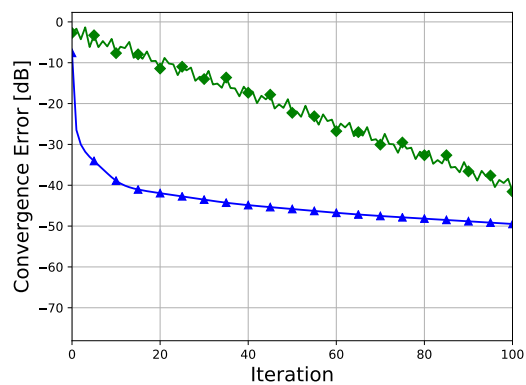
The Relaxed Jacobi method performs best in most cases but often takes much longer to converge than the Jacobi and JMRES solutions.

### 3.5.3 MRPO and IPO Comparison

This section will compare MoM, MRPO, Relaxed Jacobi and JMRES. This will give a better understanding as to how the MRPO performs against the top IPO methods. The Jacobi method has been dropped as it is always inferior to Relaxed Jacobi. Only the medium size test cases will be considered for the comparison.

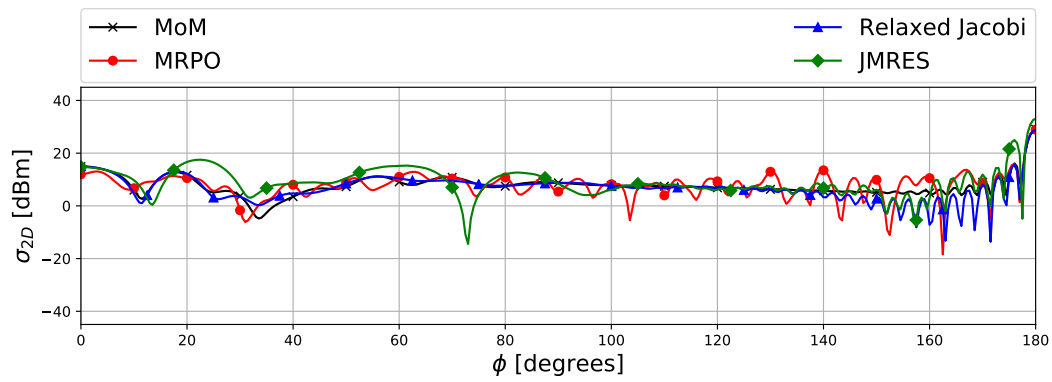
(a) Bi-static SW ( $0^\circ - 180^\circ$ ).(b) Bi-static SW ( $180^\circ - 360^\circ$ ).

(c) Bi-static SW error.

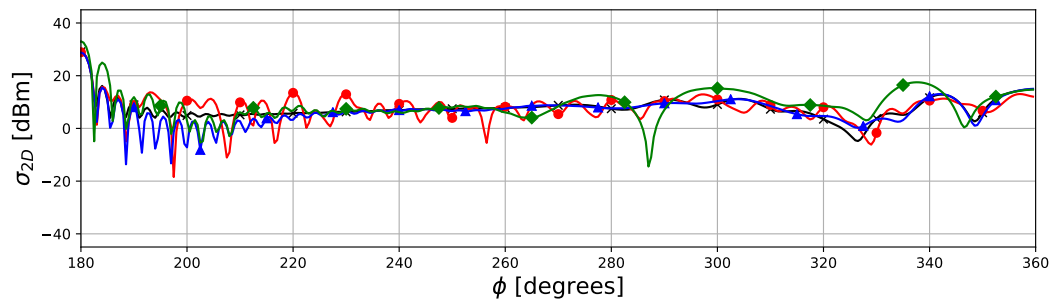


(d) Convergence error history.

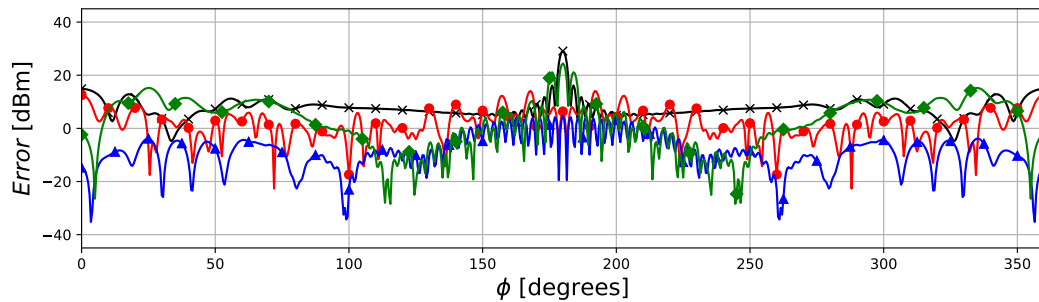
Figure 3.18: MRPO &amp; IPO – Medium sized line with angled edge.



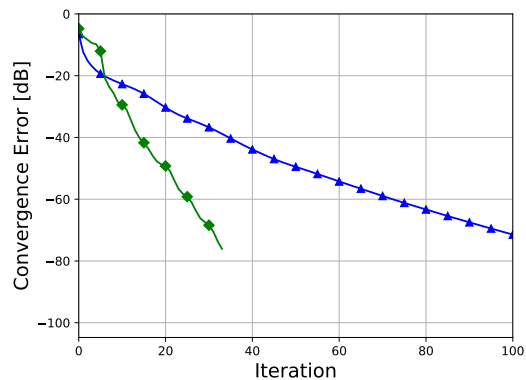
(a) Bi-static SW (0° - 180°).



(b) Bi-static SW (180° - 360°).

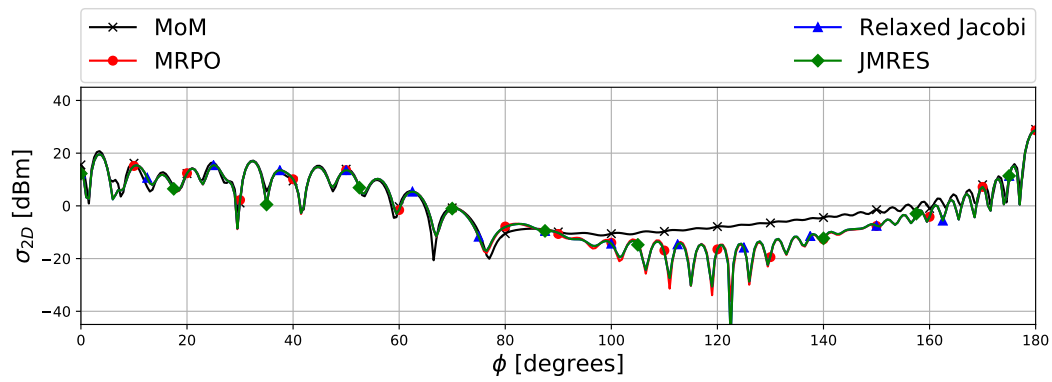
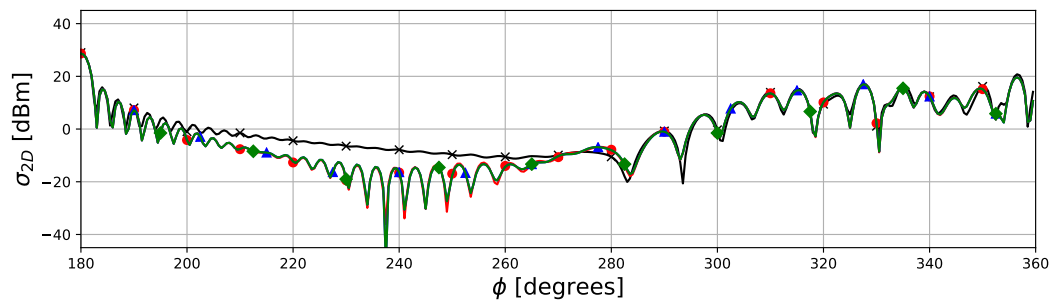
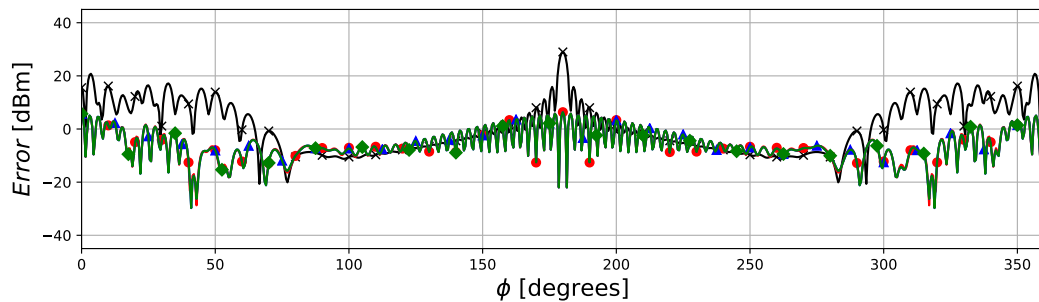


(c) Bi-static SW Error.

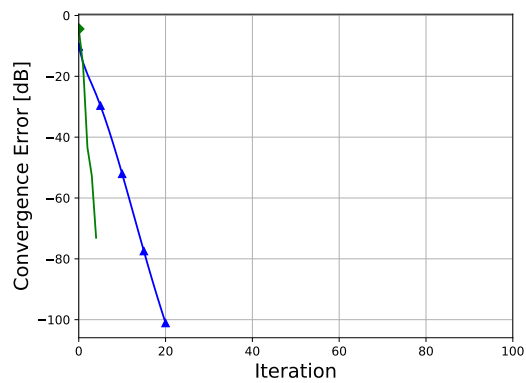


(d) Convergence error history.

Figure 3.19: MRPO &amp; IPO – Medium sized circle with a 40° opening.

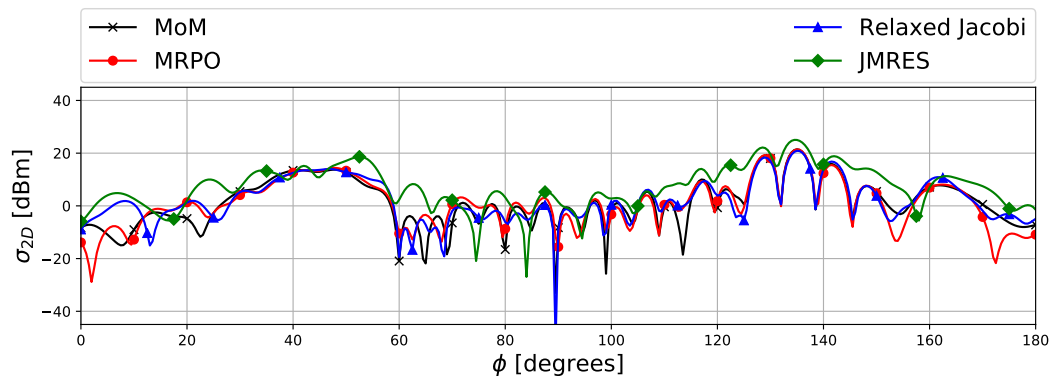
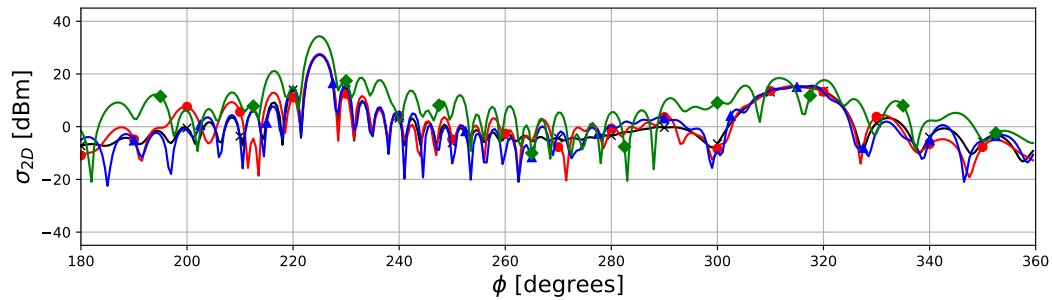
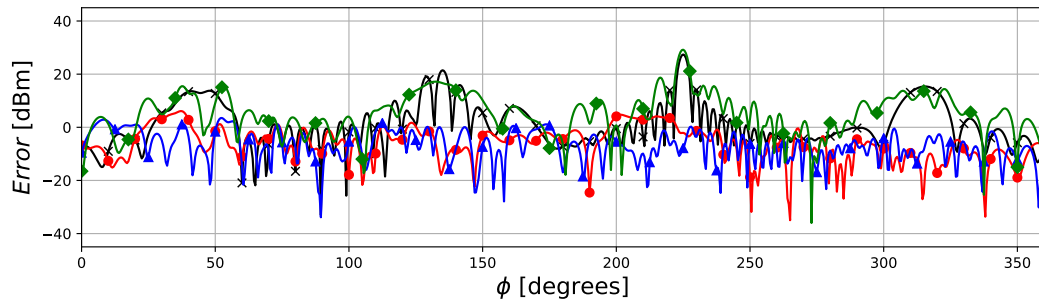
(a) Bi-static SW ( $0^\circ - 180^\circ$ ).(b) Bi-static SW ( $180^\circ - 360^\circ$ ).

(c) Bi-static SW Error.

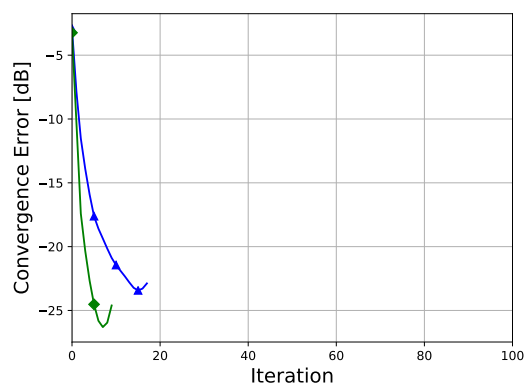


(d) Convergence error history.

Figure 3.20: MRPO & IPO – Medium sized circle with a  $180^\circ$  opening.

(a) Bi-static SW ( $0^\circ - 180^\circ$ ).(b) Bi-static SW ( $180^\circ - 360^\circ$ ).

(c) Bi-static SW Error.



(d) Convergence error history.

Figure 3.21: MRPO &amp; IPO – Medium sized irregular octagon.

The JMRES method did not approximate the main lobes at  $0^\circ$  and  $180^\circ$  well in Figure 3.18. The other two methods modelled the main lobes accurately with the Relaxed Jacobi method performing better than MRPO.

Figure 3.19 shows that the JMRES method does not perform as well as the other two methods. The Relaxed Jacobi and MRPO give very similar results for the circle with a  $40^\circ$  opening.

Figure 3.20 shows that all three methods show similar results for this structure. JMRES has converged the fastest in this case.

The JMRES method has not performed well for the irregular octagon. The MRPO and Relaxed Jacobi solutions are very similar, both approximate the MoM solution very well.

MRPO is shown to be the most consistent method for the test cases. The relaxed Jacobi method yields superior accuracy for cavities supporting many internal reflections. However, in a closed body with internal currents being modelled, it can diverge, as seen in the irregular octagon case. This issue will be investigated further in section 3.5.4. The direct method, JMRES, has converged in each of the test cases. JMRES yielded less accurate results than relaxed Jacobi and MRPO in all three of the test cases considered.

### 3.5.4 General, Closed Body Results

This section investigates the modelling of currents on the inside of a closed structure. The medium sized structures are used for this investigation. The MRPO results will not be affected by not modelling the internal currents as it uses a rigorous shadowing technique which sets the internal currents to zero. The IPO on the other hand uses a more relaxed shadowing technique which excites internal currents in a closed structure.

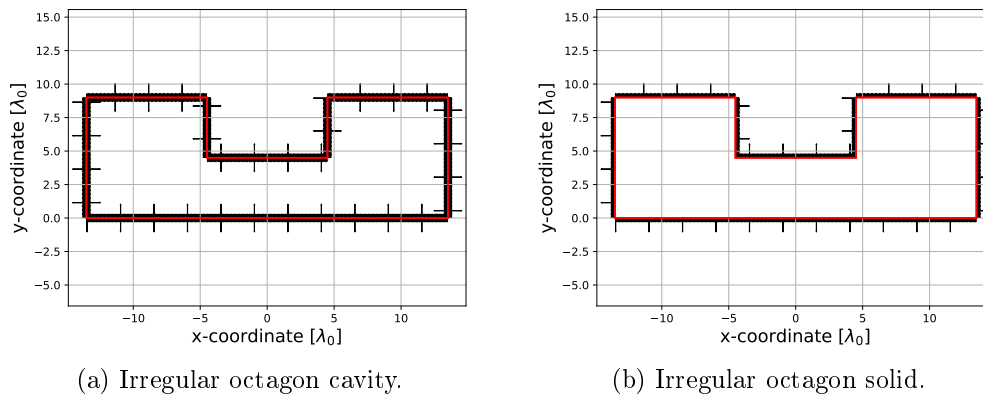
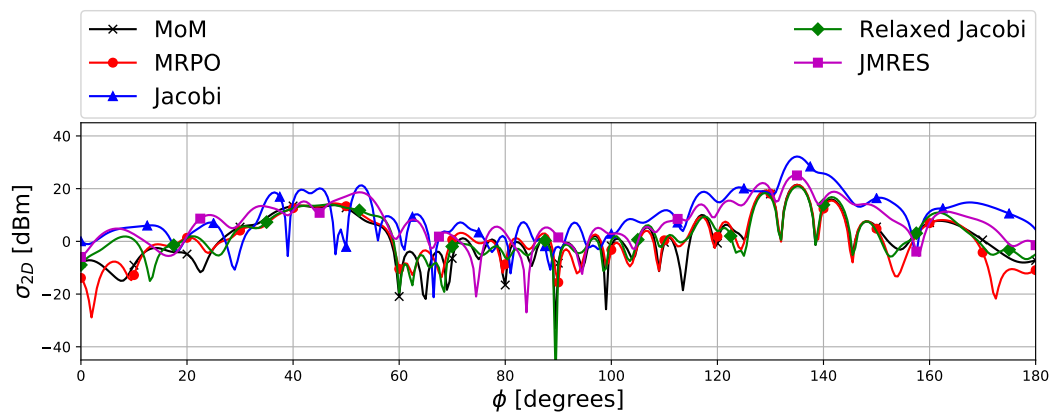
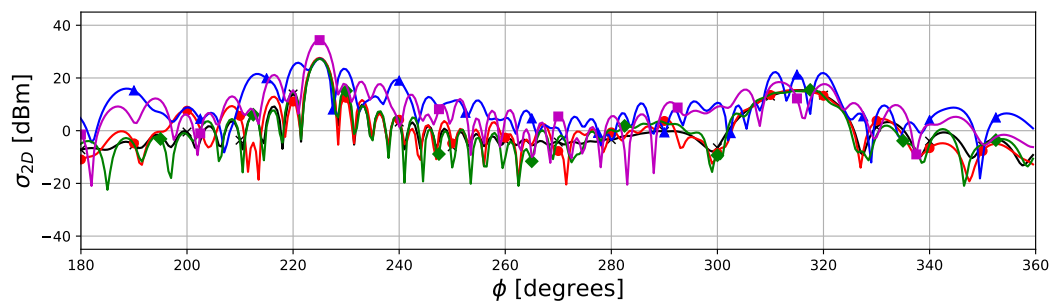
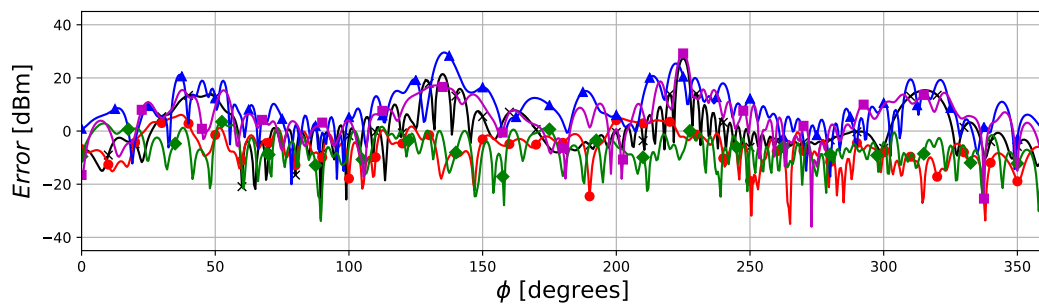


Figure 3.22: (a) Shows both sides of the structure having normals, thus modelling the external and internal current. (b) Shows only the external normals, thus only modelling the external currents.

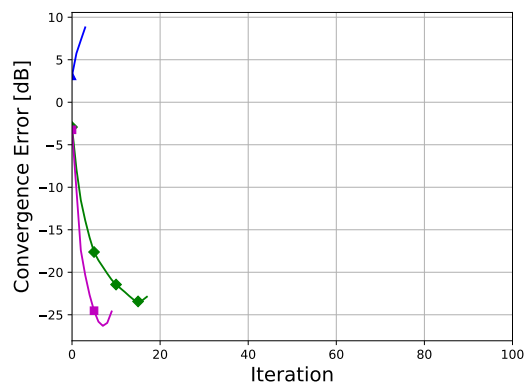
It can be seen in Figure 3.22 that the internal currents will be modelled in Figure 3.22a and not in Figure 3.22b as there are no internal normals present. Figure 3.22a is considered a cavity and Figure 3.22b is considered a solid. The bi-static SW results for the structures above are shown below.

From Figure 3.23 it can be seen that the Jacobi and JMRES do not perform well when the internal currents of the structure are modelled. The Relaxed Jacobi and MRPO perform well as shown in previous sections. When only the external currents are modelled, the Jacobi, Relaxed Jacobi and JMRES all give the same result as illustrated in Figure 3.24. The MRPO does not improve, since the shadowing for both the cavity and solid structure will be exactly the same.



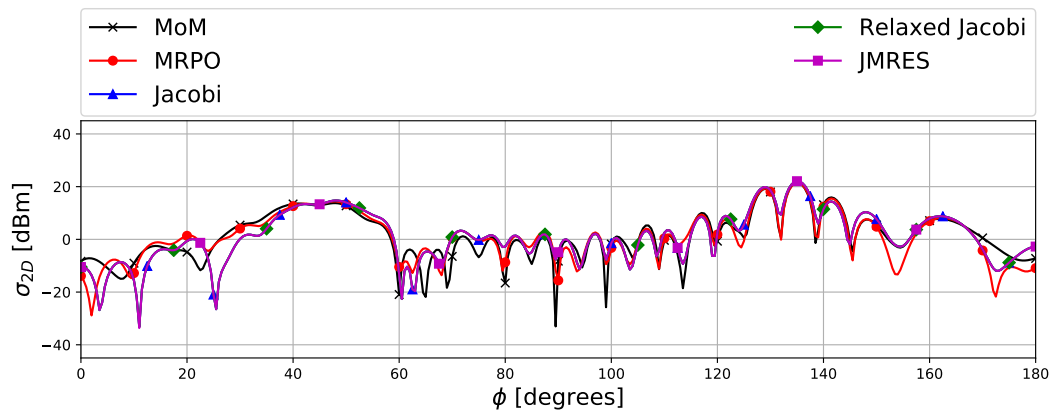
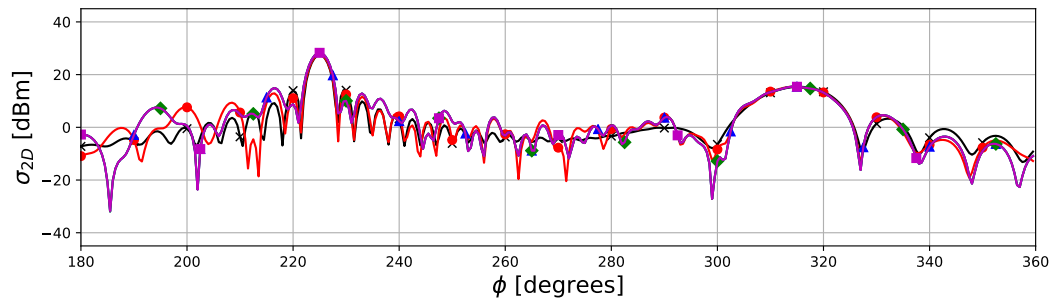
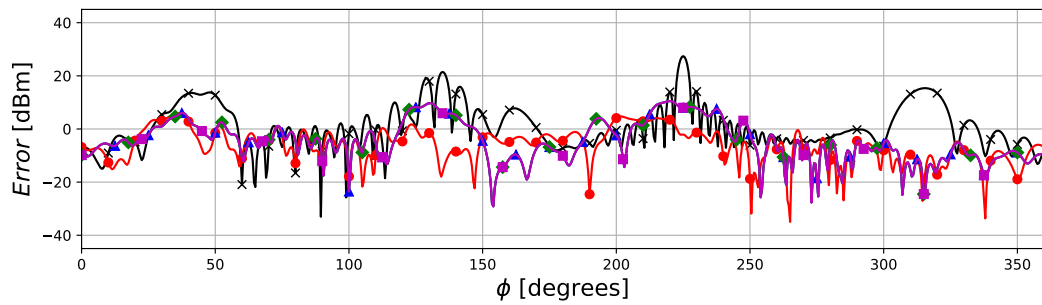
(a) Bi-static SW ( $0^\circ - 180^\circ$ ).(b) Bi-static SW ( $180^\circ - 360^\circ$ ).

(c) Bi-static SW error.

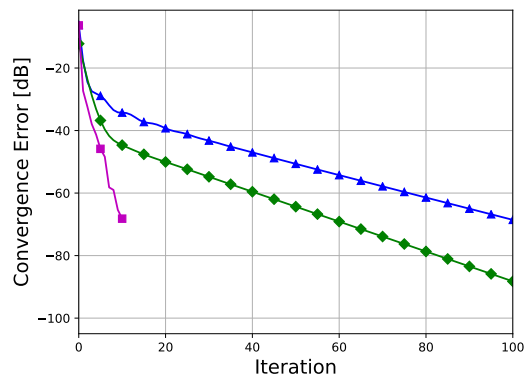


(d) Convergence error history.

Figure 3.23: Irregular octagon cavity bi-static SW (Includes internal currents).

(a) Bi-static SW ( $0^\circ - 180^\circ$ ).(b) Bi-static SW ( $180^\circ - 360^\circ$ ).

(c) Bi-static SW error.



(d) Convergence error history.

Figure 3.24: Irregular octagon solid bi-static SW (Excludes internal currents).

### 3.5.5 Relaxed Jacobi $\alpha$ Parameter Assessment

The  $\alpha$  parameter in the Relaxed Jacobi iteration, (3.50), is investigated. Only the large versions of the test cases from Figure 3.4 have been used. The  $\alpha$  parameter has been set at 0.5 and incremented by 0.1 up to 0.9.

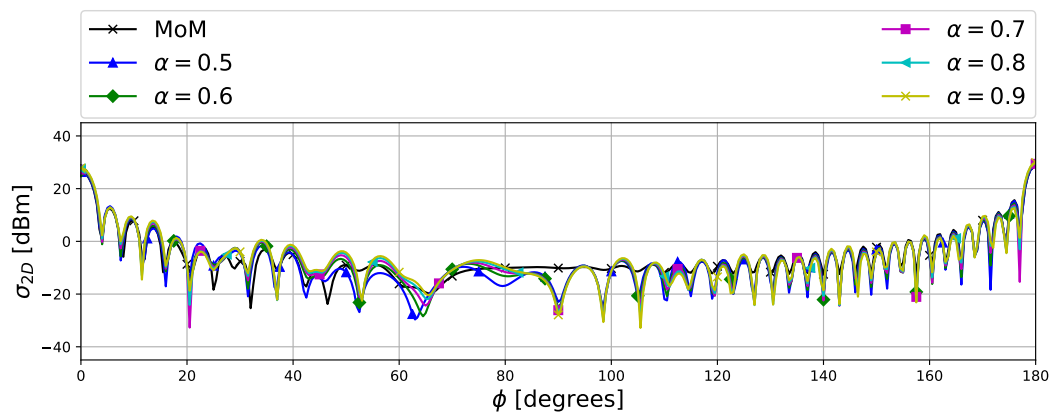
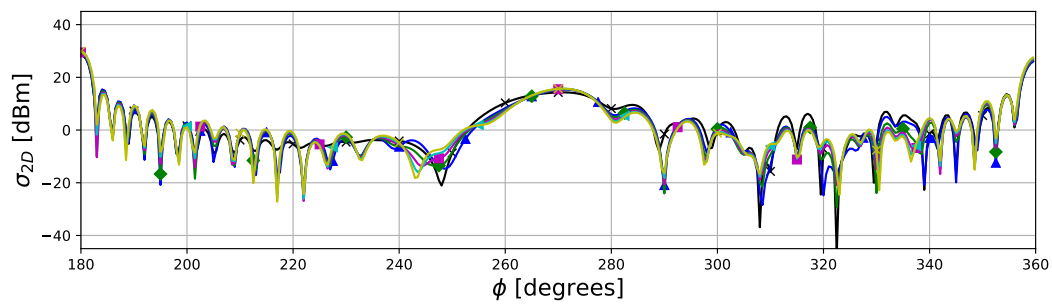
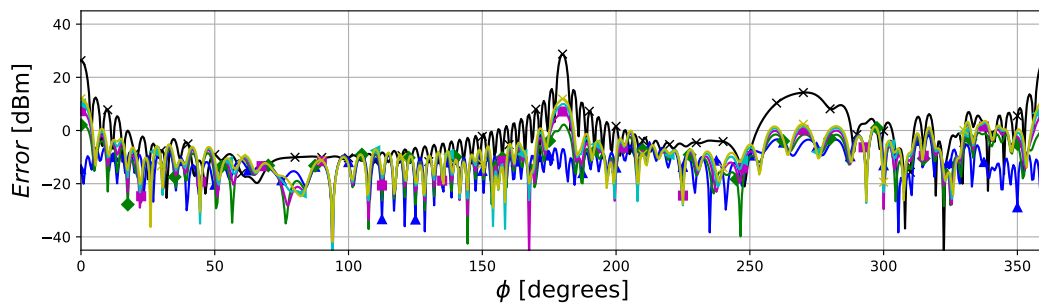
In Figure 3.25 there is no variation between the results on the main lobes at  $0^\circ$  and  $180^\circ$ . Most of the variation is between the two main lobes. When  $\alpha$  is set to 0.9 the nulls are less dominant but when it is set to 0.7 it is closer to the nulls of the MoM solution. For the line with angled edge, the higher the  $\alpha$  value the faster the convergence.

All of the results approximate the forward scattering exactly in Figure 3.26. When  $\alpha$  is set to 0.6 it approximates the back scattering very well compared to the other values. Again, when the  $\alpha$  value is set to 0.9 it converges the fastest with 0.5 taking the longest to converge.

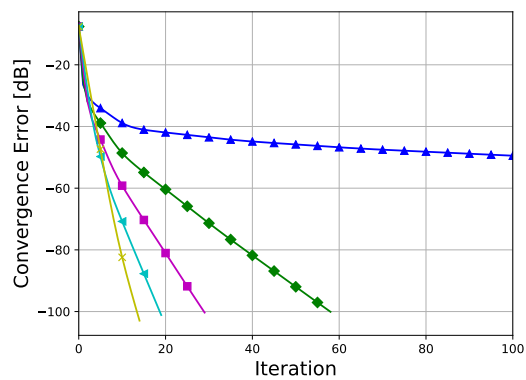
Figure 3.27 shows the forward and back scattering approximated exactly by all the  $\alpha$  values. There is a large difference between  $80^\circ$  and  $160^\circ$  and between  $200^\circ$  and  $280^\circ$  too. When  $\alpha$  is set to 0.6 for the circle with a  $180^\circ$  opening, the MoM result is closely approximated throughout. For this test structure, all of the results converged relatively quickly.

It can be seen in Figure 3.28 that when the  $\alpha$  value is set to 0.6 it approximates the MoM solution very well overall. Setting  $\alpha$  to any value larger than 0.7 causes the solution to diverge.

The  $\alpha$  parameter is very structure dependent. From the given results, 0.7 has been chosen as the recommended value for  $\alpha$ . This value has been used throughout the thesis for the Relaxed Jacobi method.

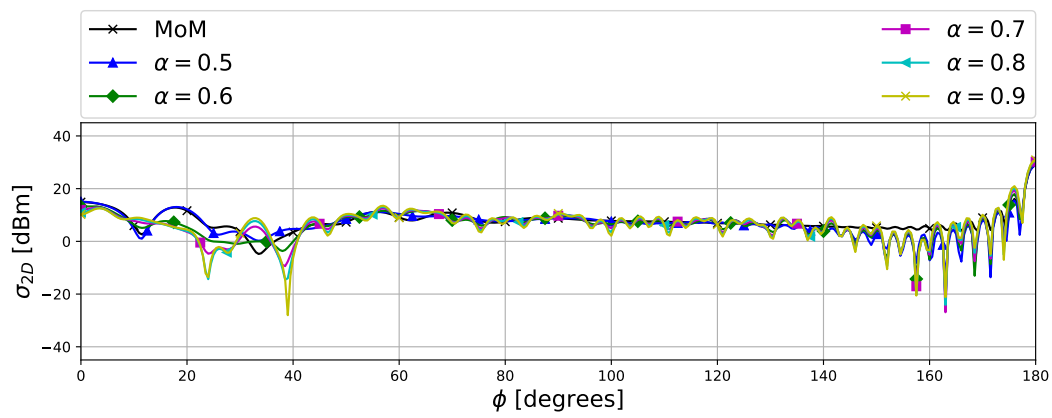
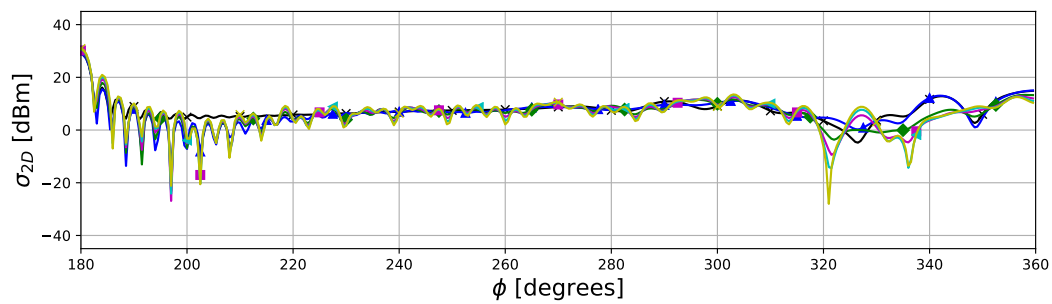
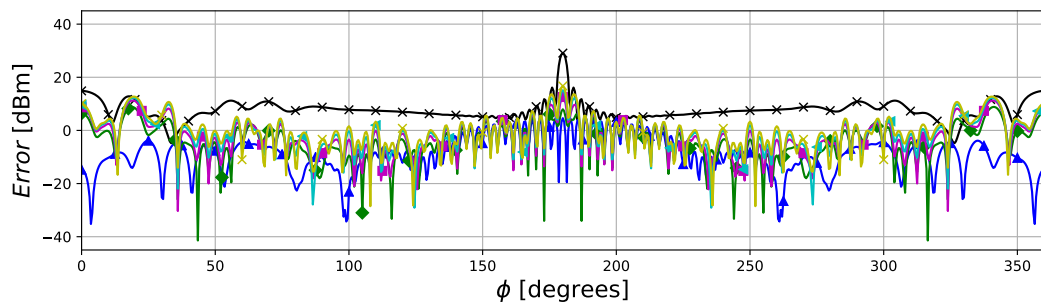
(a) Bi-static SW ( $0^\circ - 180^\circ$ ).(b) Bi-static SW ( $180^\circ - 360^\circ$ ).

(c) Bi-static SW error.

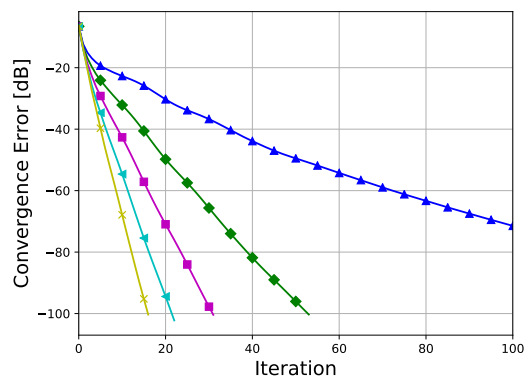


(d) Convergence error history.

Figure 3.25: Line with angled edge.

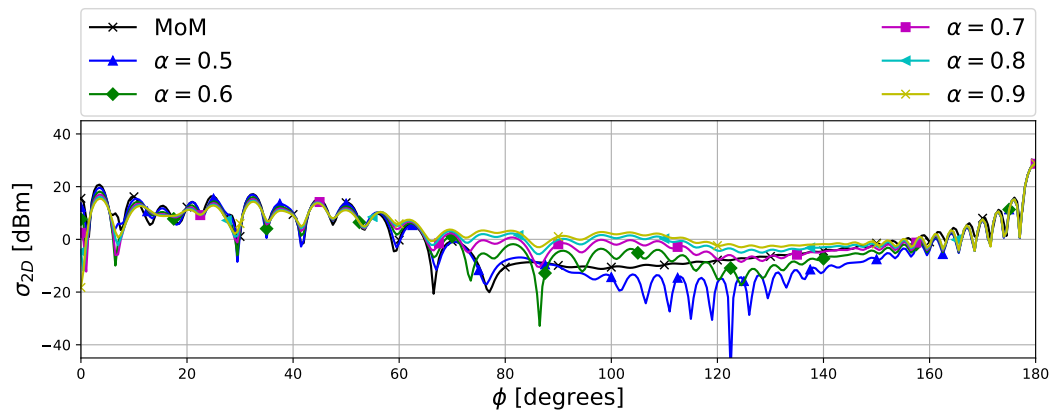
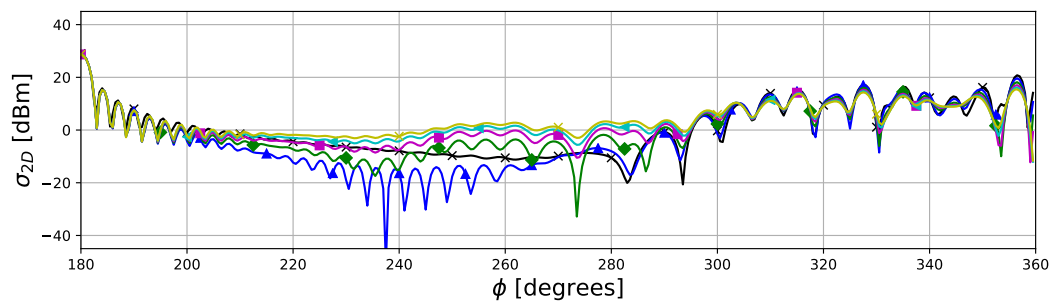
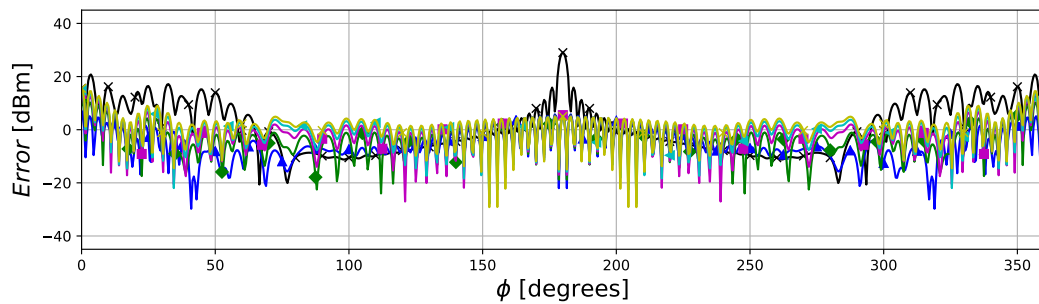
(a) Bi-static SW ( $0^\circ - 180^\circ$ ).(b) Bi-static SW ( $180^\circ - 360^\circ$ ).

(c) Bi-static SW error.

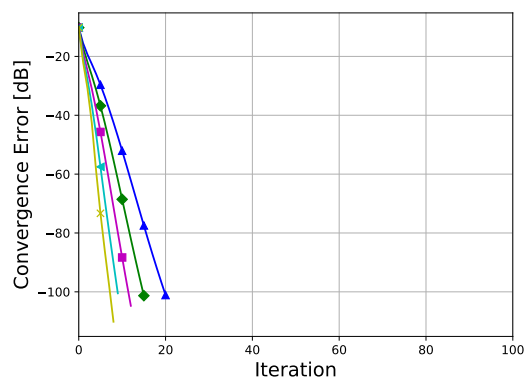


(d) Convergence error history.

Figure 3.26: Circle with a  $40^\circ$  opening.

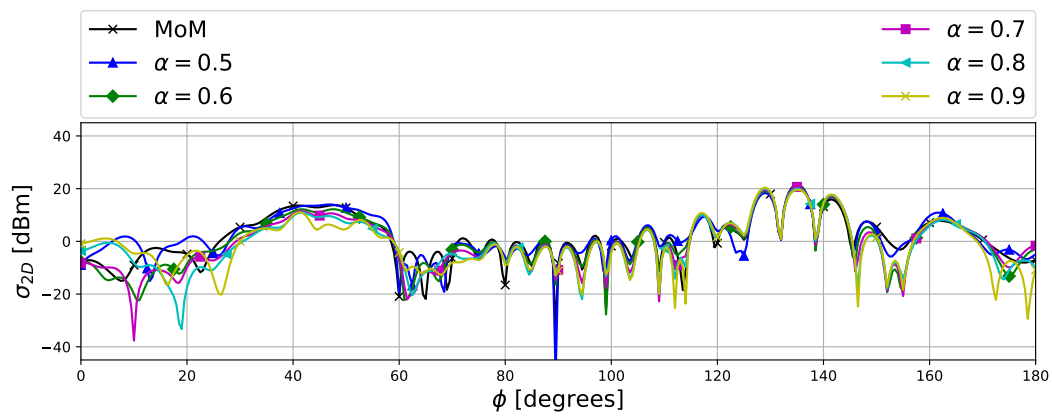
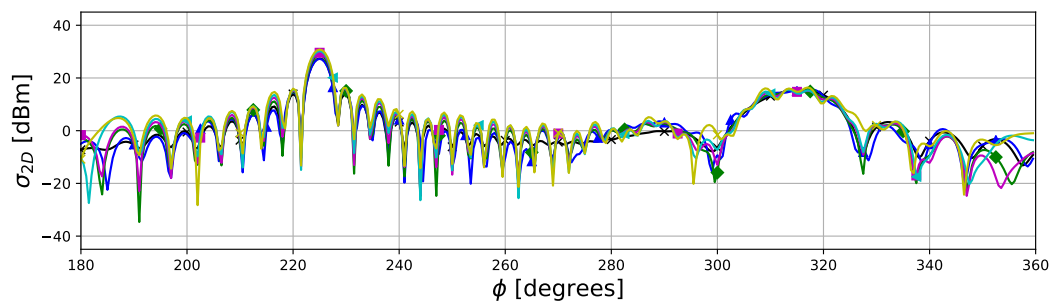
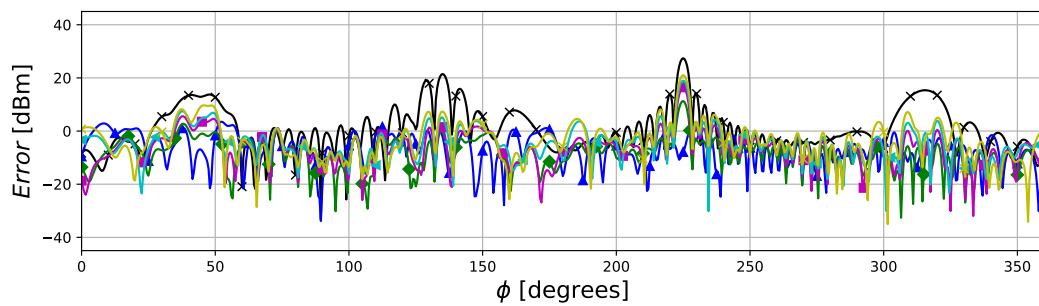
(a) Bi-static SW ( $0^\circ - 180^\circ$ ).(b) Bi-static SW ( $180^\circ - 360^\circ$ ).

(c) Bi-static SW error.

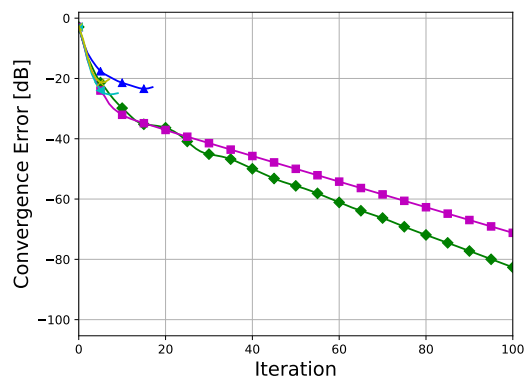


(d) Convergence error history.

Figure 3.27: Circle with a  $180^\circ$  opening

(a) Bi-static SW ( $0^\circ - 180^\circ$ ).(b) Bi-static SW ( $180^\circ - 360^\circ$ ).

(c) Bi-static SW error.



(d) Convergence error history.

Figure 3.28: Irregular octagon.

## 3.6 Conclusion

The MRPO method performs very well on all of the test structures. It models the true shadowing of the structure and thus requires some intuition when selecting the number of reflections to model. Too little reflections and the results will be incomplete, too many reflections and the simulation will take unnecessarily long. A disadvantage to the MRPO method is that the shadowing matrix needs to be calculated, although there is an MLFMM solution to dramatically decrease the computation time [18].

The IPO methods perform well. Most of the methods are less accurate than MRPO. Relaxed Jacobi is the most accurate IPO iteration on the test structures. The IPO has an advantage over the MRPO method in that the shadowing matrix can be calculated much faster but accuracy is sacrificed.

For closed body structures it is beneficial to exclude the internal currents for IPO as modelling the internal currents will cause the solution to take longer to converge, resulting in a less accurate solution. The Relaxed Jacobi method remains accurate with or without modelling internal currents.

The  $\alpha$  parameter is very structure dependent. For the implementation of the IPO methods in the previous sections,  $\alpha$  was set to 0.7 throughout.



## Chapter 4

# Domain Decomposition PO

### 4.1 Introduction

This chapter presents the Domain Decomposition Physical Optics (DDPO) method. A surface of equivalent sources is used to decouple two regions. Reflections between the two regions communicate via these sources such that the full MRPO is approximated. This will reduce the complexity and computation time significantly.

The first section gives a detailed formulation of DDPO. The second section will provide validation results to verify that the formulation is working correctly. The third section will provide results on a simple test case for the DDPO method.

### 4.2 Formulation

Consider the problem of modelling the bi-static RCS of the airplane in Figure 4.1, where it can be seen that solving this problem using a PO technique would be relatively simple for most parts of the model. The engine inlet however, in Figure 4.2, is extremely complicated and is where the bottleneck will occur.



Figure 4.1: Boeing 747-400 CAD model [23].



Figure 4.2: Jet engine inlet CAD model [24].

One way to solve a problem such as this is to model the engine inlet separately and replace it on the airplane with equivalent sources. This method works well but does not take into account any reflections from the airplane into the inlet or vice versa, since the two geometries are effectively solved separately. The airplane and inlet are decoupled.

DDPO uses a very similar technique, however, full coupling is taken into account between the two regions. An aperture of equivalent sources is placed in front of the inlet, dividing the problem into two regions. This is how the airplane and inlet geometries will communicate with each other, via the equivalent sources. This means that the shadowing coefficients can be calculated

separately for each structure, saving computation time, while still taking coupling into account.

The general MFIE formulated in Chapter 2 is used in the DDPO formulation. The aperture will contain both electric and magnetic currents. Thus, using equation (2.18), the magnetic field radiated from the aperture can be calculated. Once the radiated magnetic field is known, the PO approximation can be used to determine the surface currents of a structure.

The DDPO performs MRPO inside the cavity and on the external geometry. Using the aperture to interact between the two geometries is the only difference between the two methods.

Figure 4.3 shows the process of calculating the currents in the cavity and on the external geometry due to multiple reflections with full interactions, but in a decomposed manner.

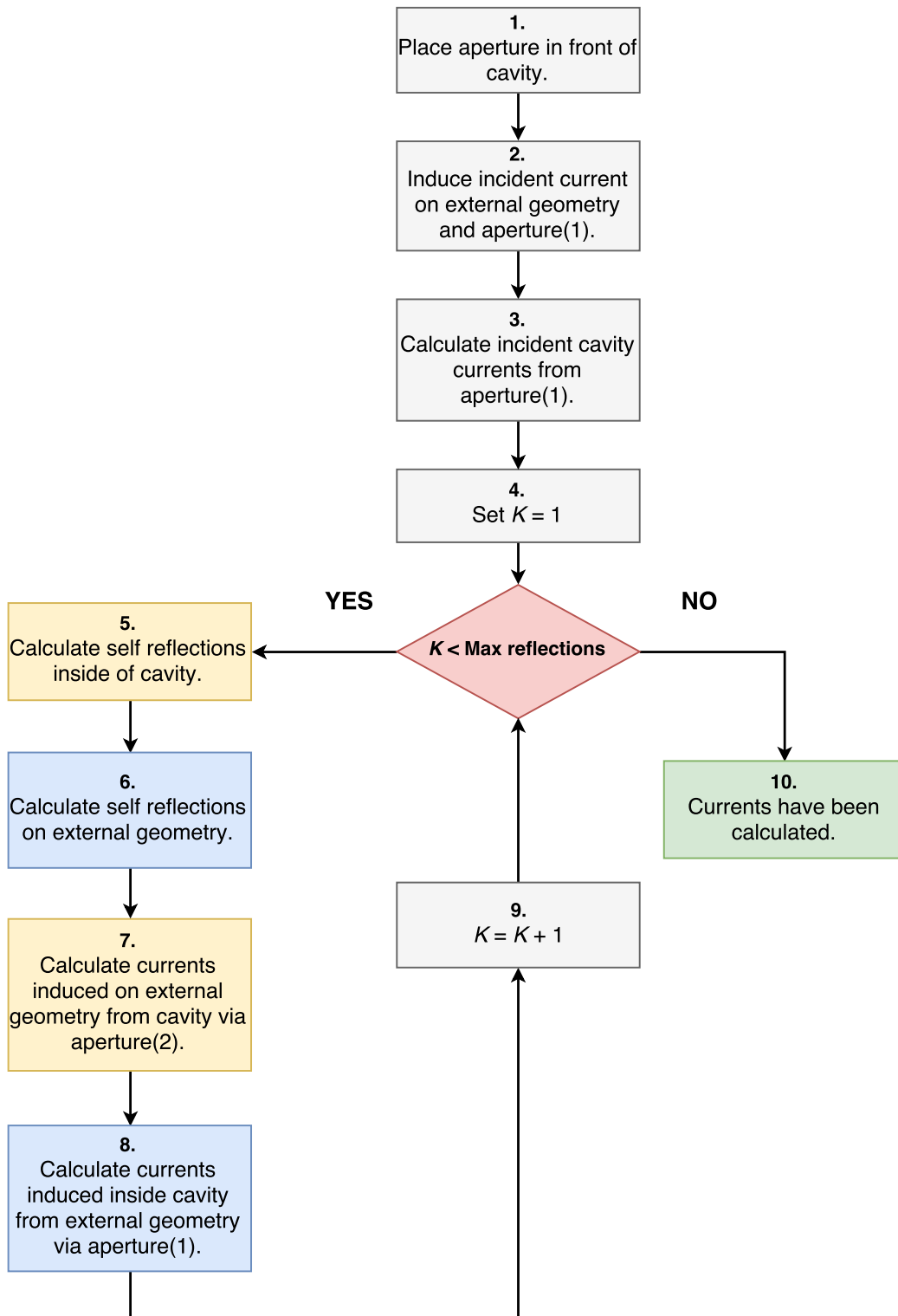


Figure 4.3: DDPO current calculation flow chart.

The figures below will help to explain the DDPO method graphically with references to the flow chart. For the rest of the formulation the current induced on the external geometry surface,  $\Gamma_{\text{ext}}$ , will be referred to as  $\mathbf{J}^{\text{ext}}$ . The current induced on the internal surface of the cavity,  $\Gamma_{\text{cav}}$ , will be referred to as  $\mathbf{J}^{\text{cav}}$ . The electric and magnetic currents on the outside surface of the aperture,  $\Gamma_1$ , will be referred to as  $\mathbf{J}^{\text{apt}(1)}$  and  $\mathbf{M}^{\text{apt}(1)}$  and the currents on the inside surface of the aperture,  $\Gamma_2$ , will be referred to as  $\mathbf{J}^{\text{apt}(2)}$  and  $\mathbf{M}^{\text{apt}(2)}$ . For the purpose of simplification, the external currents of the cavity will not be considered for the formulation, though such currents are included as part of the external solution for all the results, following standard MRPO theory. The aperture is represented by the green dotted line.

DDPO uses the same rigorous shadowing as MRPO. The shadowing coefficients  $\delta^{\text{ext}}$  and  $\delta^{\text{cav}}$  will be used. The shadowing coefficient  $\delta^{\text{cav}}$  is the inter-segment visibility of the surface  $\Gamma_{\text{cav}} \cup \Gamma_2$  while  $\delta^{\text{ext}}$  is the inter-segment visibility of the surface  $\Gamma_{\text{ext}} \cup \Gamma_1$ .

Figure 4.4 shows the structure with no currents induced on the surface. The incident field is not yet applied. Thus all of the electric and magnetic currents will be equal to zero. An aperture has been placed in front of the cavity, this is step 1 from the flow chart.

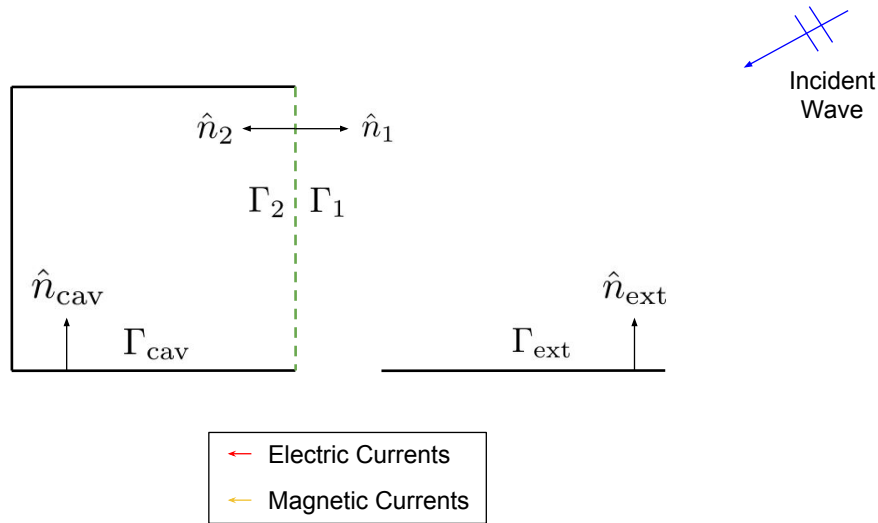


Figure 4.4: DDPO Initial currents.

Figure 4.5 shows the incident currents induced on the surface of the aperture and external geometry, this is step 2 of the flow chart. The shadowing coefficient,  $\delta^{\text{inc}}$ , has been defined in (3.3), as for the structure with the cavity closed up. Note that the aperture has both electric and magnetic currents, while the external geometry only has electric currents. The currents can be described as follows:

$$\mathbf{J}_{(1)}^{\text{ext}}(\boldsymbol{\rho}') = 2\delta^{\text{inc}} \hat{\mathbf{n}}_{\text{ext}} \times \mathbf{H}^{\text{inc}}(\boldsymbol{\rho}') \quad (4.1)$$

$$\mathbf{J}_{(1)}^{\text{apt}(1)}(\boldsymbol{\rho}') = \delta^{\text{inc}} \hat{\mathbf{n}}_2 \times \mathbf{H}^{\text{inc}}(\boldsymbol{\rho}') \quad (4.2)$$

$$\mathbf{M}_{(1)}^{\text{apt}(1)}(\boldsymbol{\rho}') = \delta^{\text{inc}} E_z^{\text{inc}}(\boldsymbol{\rho}') \hat{\mathbf{z}} \times \hat{\mathbf{n}}_2 \quad (4.3)$$

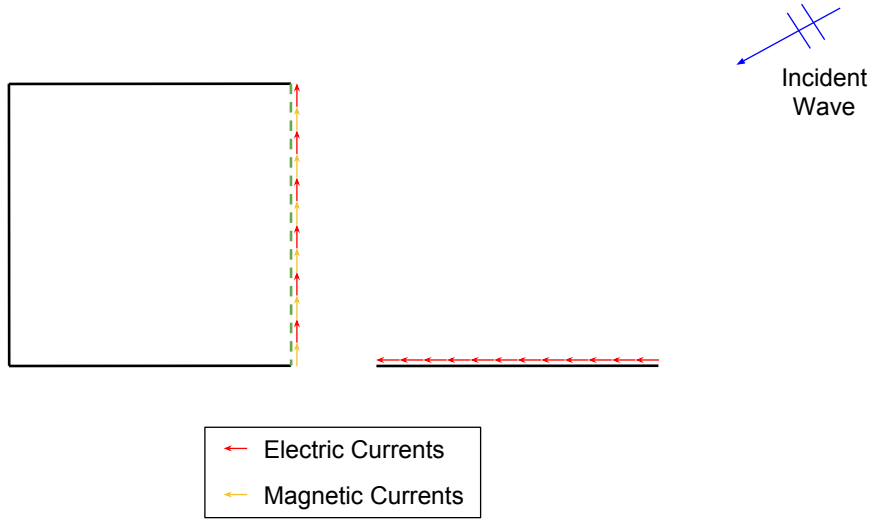


Figure 4.5: DDPO Incident currents.

Next, the MFIE, (2.18), from Chapter 2 is used in step 3 of the flow chart to calculate the magnetic field radiated from the aperture into the cavity. The PO approximation is then used to calculate the induced electric currents. At this stage it is the decomposed version of the MRPO solution, with  $K = 1$ . The induced incident currents have been calculated on both the external geometry and the cavity.

$$\mathbf{J}_{(1)}^{\text{cav}}(\boldsymbol{\rho}') = 2 \int_{\Gamma_1} \hat{\mathbf{n}}_{\text{cav}} \times \mathbf{H}(\delta^{\text{cav}}(\mathbf{J}_{(1)}^{\text{apt}(1)}, \mathbf{M}_{(1)}^{\text{apt}(1)}))(\boldsymbol{\rho}) d\Gamma'_1 \quad (4.4)$$

where,

$$\begin{aligned} \mathbf{H}(\mathbf{J}, \mathbf{M})(\boldsymbol{\rho}) = \int_{\Gamma_0} \left[ [\hat{\mathbf{n}} \times \mathbf{M}(\boldsymbol{\rho}')] [\hat{\mathbf{n}}' \cdot \nabla' \nabla' G_0(\boldsymbol{\rho}, \boldsymbol{\rho}') \times \hat{\mathbf{z}}] \right. \\ \left. + \nabla G_0(\boldsymbol{\rho}, \boldsymbol{\rho}') \times \mathbf{J}(\boldsymbol{\rho}') \right] d\Gamma' \end{aligned} \quad (4.5)$$

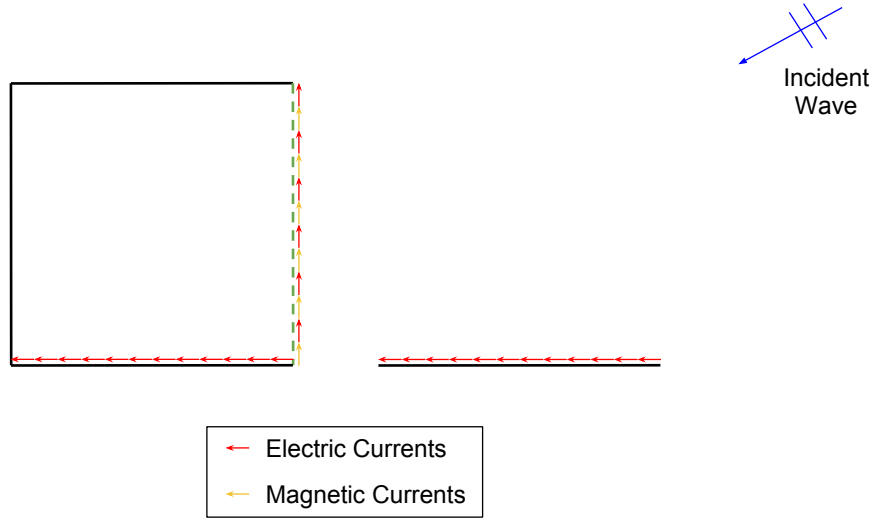


Figure 4.6: DDPO First reflection currents.

Step 5 involves calculating the self reflections inside the cavity. This is known as a half step, as reflections from the external geometry have not been taken into account.

$$\mathbf{J}_{(K+\frac{1}{2})}^{\text{cav}}(\boldsymbol{\rho}') = 2 \int_{\Gamma_{\text{cav}}} \hat{\mathbf{n}}_{\text{cav}} \times \mathbf{H}(\delta^{\text{cav}} \mathbf{J}_{(K)}^{\text{cav}})(\boldsymbol{\rho}) d\Gamma'_{\text{cav}} \quad (4.6)$$

The self reflections of the external geometry are calculated in step 6, as follows:

$$\mathbf{J}_{(K+\frac{1}{2})}^{\text{ext}}(\boldsymbol{\rho}') = 2 \int_{\Gamma_{\text{ext}}} \hat{\mathbf{n}}_{\text{ext}} \times \mathbf{H}(\delta^{\text{ext}} \mathbf{J}_{(K)}^{\text{ext}})(\boldsymbol{\rho}) d\Gamma'_{\text{ext}} \quad (4.7)$$

The electric currents in the cavity radiate and are used to set up currents,  $\mathbf{J}^{\text{apt}(2)}$  and  $\mathbf{M}^{\text{apt}(2)}$ , on the inside aperture.

$$\mathbf{J}_{(K+1)}^{\text{apt}(2)}(\boldsymbol{\rho}') = \int_{\Gamma_{\text{cav}}} \hat{\mathbf{n}}_1 \times \mathbf{H}(\delta^{\text{cav}} \mathbf{J}_{(K)}^{\text{cav}})(\boldsymbol{\rho}) d\Gamma'_{\text{cav}} \quad (4.8)$$

$$\mathbf{M}_{(K+1)}^{\text{apt}(2)}(\boldsymbol{\rho}') = \int_{\Gamma_{\text{cav}}} \mathbf{E}(\delta^{\text{cav}} \mathbf{J}_{(K)}^{\text{cav}})(\boldsymbol{\rho}) \times \hat{\mathbf{n}}_1 d\Gamma'_{\text{cav}} \quad (4.9)$$

where,

$$\mathbf{H}(\mathbf{J})(\boldsymbol{\rho}) = \int_{\Gamma_0} \nabla G_0(\boldsymbol{\rho}, \boldsymbol{\rho}') \times \mathbf{J}(\boldsymbol{\rho}') d\Gamma' \quad (4.10)$$

$$\mathbf{E}(\mathbf{J})(\boldsymbol{\rho}) = \int_{\Gamma_0} \mathbf{J}(\boldsymbol{\rho}') G_0(\boldsymbol{\rho}, \boldsymbol{\rho}') d\Gamma' \quad (4.11)$$

In step 7 of the flow chart, the currents,  $\mathbf{J}^{\text{apt}(2)}$  and  $\mathbf{M}^{\text{apt}(2)}$ , radiate and induce currents on the external geometry.

$$\begin{aligned} \mathbf{J}_{(K+1)}^{\text{ext}}(\boldsymbol{\rho}') &= \mathbf{J}_{(1)}^{\text{ext}}(\boldsymbol{\rho}') + \mathbf{J}_{(K+\frac{1}{2})}^{\text{ext}} \\ &+ 2 \int_{\Gamma_2} \hat{\mathbf{n}}_{\text{ext}} \times \mathbf{H}(\delta^{\text{ext}}(\mathbf{J}_{(K+1)}^{\text{apt}(2)}, \mathbf{M}_{(K+1)}^{\text{apt}(2)}))(\boldsymbol{\rho}) d\Gamma'_2 \end{aligned} \quad (4.12)$$

The incident currents,  $\mathbf{J}_{(1)}^{\text{apt}(1)}$  and  $\mathbf{M}_{(1)}^{\text{apt}(1)}$ , are summed together with the currents set up on the outside aperture from  $\mathbf{J}_{(K)}^{\text{ext}}$ .

$$\mathbf{J}_{(K+1)}^{\text{apt}(1)}(\boldsymbol{\rho}') = \mathbf{J}_{(1)}^{\text{apt}(1)}(\boldsymbol{\rho}) + \int_{\Gamma_{\text{ext}}} \hat{\mathbf{n}}_2 \times \mathbf{H}(\delta^{\text{ext}} \mathbf{J}_{(K)}^{\text{ext}})(\boldsymbol{\rho}) d\Gamma'_{\text{ext}} \quad (4.13)$$

$$\mathbf{M}_{(K+1)}^{\text{apt}(1)}(\boldsymbol{\rho}') = \mathbf{M}_{(1)}^{\text{apt}(1)}(\boldsymbol{\rho}) + \int_{\Gamma_{\text{ext}}} \mathbf{E}(\delta^{\text{ext}} \mathbf{J}_{(K)}^{\text{ext}})(\boldsymbol{\rho}) \times \hat{\mathbf{n}}_2 d\Gamma'_{\text{ext}} \quad (4.14)$$

The currents,  $\mathbf{J}_{(K+1)}^{\text{apt}(1)}$  and  $\mathbf{M}_{(K+1)}^{\text{apt}(1)}$ , induce surface currents in the cavity which are summed together with  $\mathbf{J}_{(K+\frac{1}{2})}^{\text{cav}}$ , from step 5 of the flow chart.

$$\begin{aligned} \mathbf{J}_{(K+1)}^{\text{cav}}(\boldsymbol{\rho}') &= \mathbf{J}_{(1)}^{\text{cav}}(\boldsymbol{\rho}') + \mathbf{J}_{(K+\frac{1}{2})}^{\text{cav}}(\boldsymbol{\rho}') \\ &+ 2 \int_{\Gamma_1} \hat{\mathbf{n}}_{\text{cav}} \times \mathbf{H}(\delta^{\text{cav}}(\mathbf{J}_{(K+1)}^{\text{apt}(1)}, \mathbf{M}_{(K+1)}^{\text{apt}(1)}))(\boldsymbol{\rho}) d\Gamma'_1 \end{aligned} \quad (4.15)$$

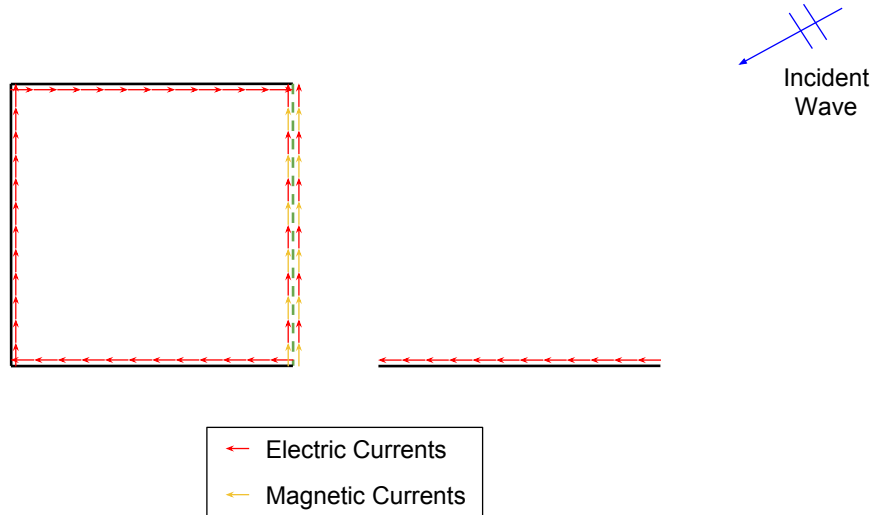


Figure 4.7: DDPO Second reflection currents.

From (4.6) to (4.15) is the recursion step of DDPO starting with  $K = 1$ . This step will be run until the number of reflections modelled is sufficient to account for all the reflections in the geometry.



### 4.3 Computational Cost

The MRPO shadowing determines the inter-segment visibility for each segment in the structure. The MRPO shadowing algorithm is able to determine the full MRPO shadowing matrix in  $O(N^2)$  operations, with  $N$  being the number of segments in the geometry, using an angular buffer scheme similar in concept to the one presented in [25].

For the structure shown in Figure 4.7, the cavity has  $N$  segments and the external geometry has  $M$  segments. The standard MRPO shadowing matrix for this structure will take  $O((N + M)^2)$  time to compute. Whereas when DDPO is used and the structure is divided into two regions, the shadowing matrix takes  $O(N^2 + M^2)$  time to compute. This will reduce the computation time by  $O(2NM)$ .

### 4.4 Validation

This section will validate the different components of the DDPO. The first test will validate that fields generated by the equivalent aperture sources tend towards the true fields. The second test will validate that the interaction between two geometries through the aperture works correctly. The aperture is represented by the green dotted line.

#### 4.4.1 Aperture Source Accuracy

The first test will evaluate how the PO current induced by aperture sources, converge as the electrical size of the aperture is increased. Figure 4.8 shows the geometry used for the test. The size of the aperture and geometry is increased from  $5\lambda$  to  $500\lambda$ . For the benchmark incident currents,  $\mathbf{E}^{\text{inc}}$  and  $\mathbf{H}^{\text{inc}}$  will only illuminate half of the geometry (red solid line). The other half will have zero incident current. The  $\mathbf{E}^{\text{inc}}$  and  $\mathbf{H}^{\text{inc}}$  induce the electric and magnetic currents on the aperture (dotted green line). The aperture will replace the incident plane wave and illuminate the geometry with the equivalent sources. The equivalent sources radiate a  $45^\circ$  incident beam which is expected to predominantly illuminate only half of the structure as the incident field has an incident angle of  $45^\circ$ .

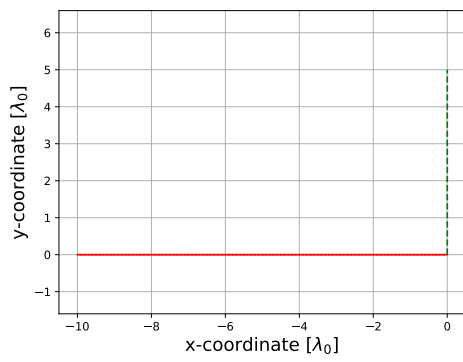
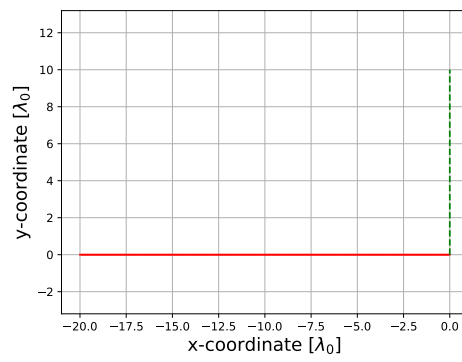
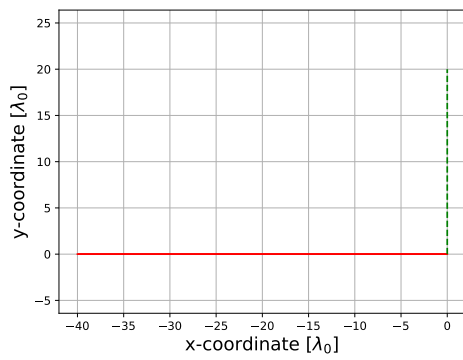
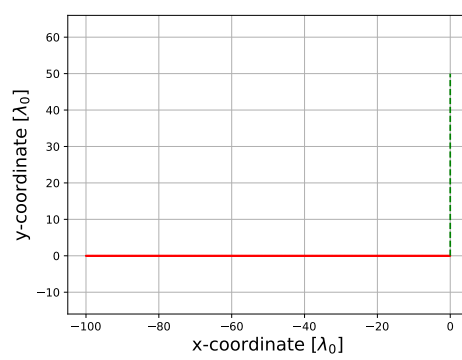
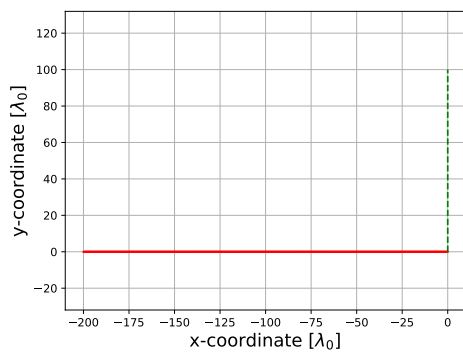
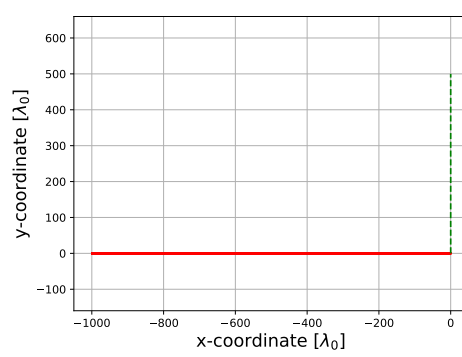
(a)  $5\lambda$ .(b)  $10\lambda$ .(c)  $20\lambda$ .(d)  $50\lambda$ .(e)  $100\lambda$ .(f)  $500\lambda$ .

Figure 4.8: Horizontal line with aperture for equivalent source tests.

The results for the current convergence test are shown in Figure 4.9.

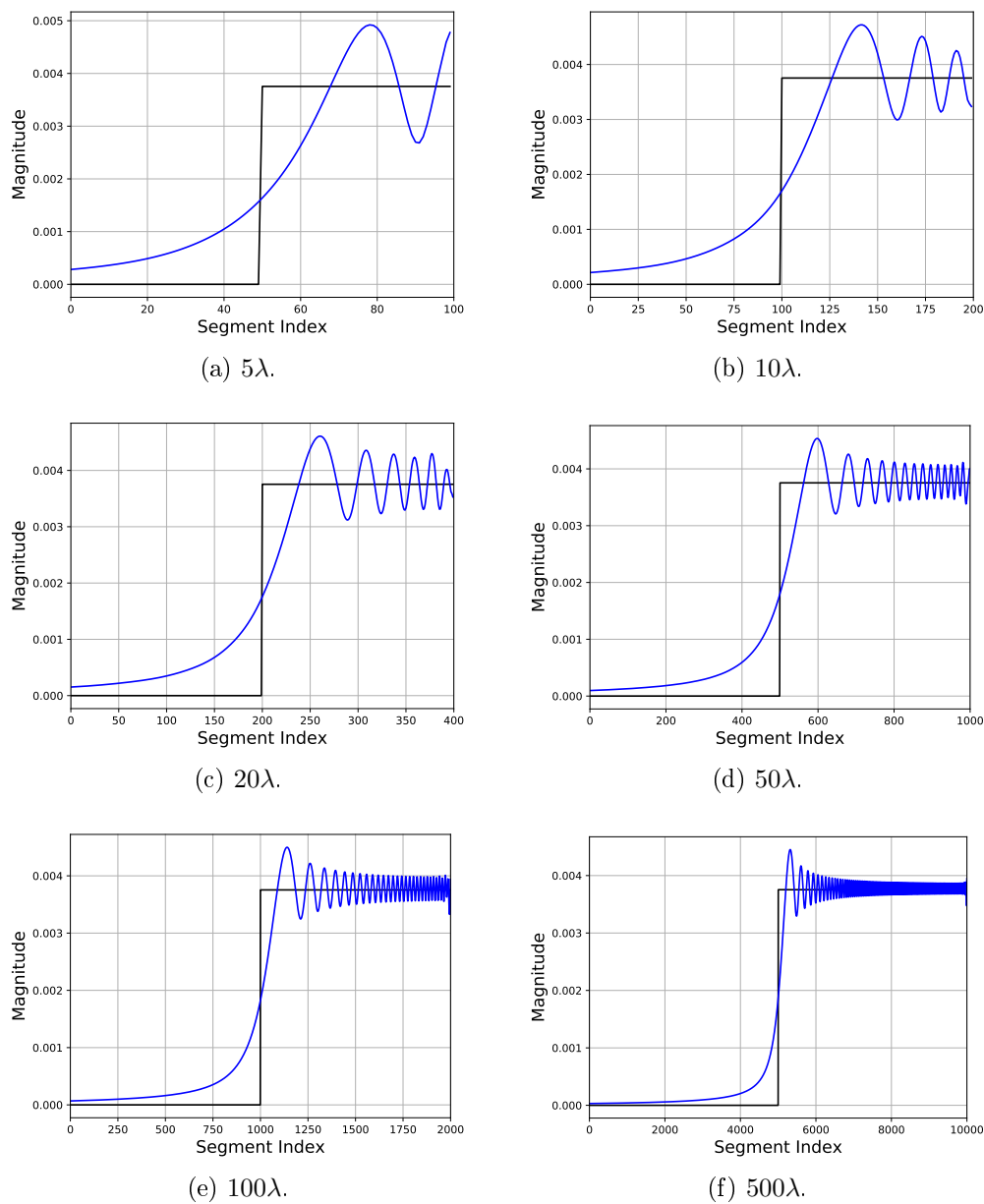


Figure 4.9: Equivalent source tests. The black line represents the current induced, on the line segment surface with half the geometry in shadow, due to the incident source. The blue line represents the current induced from the aperture.

From the results above it can be seen that the current solution does converge as the size of the aperture increases. The PO shadowing boundary is approximated very well as the size of the aperture increases. The current solution and PO shadowing boundary are not well approximated for the smaller geometries,  $5\lambda$  and  $10\lambda$ . As the aperture will always be finite in length, the

results will never be perfect as an infinite surface is needed to reproduce the fields exactly [14].

#### 4.4.2 Aperture Source Interaction

In this section, the full DDPO is employed. The effect of increasing the aperture size on accuracy, is studied. A simple corner reflector, illuminated by a  $0^\circ$  plane wave, is used. The reflector has been split into two geometries, an upper and lower reflector.

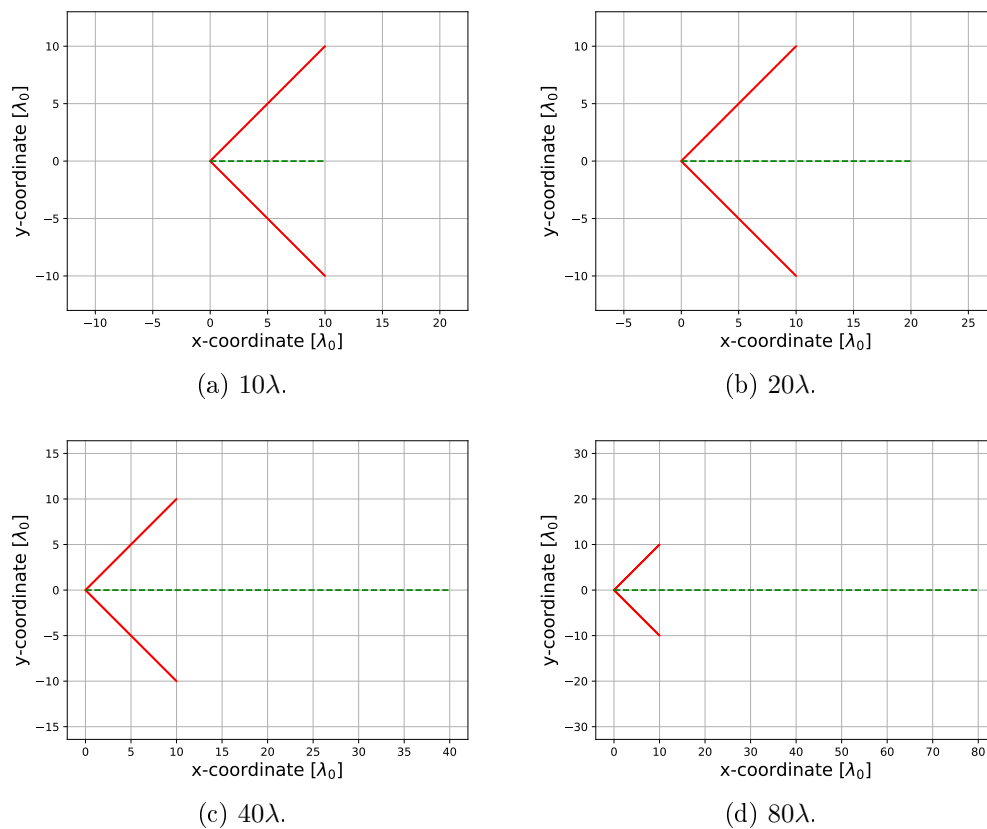
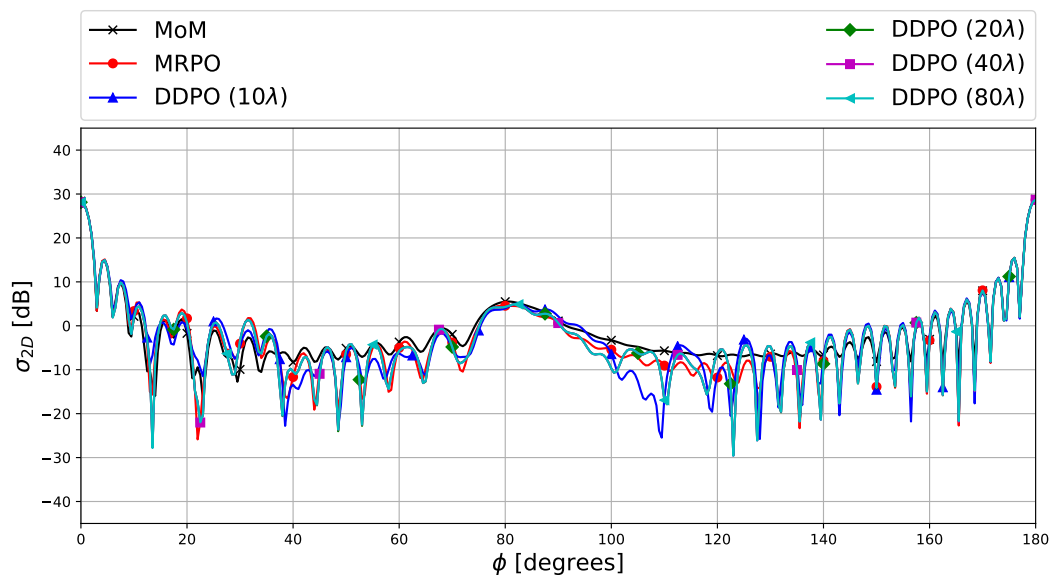
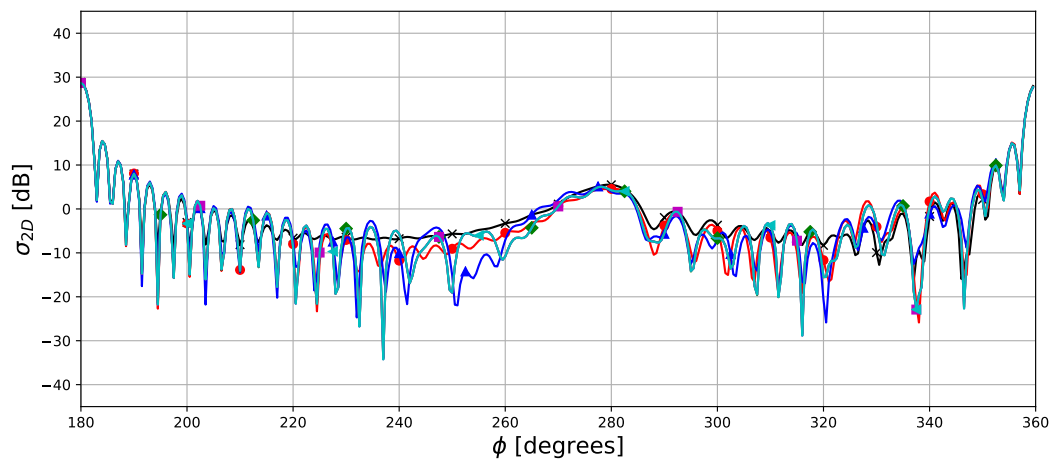


Figure 4.10:  $10\lambda$  Reflector with varying aperture sizes.



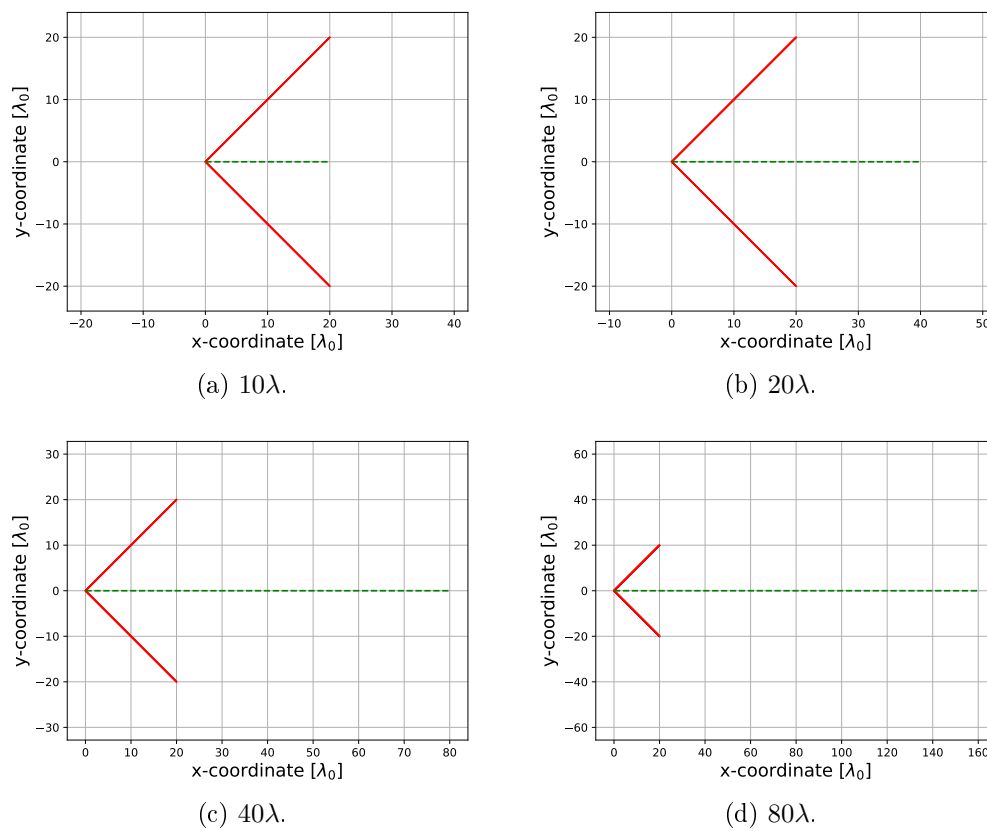
(a) Bi-static SW.

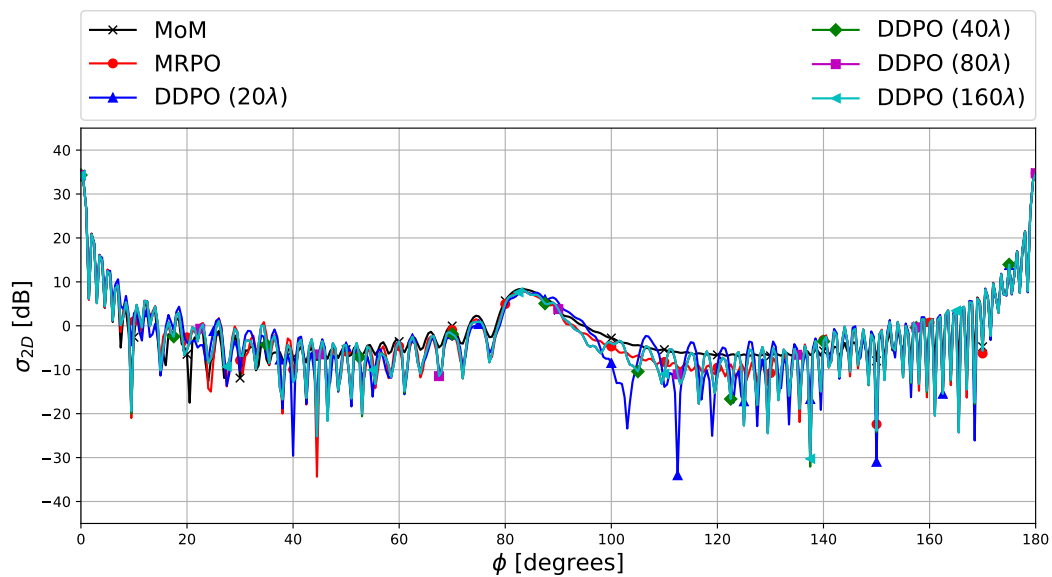


(b) Bi-static SW.

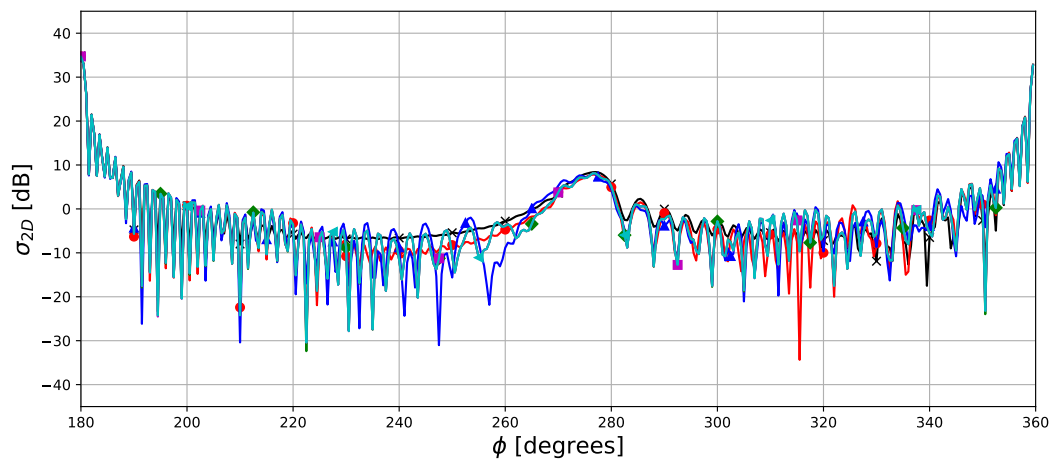
Figure 4.11:  $10\lambda$  Reflector aperture test.

Figure 4.10 shows the test structures used for the results in Figure 4.11. The results in Figure 4.11 illustrate the bi-static SW for a larger ( $10\lambda$ ) reflector. It can be seen in Figure 4.11, that the DDPO results approximate the MRPO solution well. Taking the aperture to be the extent of the geometries ( $10\lambda$ ), as would be done in case of a practical situation of a cavity aperture, the results still correspond well. The DDPO results are never perfect as the aperture is finite and only an infinitely large flat sheet can reproduce a field exactly (as per the equivalence theorem [14]).

Figure 4.12:  $20\lambda$  Reflector with varying aperture sizes.



(a) Bi-static SW.



(b) Bi-static SW.

Figure 4.13:  $20\lambda$  Reflector aperture test.

Figure 4.12 shows the test structures used for the results in Figure 4.13. The results in Figure 4.13 illustrate the bi-static RCS for a larger ( $20\lambda$ ) reflector. The DDPO results approximate the MRPO solution well.

## 4.5 Evaluation

Firstly, a simple square cavity will be used to compare the single reflection DDPO and SRPO, after which the multiple reflection DDPO will be compared to the MRPO. Once it can be seen that DDPO works for the simple square

cavity, external geometry will be added to add external reflections. The test structures will be illuminated by a  $45^\circ$  plane wave. The aperture is represented by the green dotted line.

### 4.5.1 Square Cavity

The simple square cavity is illustrated in Figure 4.14. The green dotted line indicates the aperture. The single and multiple reflection results are shown in Figure 4.15.

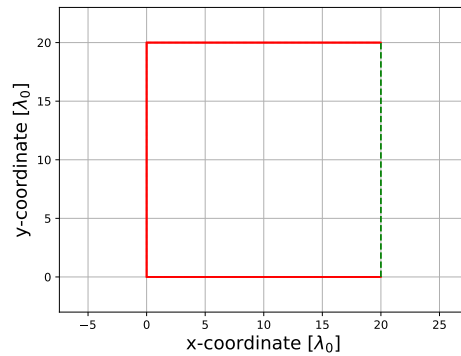


Figure 4.14: Open square cavity with aperture.



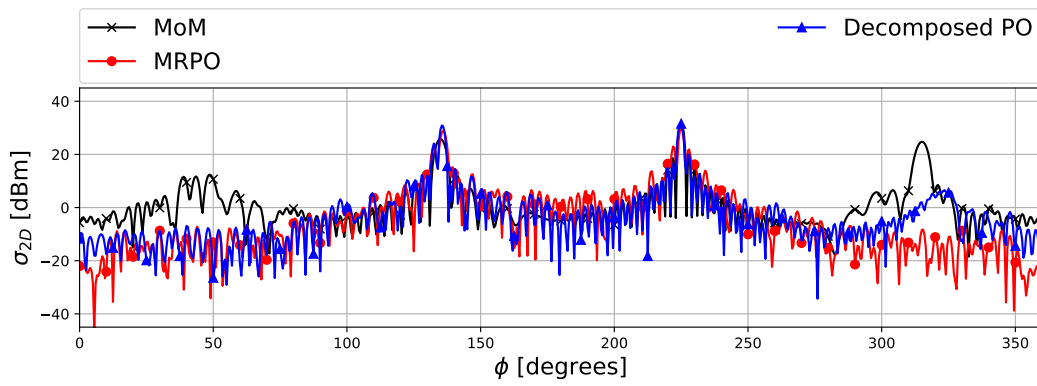
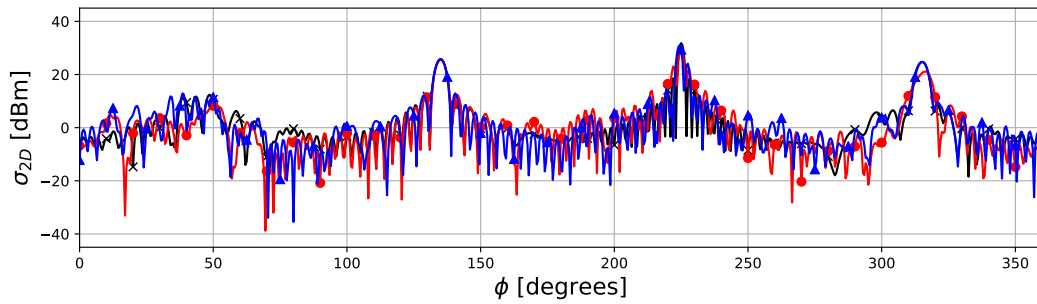
(a) Single reflection ( $K=1$ ) bi-static SW.(b) Multiple reflections ( $K=5$ ) bi-static SW.

Figure 4.15: Open square cavity with aperture bi-static SW.

The results in Figure 4.15a correspond fairly well with the SRPO, especially in the main lobes. Of course, since this geometry supports multiple physical reflections, the results do not approximate the MoM solution well. The results in Figure 4.15b show a good correspondence between MRPO and DDPO results.

## 4.5.2 Square Cavity with External Geometry

The simple square cavity with the external geometry is shown in Figure 4.16. The test structure sizes vary from  $5\lambda$  to  $50\lambda$  and are shown in Figure 4.16.

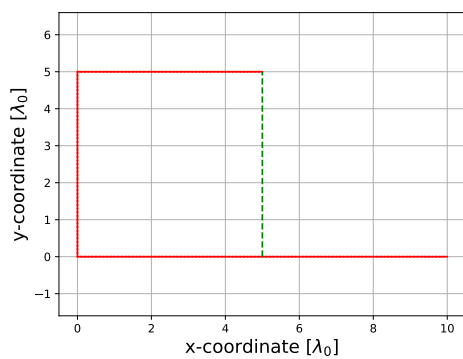
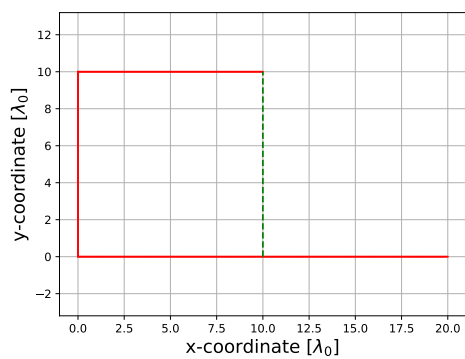
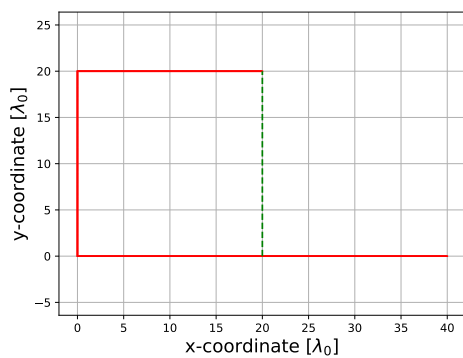
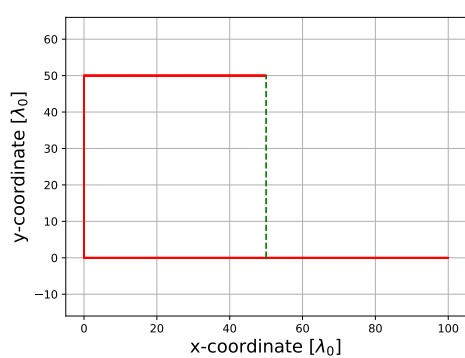
(a)  $5\lambda$  Aperture.(b)  $10\lambda$  Aperture.(c)  $20\lambda$  Aperture.(d)  $50\lambda$  Aperture.

Figure 4.16: Square cavity with external geometry.

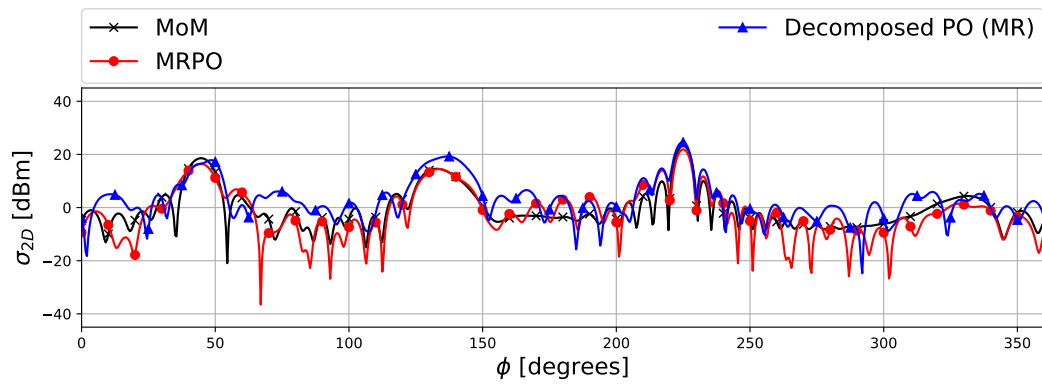
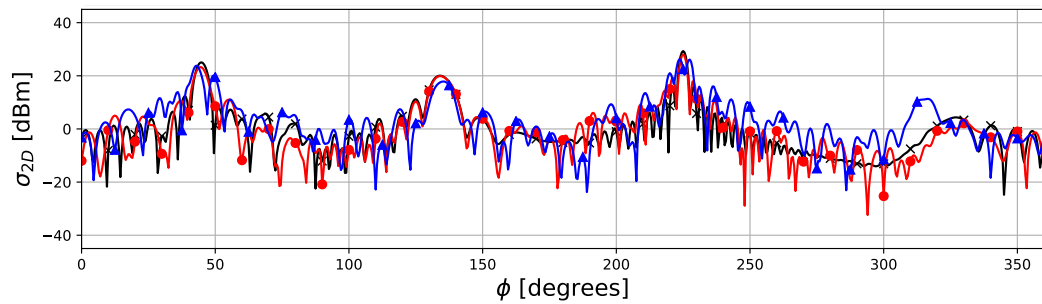
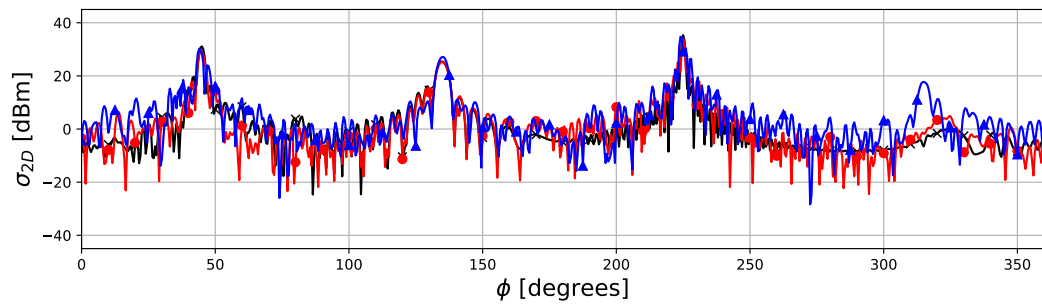
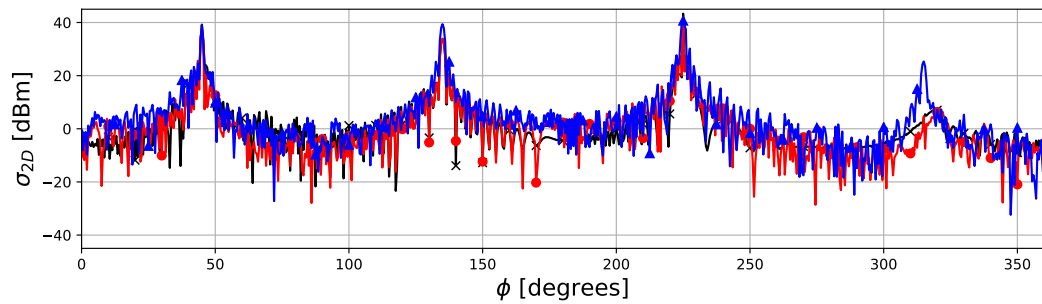
(a)  $5\lambda$  Aperture.(b)  $10\lambda$  Aperture.(c)  $20\lambda$  Aperture.(d)  $50\lambda$  Aperture.

Figure 4.17: Square cavity with external geometry bi-static SW.

From the results in Figure 4.17, it can be seen that the DDPO method is able to model reflections successfully between the two geometries via the aperture sources. The main lobes are in the same locations as the MRPO results. Since only an infinitely-sized aperture will guarantee exact correspondence, differences are expected.

## 4.6 Conclusion

The DDPO method will be very useful for large structures which contain complicated cavities. By allowing the cavity and external geometry to only interact via the aperture, the amount of computation time can be reduced.

The results in the validation section show that the aperture can act as a reasonable equivalent source. The interaction between the geometries via the aperture provides good results.

The practical test of having a cavity and some external geometry is simple but allows the concept of including other reflections into the cavity to be tested. The results correspond mostly well with the MRPO, though notable differences are apparent. The DDPO method was able to model the reflections between the two geometries.

# Chapter 5

## Conclusion

This thesis investigated mesh-based PO methods of electromagnetic scattering analysis, in a 2D, TM context. The formulation of the MoM in Chapter 2 served as the basis from which the MFIE and EFIE were derived. These were required later in the investigation. The MoM was formulated first since it provided necessary reference results throughout. The PO chapter provided a detailed break down of MRPO and IPO variants and the relative performance of the PO-based methods was assessed. The effect of modelling the internal and external currents versus only modelling the external current was investigated upon the accuracy of the PO. The Relaxed Jacobi method was altered to be more general instead of having a set value as in [12]. The  $\alpha$  parameter was varied to investigate different solutions. In the final chapter, DDPO was introduced. A surface of equivalent sources was used to interact between two different geometries. This way the reflections from the geometries are able to communicate via the equivalent sources. The MFIE from Chapter 2 was used extensively here. Various tests were performed to show that the equivalent sources and aperture interact correctly.

The comparative study of the PO-based methods in Chapter 3 showed that MRPO typically corresponded quite well with the MoM solutions and was consistent. The Jacobi and Relaxed Jacobi methods gave good results for open structures. For the closed structure, Jacobi did not converge and performed poorly. Relaxed Jacobi was able to converge and the results approximated the MoM solution fairly well. Relaxed Jacobi was the most consistent IPO method. JMRES was not always able to approximate the forward scattering well and performed poorly in most of the test cases. The IPO methods performed better when the internal currents for a closed structure were not modelled. However, the Relaxed Jacobi was unchanged when the internal currents were not modelled. The IPO methods were not as reliable as MRPO.

In the DDPO chapter, it was demonstrated that reflections can be successfully transferred via the aperture. The structure can be broken up into two geometries. The benefit of this being that the shadowing matrix for the entire geometry does not need to be computed, thus lowering the computational cost.

The DDPO results corresponded well with the MRPO results. The DDPO solution does not match the MRPO solution exactly, which is expected due to the fact that finite-sized apertures are used for the equivalent sources.

Future recommendations would be to implement the PO investigation and DDPO in 3D. Real-world problems are seldom only in two dimensions. However, this did allow for ideas to be explored more easily, since it is simpler. The MLFMM acceleration in [18] can be incorporated into the DDPO. This will have a dramatic effect on the computational cost of the shadowing matrix. The DDPO has been limited to only one aperture per structure, which again will not necessarily be sufficient for real-world problems. To simplify the structure and decrease the computation time, multiple apertures should be considered. In the case of the airplane in Figure 4.1, an aperture could be placed on each of the engines. This would greatly simplify the problem.

# List of References

- [1] A. F. Peterson, S. L. Ray, and R. Mittra. *Computational methods for electromagnetics*. Oxford & New York: Oxford University Press and IEEE Press, 1998.
- [2] J. M. Jin. *Theory and Computation of Electromagnetic Fields*. New York: John Wiley and Sons, 2010.
- [3] W. C. Chew, E. Michielssen, J. M. Song, and J. M. Jin. *Fast and efficient algorithms in computational electromagnetics*. Artech House, Inc., 2001.
- [4] W. L. Stutzman and G. A. Thiele. *Antenna Theory and Design, 2nd Edition*. New York: John Wiley and Sons, 1998.
- [5] R. G. Kouyoumjian and P. H. Pathak. A uniform geometrical theory of diffraction for an edge in a perfectly conducting surface. *Proc. IEEE*, 62(11):1448–1461, 1974.
- [6] H. Ling, R. C. Chou, and S. W. Lee. Shooting and bouncing rays: Calculating the RCS of an arbitrarily shaped cavity. *IEEE Transactions Antennas and Propagation*, 37(2):194–205, 1989.
- [7] F. Saez de Adana, O. Gutiérrez, I. González, M. F. Cátedra, and L. Lozano. *Practical Applications of Asymptotic Techniques in Electromagnetics*. Boston: Artech House, 2011.
- [8] C. Corbel, C. Bourlier, N. Pinel, and J. Chauveau. Rough Surface RCS Measurements and Simulations Using the Physical Optics Approximation. *IEEE Transactions on Antennas and Propagation*, 61(10):5155–5165, 2013.
- [9] B. Persson and M. Norsell. On modeling RCS of aircraft for flight simulation. *IEEE Antennas and Propagation Magazine*, 56(4):34–43, 2014.
- [10] F. Obelleiro-Basteiro, J. L. Rodriguez, and R. J. Burkholder. An iterative physical optics approach for analyzing the electromagnetic scattering by large open-ended cavities. *IEEE Transactions on Antennas and Propagation*, 43(4):356–361, 1995.
- [11] R. J. Burkholder. A fast and rapidly convergent iterative physical optics algorithm for computing the RCS of open-ended cavities. *Applied Computational Electromagnetics Society Journal*, 16(1):53–60, 2001.

- [12] R. J. Burkholder, C. Tokgöz, C. J. Reddy, and W. O. Coburn. Iterative physical optics for radar scattering predictions. *Applied Computational Electromagnetics Society Journal*, 24(2):241–258, 2009.
- [13] K. E. Atkinson. *The Numerical Solution of Integral Equations of the Second Kind*. Cambridge, UK: Cambridge University Press, 1997.
- [14] C. A. Balanis. *Advanced Engineering Electromagnetics*. John Wiley & Sons, Inc., 2012.
- [15] W. C. Gibson. *The Method of Moments in Electromagnetics*. Chapman & Hall/CRC, 2008.
- [16] Ieee standard for radar definitions. *IEEE Std 686-2017 (Revision of IEEE Std 686-2008)*, pages 1–54, Sept 2017.
- [17] Altair Engineering, Inc. *User Manual for FEKO 2017.2*. <http://feko.info/>, 2017.
- [18] D. P. Xiang and M. M. Botha. MLFMM-based, fast multiple-reflection physical optics for large-scale electromagnetic scattering analysis. *Submitted for publication*, 2016.
- [19] G. H. Golub and C. F. Van Loan. *Matrix Computations, 4th Edition*. The Johns Hopkins University Press, 2013.
- [20] Y. Saad. *Iterative Methods for Sparse Linear Systems, Second Edition*. Society for Industrial and Applied Mathematics, 2003.
- [21] C. T. Kelly. *Iterative Methods for Linear and Non-Linear Equations*. Raleigh, North Carolina, 1998.
- [22] M. P. Richardson and M. M. Botha. Comparative results for multiple-reflection physical optics (MRPO) and iterative physical optics (IPO). *IEEE AP-S Symposium on Antennas and Propagation*, pages 2364–2365, 2017.
- [23] 3D CAD Browser. Boeing 747-400 3D Model, 2017.
- [24] GE Aviation. The GENx Commercial Aircraft Engine, 2017.
- [25] D. P. Xiang and M. M. Botha. Efficient shadowing determination at grazing incidence, for mesh-based physical optics scattering analysis. *Electronics Letters*, 52(22):1893–1894, 2016.